MODELING GAS PRODUCTION FROM

METHANE HYDRATE SEDIMENTS

A Dissertation

by

MEHDI TEYMOURI

Submitted to the Office of Graduate and Professional Studies of
Texas A&M University
In partial fulfillment of requirements for the degree of

DOCTOR OF PHILOSOPHY

Chair of Committee,	Marcelo Sánchez
Committee Members,	Yucel Akkutlu
	Charles Aubeny
	Robert Lytton
Head of Department,	Robin Autenrieth

December 2018

Major Subject: Civil Engineering

ABSTRACT

Constitutive modeling of gas production from methane hydrates, as the largest source of hydrocarbons on Earth, is one of the challenging topics in the field of Energy Geotechnics. Methane hydrates are solid compounds made of water molecules clustered around methane gas molecules. The ice shaped methane hydrates form under specific conditions of high pressure and low temperature that are common in sub-permafrost layers and in deep marine sediments. Methane gas is produced from hydrate bearing sediments (HBS) as a valuable energy resource based on releasing the molecules of gas from lattice components of hydrate with the aid of depressurization, heat and/or chemical stimulation. Coupled thermal, hydraulic, chemical and mechanical (THCM) analyses are necessary for realistic simulation of this complex phenomenon since hydrate dissociation comes with interrelated THCM processes. In this study, a numerical code based on a general mathematical formulation is used to analyze coupled THCM problems involving gas hydrate bearing sediments. It takes into consideration thermal and hydraulic processes, effective stress and the change in sediment properties in the presence of hydrates. This fully coupled formulation incorporates the different phases existing in HBS (including hydrate and ice) and has been implemented in CODE_BRIGHT, an existing coupled multiphysics program for geological media.

An analytical solution is also proposed for the steady state condition involving fluid flow in a cylindrical geometry and accounting for the presence of two zones of different permeability coefficients. This solution can be very useful in problems encompassing HBS since it can determine the depressurization zone of influence, which paves the path to define realistic boundary

conditions in the numerical simulation. Furthermore, the effect of crucial parameters on hydrate dissociation, induced by depressurization, are investigated by both constitutive modeling and analytical solution.

Beside the comparison between the outputs of the numerical analysis with the corresponding analytical solution, which are satisfactory compatible, the presented numerical formulation has been verified by some of the previous experimental data. The numerical simulations successfully capture the coupled processing associated with the hydrate dissociation/formation reported by the experiments and address the characteristic behavior of HBS.

ACKNOWLEDGMENTS

First, I would like to express my sincere gratitude to Professor Marcelo Sánchez for the patient guidance, encouragement, and advice he has provided throughout my time as his student. It has been my ultimate pleasure to have a supervisor who cared so much about my research, and who responded to my questions and queries so patiently and promptly. Without his constructive feedback and continuous encouragement, I would not have been able to complete the dissertation.

I would also like to extend my deepest appreciation to my dissertation committee, Professor Charles Aubeny, Professor Robert Lytton, and Professor Yucel Akkutlu, for their direction, dedication, and invaluable advice along this research.

Finally, my special thanks go to my family for all the support and love they have given me; for their encouragement and placing their confidence in me; for letting me find my own way.

CONTRIBUTORS AND FUNDING SOURCES

Contributors

Part 1, faculty committee recognition: This work was supervised by a dissertation committee consisting of Professor Marcelo Sánchez (advisor), Professor Charles Aubeny, and Professor Robert Lytton of the Zachry Department of Civil Engineering and Professor Yucel Akkutlu of the Harold Vance Department of Petroleum Engineering.

Part 2, student/advisor contributions: All work for the dissertation was completed by the student, under the advisement of Professor Marcelo Sánchez of the Zachry Department of Civil Engineering.

Funding Sources

TABLE OF CONTENTS

LIST OF FIGURES

LIST OF TABLES

Page

1. INTRODUCTION

Ice shaped crystalline methane hydrate (Figure.1.1) is the largest source of hydrocarbons on Earth. (Sloan, 1998; Soga et al., 2006; Rutqvist & Moridis, 2007; Boswell, 2009). This enormous source of methane, which is made of water molecules clustered around methane molecules, forms under specific conditions of high pressure and low temperature that are common in sub-permafrost layers and also in deep marine sediments. One cubic meters of methane hydrate contains at least 168 m^3 of methane gas at the standard pressure and temperature conditions. According to estimations, the amount of this huge intact energy resource is at least twice of the whole amount of conventional oil and gas reservoirs (Kvenvolden, 1998; Lee & Holder, 2001; Milkov, 2004; Klauda & Sandler, 2005; Sloan & Koh, 2007). Methane gas is produced from hydrate bearing sediments, HBS, as a valuable clean energy resource based on releasing the molecules of gas from lattice components of hydrate, known as hydrate dissociation, with the aid of depressurization, CH_4-CO_2 replacement, heat and/or chemical stimulation (Figure.1.2).

Figure 1.1 Methane hydrate; an enormous environmentally friendly energy resource.
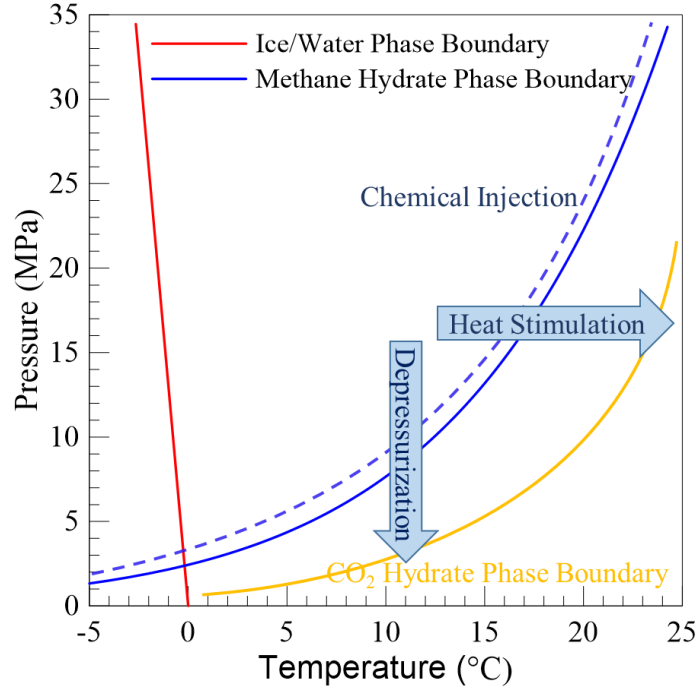
Figure 1.2 Main methods of gas production from HBS

The experimental study of HBS has been hindered by the very low solubility of methane in water (preparing artificial samples in lab), and inherent sampling difficulties associated with depressurization and thermal changes during core extraction. This situation has prompted more decisive developments in numerical modeling in order to advance the current understanding of HBS, and to investigate/optimize production strategies and implications.

Numerical modeling is equally challenged by the complex behavior of HBS since hydrate dissociation comes along with interrelated thermal, hydraulic, chemical, and mechanical, THCM, processes. For example, releasing gas from hydrate component is accompanied by a significant volume expansion, which results in either considerable fluid flux in free draining conditions, or high fluid pressure if the rate of dissociation is faster than the rate of fluid pressure dissipation. Consequently, changes in fluid pressure will alter the effective stress, hence the stiffness, strength and dilatancy of the sediment. Moreover, the permeability coefficient, as a crucial parameter in the fluid flow problem, will change because of a variation in temperature, in hydrate saturation, and volume expansion/contraction. Also, mechanical strength of sediments depends on hydrate

2

saturation while the effective stresses are affected by depressurization. Therefore, coupled THCM analyses are inevitable for providing realistic simulation of this complex phenomenon.

Furthermore, methane gas production from HBS in permafrost possess additional challenges and opportunities. Complex stress paths in the pressure and temperature space, the P-T space, with two phase boundaries (i.e. gas-hydrate and ice-liquid phase lines) are anticipated during gas production, including secondary hydrate and ice formation. Therefore, ice phase must be explicitly incorporated in the analysis as it affects mechanical stability, fluid migration, and thermal properties.

There are also side effects associated with hydrate dissociation, since it can cause borehole instability, blowouts, foundation failures, and trigger large-scale submarine slope failures (Kayen & Lee, 1991; Jamaluddin et al., 1991; Briaud & Chaouch, 1997; Chatti et al., 2005). Moreover, sand production has been reported during previous field trial tests (Yamamoto et al., 2014; Uchida et al. 2016). The escape of methane into the atmosphere would exacerbate greenhouse effects and contribute to global warming (Dickens et al., 1997).

1.1. Background

Several formulations have been developed to explore various aspects of hydrate formation and dissociation within well-defined boundary conditions (Rempel & Buffett 1997, 1998; Xu & Ruppel 1999; Davie & Buffett, 2001; Ahmadi et al 2004; Sultan et al., 2004; Xu & Germanovich 2006; Nazridoust & Ahmadi 2007; Kwon et al. 2008). In these models, the sediment response is disregarded or handled with simple models (e.g., non-deformable rigid porous medium is assumed in Nazridoust & Ahmadi (2007), an elastic porous medium in Kwon et al. (2008); and a non-linear 1D compression law in Garg et al. 2008). HM coupled isothermal models with more appropriate (mechanical) sediment representation has been developed by Klar et al. (2010). Other hydrate simulators mainly focused on fluid flow and phase changes, rather than on the mechanical behavior of HBS (e.g. White & McGrail, 2008). Chemo-thermo-mechanical analyses related to ground deformation and gas production are presented in Kimoto et al. (2007, 2010). Rutqvist & Moridis (2007), Rutqvist (2011), and Kim et al. (2012) presented a more general THMC approach by linking (sequentially) a geomechanical code (FALC^{3D}) with a multiphase fluid and heat transport simulator (TOUGH+HYDRATE). More recently, Gupta et al. (2017) proposed a TCHM code for

HBS that is based on a simplified coupling concept for linking different simulators. Ajayi et al. (2018) discussed key aspects to consider when modeling gas production from HBS.

Furthermore, some analytical solutions have been proposed to analyze depressurization (Goel et al. 2001; Ji et al. 2001; Hong et al. 2003; Tsypkin 2000), thermal stimulation (Ullerich et al. 1987; Esmaeilzadeh et al. 2011; Klar et al. 2013), and local conditions (Kwon et al. 2008). However these analyses also remain complex, require iterative solution and hide explicit relations between governing parameters (Sanchez & Santamarina, 2015).

1.2. Gap in the Knowledge

Currently, some simulator codes are provided as results of previous studies (Moridis, 2014; Hong & Pooladi-Darvish 2005; Moridis et al. 2008; Walsh et al. 2009; Konno et al. 2010) such as TOUGH+HYDRATE (Lawrence National Lab), MH21-HYDRES (Japan Oil Engineering Company), CMG_STARS (Computer Modeling Group, Canada), STOMP-HYD (Pacific Northwest National Laboratory) but they are complex and suffer from time and space discretization errors due to a large number of equations, constitutive relations, and parameters involved (Pooladi-Darvish 2004). Also, sequential explicit computational schemes are implemented in most of them. Truly coupled THCM numerical approaches rather than sequential explicit computational schemes (i.e., they resolve the hydrate state separate from the sediment state at every time step) is recommendable for the robust analysis of hydrate bearing sediments. Sequential schemes often restrict computations to one-way coupled analysis where one can investigate. For example, it considers the effect that change in pressure and/or temperature has on the sediments mechanical response while it does not account for the effect of granular strains on the multiphase flow behavior. Furthermore, sequential schemes are generally less efficient because they require the use mapping algorithms to transfer the information between the codes used to solve the different physics. Therefore, the fully coupled THCM numerical code formulation that incorporates the different phases existing in HBS (including hydrate and ice) is necessary to simulate the methane hydrate formation/dissociation form the laboratory to the field scale reservoir. The robust monolithic approach in implicit truly-coupled methods leads to computational efficiency and improved rate of convergence in the solution of the coupled nonlinear problem.

4

Additionally, implementing realistic boundary conditions in the numerical modeling is inevitable for the sake of precise simulation. Up-to-date, no criterion has been presented to determine the influence length of depressurization within the reservoir induced by the vertical well. For instance, gas production from HBS at the Mount Elbert located in the North Slope of Alaska is simulated with TOUGH+HYDRATE by Moridis et al. (2011). A cylindrical 2D axisymmetric geometry with the outer radius of 400m is used for modeling the reservoir with vertical well while there is no strong discussion behind the assumed horizontal limitation of reservoir.

Issues associated with sand production was observed in previous field trial methane hydrate gas producing operations. For instance, sanding was occurred during ConocoPhillips gas production test from gas hydrate sediments in Ignik Sikumi field on North Slope of Alaska. Also, during the 1ˢᵗ offshore gas hydrate field trial production at Nankai Trough (Japan) in 2013, the operation was terminated on day 6 due to severe sanding. Sand production is a relatively well-known problem that has been extensively studied in the context of hydrocarbon production from conventional reservoirs. However, sanding associated with methane hydrate production possess new and significant challenges that require further research. A clear difference is that hydrate dissociation induces profound changes in the sediment structure, facilitating even more disaggregation of particles and their subsequent transport.

1.3. Objectives

The main aim of this research is to investigate the coupled THCM processes during methane hydrate dissociation by studying its natural behavior and simulating it through both the numerical analysis and analytical solution.

Truly coupled processing in the enhanced numerical code paves the path:

- to advance the current knowledge of HBS;
- to simulate hydrate dissociation/formation more efficiently and precisely;
- to investigate the crucial parameters, which affects the methane hydrate gas production;
- to optimize the future field production studies in marine and permafrost sediments;
- to minimize the hazardous side effects;

- to address the most pertinent questions that have emerged from both past lab tests and previous field scale experiences.

The proposed simple yet robust analytical solution at steady state conditions makes it possible:

- to predict the maximum recoverable gas form HBS based on initial and boundary conditions;
- to consider a realistic boundary conditions in the numerical analysis;
- to validate the results achieved by the numerical analysis;
- to perform sensitivity studies on the essential factors affecting the methane hydrate production and examine different strategies.

1.4. Activities

The scope of the conducted study has been related to the development of a formal and robust numerical framework able to capture P-T paths and ensuing phase transmissions during methane hydrate gas production in both marine and permafrost settings based on the analysis of available data from laboratory tests and field experiments. The analytical solution has also been proposed to predict the influence zone of depressurization induced gas hydrate production in a 2D axisymmetric cylindrical geometry with various confining situations at the steady state condition. The main following activities have been conducted:

- in-depth reviewing of the properties associated with gas hydrates sediments;
- updating the coupled THCM formulations and the numerical code for hydrate bearing sediments to incorporate augmented constitutive models;
- developing the close-form analytical solutions that highlight the interplay between governing parameters in the context of gas production, and to corroborate the numerical code with these close-form end-member situations (i.e., close form solutions will inherently involve simplifying assumptions such as considering the problem at the steady state condition);
- studying on the sanding phenomenon, which comes along with methane hydrate gas production from unconsolidated sand stone reservoirs and providing the augmented formulations to upgrade the numerical code.

- gathering data about past laboratory tests and previous field scale productions to validate the numerical code and to address the most pertinent questions that have emerged from earlier experiences;

- implementing the enhanced code (in combination with the proposed analytical solutions) to optimize methane hydrate gas production in marine and permafrost sediments by investigating the effect of crucial parameters on hydrate dissociation, like the permeability coefficient, the imposed pressure and temperature at wellbore area, heterogeneity in sediments, reservoir initial and boundary conditions.

1.5. Methodology

A numerical code based on a general mathematical formulation is upgraded to analyze coupled THCM problems involving gas hydrate bearing sediments. This finite element, FE, program takes into consideration thermal and hydraulic processes, effective stress and the change in sediment properties in the presence of hydrates. It is a fully coupled formulation that incorporates the different phases existing in HBS (including hydrate and ice) and has been implemented in CODE_BRIGHT, standing for COupled DEformation, BRIne, Gas, and Heat Transport problems, which is an existing coupled multiphysics program for geological media (Olivella et al. 1996).

Also, an analytical solution is studied for the steady state condition involving fluid flow in an axisymmetric cylindrical geometry with various confining situations and accounting for the presence of two zones of different permeability coefficients for hydrate bearing sediments and free hydrate sediments within the reservoir. This solution can be very useful in problems encompassing HBS as it provides the physical limit to the zone around a well that can experience dissociation triggered by depressurization. This solution makes it possible to predict the maximum amount of gas that can be produced from a given reservoir under this assumptions. The outputs of the numerical analysis are verified with the analytical solution.

1.6.Scope of Chapters

Below, a description of the main components of the conducted research is summarized.

In order to deal with coupled THCM processing involved in gas hydrae production, the inherent behaviors of HBS should be studied. For instance, hydrate dissociation as an endothermic phenomenon comes with either a volume expansion or a generated excess pore pressure. These properties of HBS is explored in *Chapter.2*.

The theoretical framework and the main formulations implemented to enhance the numerical code are explained in *Chapter.3*. Also, a number of simple 1D models are provided to capture all the probable P-T paths, which are common in simulating hydrate/ice formation/dissociation.

A simple yet robust analytical solution, which calculates the ultimate radius of reservoir affected by depressurization from vertical well is introduced in *Chapter.4*. The suggested analytical solution can predict maximum recoverable gas from HBS by depressurization. Moreover, it paves the path to have realistic boundary conditions in the numerical modeling. The results of numerical code presented in *Chapter.3* have been validated with that of this analytical solution. The proposed solution can also describe the effect of crucial parameters on depressurization induced gas hydrate production.

The numerical code explained in *Chapter.3* can be enhanced to simulate the sand production associated in HBS. The augmented formulations is provided in *Chapter.5*.

The gathered data of two laboratory depressurization induced dissociation tests performed on natural HBS samples are presented in *Chapter.6*. Both experiments are simulated by the enhanced numerical code and results are satisfactory compatible with the lab reports. Moreover, the history of HBS formation in a permafrost setting reported by Dai et al. (2011) is illustrated and analyzed with the numerical simulator.

The dissertation is concluded and some recommendations for future studies are provided in *Chapter.7*.

2. INHERENT BEHAVIORS OF HBS: VOLUME EXPANSION

DURING HYDRATE DISSOCIATION

Gas hydrates are solid compounds consisting of water molecules clustered around low molecular weight gas molecules (Figure.2.1). According to mass balance equations, the mass of this solid compound should be equal to the summation mass of released water and gas molecules after dissociation:

$$m_h = m_l + m_g \tag{1}$$
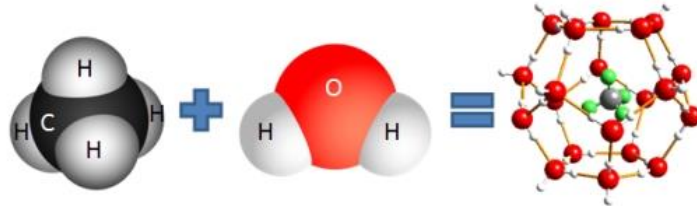
Figure 2.1 A unit of methane hydrate composed by molecules of water clustered around methane molecules

Hydrate molecular structure is indicated by the hydration number. Therefore, the water mass fraction in hydrate solid compound *'α'* could be derived as,

$$\alpha = \frac{m_l}{m_h} = \frac{X}{(0.89 + X)} \tag{2}$$

Note that for the case of methane-hydrate: *X=5.75* and *α=0.866*

It can be concluded that the following equations are valid for the mass fraction of water and gas molecules composing a molecule of hydrate.

$$m_l = \alpha \, m_h \tag{3}$$

$$m_g = (1 - \alpha) m_h \tag{4}$$

The variation of void volume due to dissociation is the summation of changes in volume of hydrate, gas, and liquid phases. The amount of volume expansion could be derived as follows:

$$\frac{dV_V}{V_V} = \frac{dV_l + dV_g + dV_h}{V_V} = \frac{\left[\alpha\left(\frac{\rho_h}{\rho_l}\right) + (1-\alpha)\left(\frac{\rho_h}{\rho_g}\right) - 1\right]dV_h}{V_V} = R_V dS_h \tag{5}$$

where dS_h represents de reduction in hydrate saturation because of dissociation.

$$R_V = \alpha\left(\frac{\rho_h}{\rho_l}\right) + (1-\alpha)\left(\frac{\rho_h}{\rho_g}\right) - 1 \tag{6}$$

where R_V is the factor of volume expansion resulting from the gas hydrate dissociation (Xu and Germanovich, 2006). The minus sign for hydrate volume indicates the consumption of hydrate due to dissociation while the gas and water are released. As shown in the equations above, the factor of volume expansion inherently depends on molecular structure of hydrate 'α' and also is a function of gas, liquid and hydrate densities. Gas and liquid densities highly depends on pressure P [MPa] and temperature T [°C], while the dependency of solid hydrate density (ρ_h=900kg/m^3) on variation of pressure and temperature is negligible.

$$\rho_l = \rho_{l_0}\left(1 + \frac{P}{\beta_l}\right)\left(1 - \beta_{T_l}\left[\frac{(T+273.15) - 277}{5.6}\right]^2\right) \tag{7}$$

where $\rho_{l_0} = 999.8$ [kg/m^3], $\beta_l = 2000$ [MPa] and $\beta_{T_l} = 0.0002 \circ K^{-1}$.

$$\rho_g = \frac{M_m.P}{R(T+273.15)}\left[1176 + 12.7\left(\frac{P}{P_{ref}}\right) - 0.45\left(\frac{P}{P_{ref}}\right)^2\right] \tag{8}$$

where M_m=16.042 g/mole; R=8.314 J/(mol°K), and P_{ref}=1[MPa]

2.1. Factor of Volume Expansion

Since the factor of volume expansion 'R_V' is a function of liquid and gas densities which are highly dependent on pressure and temperature, it considerably changes through methane-hydrate phase boundary. Figure.2.2 illustrates the variation of R_V through methane-hydrate phase

boundary. As shown, the rate of volume expansion is much higher for the case of cold reservoir (permafrost region).
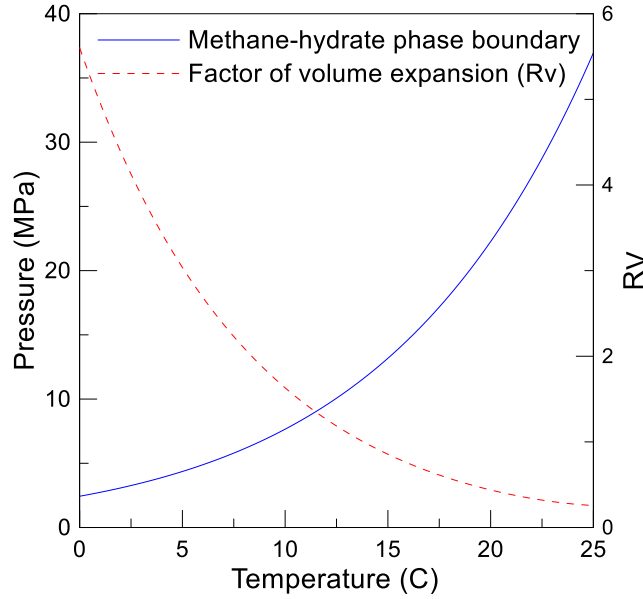
Figure 2.2 Variation in factor of volume expansion through methane-hydrate phase boundary.

2.2. Excess Pore Pressure

The volume expansion that takes place during hydrate dissociation may induce some of the following effects: i) compression of the liquid and/or gas phases (mainly associated with undrained and rigid skeleton conditions); ii) advective fluxes of gas and liquid phases (triggered by the gradient of fluid pressure under drained conditions); iii) sediment deformation (related to changes in effective stresses in deformable media).

For the case of compression of the liquid and gas phases, it can be estimated from the excess pore pressure generated during dissociation. Considering a rigid and undrained sediment, the increment of the excess pore pressure (P_{ex}) can be estimated as a function of the hydrate dissociation (dS_h), factor of volume expansion (R_v), and the equivalent volume compressibility of void phases (K_{eq}):

$$P_{ex} = \int_0^{\Delta S_h} \frac{R_V}{K_{eq}} dS_h \qquad (9)$$

11

The compressibility coefficients of gas and liquid phases, 'K_g' and 'K_l' respectively (Figure.2.3), through methane-hydrate phase boundary can be calculated from the following expressions:

$$K_g = \frac{\partial \rho_g}{\partial P} + \frac{\partial \rho_g}{\partial T}\frac{dT_{eq}}{dP} \tag{10}$$

$$K_g = \left[\frac{M_m}{R(T+273.15)}\right]$$
$$\left[\left(1176+25.4P-1.35P^2\right) - \frac{P}{(T+273.15)}\left(1176+12.7P-0.45P^2\right)\left(\frac{8860}{\left(P\times10^3\right)\left(40.234-\ln\left(P\times10^3\right)\right)^2}\right)\right] \tag{11}$$

$$K_l = \frac{\partial \rho_l}{\partial P} + \frac{\partial \rho_l}{\partial T}\frac{dT_{eq}}{dP} \tag{12}$$

$$K_l = \left(\frac{\rho_{l_0}}{\beta_l}\right)\left(1-\beta_{T_l}\right)\left[\frac{(T+273.15)-277}{5.6}\right]^2 +$$
$$\left[\rho_{l_0}\left(1+\frac{P}{\beta_l}\right)\left(-\beta_{T_l}\right)\left(\frac{1}{5.6}\right)^2\left(2T-554\right)\left(\frac{8860}{\left(P\times10^3\right)\left(40.234-\ln\left(P\times10^3\right)\right)^2}\right)\right] \tag{13}$$

The equivalent volume compressibility factor 'K_{eq}' can be calculated as:

$$K_{eq} = \frac{K_g S_g + K_l S_l}{S_g + S_l} \tag{14}$$
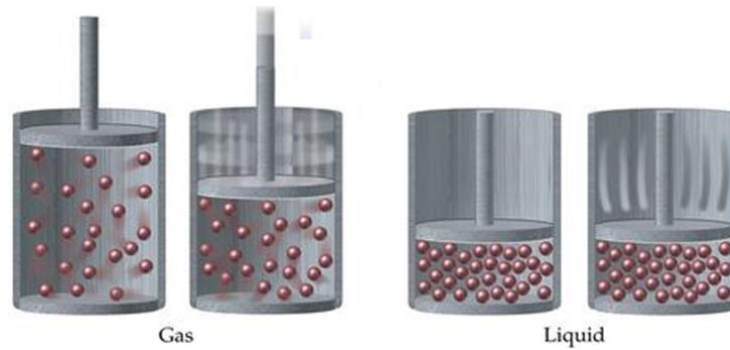
Gas   Liquid

Figure 2.3 Gas VS liquid phase compressibility factor

Based on the aforementioned equations, the updated hydrate, liquid and gas saturations ($S_h{}^u$, $S_l{}^u$ and $S_g{}^u$, respectively) can be written in terms of the current hydrate, liquid, and gas saturations (S_h, S_l and S_g, respectively), compressibility coefficients and saturations, as follows:

$$S_h^u = S_h - dS_h \tag{15}$$

$$S_l^u = \left(S_l + \alpha \frac{\rho_h}{\rho_l} dS_h \right) \left(1 - \frac{K_l \left(R_V dS_h \right)}{K_{eq} \left(S_l + S_g \right)} \right) \tag{16}$$

$$S_g^u = \left(S_g + \left(1 - \alpha \right) \frac{\rho_h}{\rho_g} dS_h \right) \left(1 - \frac{K_g \left(R_V dS_h \right)}{K_{eq} \left(S_l + S_g \right)} \right) \tag{17}$$

3. NUMERICAL CODE: COUPLED THCM PROCESSES INVOLVING WITH GAS PRODUCTION FROM HBS

The coupled THCM numerical code is being developed to analyze problems involving HBS. The finite element (FE) computer program takes into consideration thermal and hydraulic processes in deformable sediments, and it also accounts for the changes in sediment properties in the presence of hydrate dissociation/formation. It is based on a fully coupled formulation that incorporates the different phases and species existing in HBS (including hydrate and ice) and it has been implemented in CODE_BRIGHT (Olivella et al., 1996), an existing coupled multiphysics program for geological media.

As illustrated in Figure.3.1, five phases including solid, liquid, gas, ice, and hydrate, which are composed by three species of minerals, water, and methane are considered in this framework. Also, the following components are considered in the analysis: balance equations, constitutive equations, and equilibrium restrictions. A brief explanation of these equations is presented below.
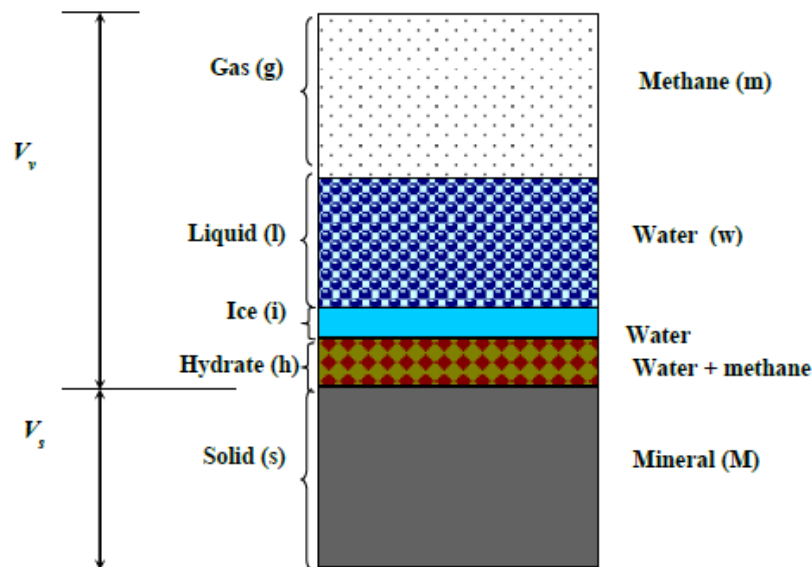
Figure 3.1 Components of HBS grouped into phases and species.

14

3.1. Balance Equations

The macroscopic balance of either mass or energy relates the rate of change per unit volume to the flux in and out of the volume, and takes into consideration external inputs as well (Figure.3.2). The mass flux in balance equations includes advective transport by the fluid and the movement of the sediment relative to a fixed reference frame. The proposed framework can also accommodate non-advective diffusive transport of species in the phases (i.e. w in g, and m in l) as discussed in Olivella et al. (1994).

The mass of water per unit volume of the porous medium consists of the mass of water in the liquid, hydrate, and ice phases. The water flux associated to the liquid, hydrate, and ice phases with respect to a fixed reference system includes Darcian flow with respect to the solid phase $q_l \left[\frac{L}{t}\right]\left(\frac{m}{\text{Sec}}\right)$ and the motion of the whole sediment with velocity $\dot{u}\left[\frac{L}{t}\right]\left(\frac{m}{\text{Sec}}\right)$ relative to the fixed reference system. Therefore, the water mass balance can be expressed as:

$$\frac{\partial}{\partial t}[(\rho_l S_l + \alpha \rho_h S_h + \rho_i S_i)\varphi] + \nabla.[\rho_l q_l + \rho_l S_l \varphi \dot{u} + \alpha \rho_h S_h \varphi \dot{u} + \rho_i S_i \varphi \dot{u}] = f^w \tag{18}$$

where $\rho_l \left[\frac{M}{L^3}\right]\left(\frac{Kg}{m^3}\right)$, ρ_h, and ρ_i represent the mass density of liquid, hydrate, and ice phase respectively. S_β $(\beta = l,h,i)$ indicates the phase saturation, α is the mass fraction of water in hydrate, and $f^w \left[\frac{M}{L^3 t}\right]\left(\frac{Kg}{m^3 \text{Sec}}\right)$ stands for the external water mass supply per unit volume of the medium.
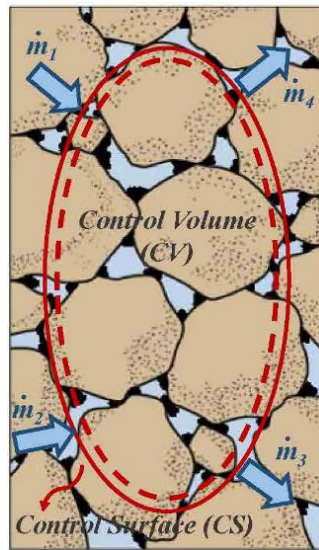
Figure 3.2 Control volume (CV) for calculating the mass balance equation.

15

The total mass of methane per unit volume of the HBS is computed by adding the mass of methane per unit volume of the gas and hydrate phases taking into consideration the volume fraction S_g and S_h, the mass fraction of methane in hydrate $(1-\alpha)$, and the porosity of porous medium φ. As in the case of water balance, the flux of methane in each phase combines advective terms relative to the porous matrix and the motion of the porous medium with velocity relative to the fixed reference system:

$$\frac{\partial}{\partial t}[(\rho_g S_g + (1-\alpha)\rho_h S_h)\varphi] + \nabla.[\rho_g q_g + \rho_g S_g \varphi \dot{u} + (1-\alpha)\rho_h S_h \varphi \dot{u}] = f^m \tag{19}$$

In this case, $f^m \left[\frac{M}{L^3 t}\right]\left(\frac{Kg}{m^3 \, \text{Sec}}\right)$ is an external supply for methane, expressed in term of mass of methane per unit volume of the porous medium.

The mineral species is only found in the solid phase. The mass balance equation follows:

$$\frac{\partial}{\partial t}[\rho_s (1-\varphi)] + \nabla.[\rho_s (1-\varphi)\dot{u}] = 0 \tag{20}$$

where $\rho_s \left[\frac{M}{L^3}\right]\left(\frac{Kg}{m^3}\right)$ is the mass density of the minerals that make the soil particles.

The energy balance equation is considered as a function of internal energy per unit volume, assuming that all phases are in equilibrium at the same temperature. Also, energy consumption or liberation associated to hydrate dissociation/formation and ice melting/formation are taken into consideration using the corresponding latent heats or changes in enthalpy. Therefore, the formulation inherently captures energy changes during endothermic or exothermic processes through specific internal energies and the corresponding changes in volume fractions.

The energy flux consists of conducting through the HBS, $i_c \left(\frac{W}{m^2}\right)$, transport by fluid mass advection relative to the mineral skeleton, and transport by the motion of the whole sediment with respect to the fixed reference system. The energy balance equation taking into consideration transport through the phases is:

16

$$\frac{\partial}{\partial t}\left[\left(e_s\rho_s(1-\varphi)\right)+\left(e_l\rho_l S_l+e_g\rho_g S_g+e_h\rho_h S_h+e_i\rho_i S_i\right)\varphi\right]+\nabla i_c$$

$$+\nabla\left[e_s\rho_s(1-\varphi)\dot{u}+e_l\rho_l\left(q_l+S_l\varphi\dot{u}\right)+e_g\rho_g\left(q_g+S_g\varphi\dot{u}\right)+e_h\rho_h S_h\varphi\dot{u}+e_i\rho_i S_i\varphi\dot{u}\right]=f^E \qquad (21)$$

where $e\left[\dfrac{J}{g}\right]$ stands for the specific internal energy per unit mass of each phase and $f^E\left[\dfrac{W}{m^3}\right]$ is

the energy supply per unit volume of HBS.

3.2. Constitutive Equations

The governing equations are finally considered in terms of the unknowns when constitutive equations that relate unknowns to dependent variables are substituted in the balance equations. Given the complexity of the problem, simple yet robust constitutive laws are selected for this simulation.

The advective fluxes of the liquid and the gas phases q_l and $q_g\left[\dfrac{L}{t}\right]\left(\dfrac{m}{\text{Sec}}\right)$ are computed using the generalized Darcy's law (Gens & Olivella, 2001):

$$q_\alpha=-K_\alpha\left(\nabla P_\alpha-\rho_\alpha\mathbf{g}\right)\qquad\qquad \alpha=\ell,g \qquad\qquad (22)$$

where $P_\alpha\left(\dfrac{N}{m^2}\right)$ is the phase pressure, and the vector $\mathbf{g}$ is the scalar gravity $g=9.8$ m/s^2 times the vector $[0,0,1]^T$. The tensor $K_\alpha\left(\dfrac{m^4}{N\,\text{Sec}}\right)$ captures the medium permeability for the α-phase; if the medium is isotropic, K_α is the scalar permeability K_α times the identity matrix. The permeability K_α depends on the intrinsic permeability $k\left[L^2\right]\left(m^2\right)$ of the medium, the dynamic viscosity of the α-phase $\mu\alpha\left(\dfrac{N\,\text{Sec}}{m^2}\right)$ and the relative permeability $k_{r\alpha}$ [-]:

$$K_\alpha=\mathbf{k}\frac{k_{r\alpha}}{\mu_\alpha} \qquad\qquad (23)$$

Methane and water densities, which are equal to the gas and liquid phase densities correspondingly, highly depend on pressure P (MPa) and temperature T (°C), while the

dependency of solid hydrate density (ρ_h=900kg/m^3) on variation of pressure and temperature is negligible.

$$\rho_l = \rho_w = \rho_{w_0}\left(1+\frac{P}{\beta_l}\right)\left(1-\beta_{T_l}\left[\frac{(T+273.15)-277}{5.6}\right]^2\right) \tag{24}$$

where $\rho_{w_0} = 999.8$ (kg/m^3), $\beta_l = 2000$ (MPa) and $\beta_{T_l} = 0.0002\,^\circ K^{-1}$.

$$\rho_g = \rho_m = \frac{M_m.P}{R(T+273.15)}\left[1176+12.7\left(\frac{P}{P_{ref}}\right)-0.45\left(\frac{P}{P_{ref}}\right)^2\right] \tag{25}$$

where M_m=16.042 g/mole; R=8.314 J/(mol°K), and P_{ref}=1(MPa)

The viscosity of the liquid phase $\mu_l\left(Pa.\text{Sec}\right)$ varies with temperature T (°K) (i.e. Olivella, 1995):

$$\mu_\ell = 2.1\cdot10^{-6}\exp\left(\frac{1808.5\,^\circ K}{T}\right) \tag{24}$$

While the viscosity of gases is often assumed independent of pressure, experimental data in the wide pressure range of interest shows otherwise. Published data in Younglove & Ely (1987) are fitted to develop a pressure and temperature dependent expression for the viscosity of methane gas (fitted range: 270°K<T<290°K and 0.1MPa<P_g<40MPa).

$$\mu_g = 10.3\cdot10^{-6}\left[1+0.053\frac{P_g}{\text{MPa}}\left(\frac{280\,^\circ K}{T}\right)^3\right] \tag{25}$$

The relative permeability coefficients for liquid $k_{r\ell}$ and gas k_{rg} increase as the degree of saturation of each phase increases with respect to the mobile phase saturation, $S_\ell+S_g$. A single parameter power function properly reproduces experimental data.

$$k_{r\ell} = \left(\frac{S_\ell}{S_\ell+S_g}\right)^a = \left(S_\ell^*\right)^a \tag{26}$$

$$k_{rg} = \left(1-\frac{S_\ell}{S_\ell+S_g}\right)^b = \left(1-S_\ell^*\right)^b \tag{27}$$

where S_ℓ^* is the effective liquid saturation in the hydrate bearing sediment.

Implementing aforementioned equations for the phase relative permeability for the full range of effective liquid and gas saturation causes some numerical errors for the case of fully saturated and oven dry porous medium. For instance, consider the case of fully saturated soil in which the gas saturation should be equal to zero. Consequently, the gas relative permeability calculated based on the classical power law is zero. Therefore, if there is any perturbation in fluid pressure, assume depressurization, the liquid pressure will be modified, decreases, according to the liquid flow, however the gas pressure remains constant because of the zero/negligible gas relative permeability, which results in spurious gas saturation as a result of spurious capillary pressure. This problem is common in the study of coupled processing in porous media (Zhang et al. 2016). In order to avoid the numerical error for these extreme conditions, the validation of classical models is restricted to the range of effective saturation bounded by critical values (e.g. Webb (2000) modified the classical capillary pressure suggested by Brooks & Corey (1966) and Van Genuchten (1980) for the oven dry condition).

In this study, the same problem happens for the condition of a fully saturated porous medium. Consider a case of depressurization in the HBS in which the P-T conditions are still favorable for hydrate stability. Perturbation of liquid pressure is propagated through reservoir while the gas pressure is not affected by the depressurization due to the negligible gas relative permeability. Furthermore, the capillary pressure generated by a considerable difference in the value of gas and liquid pressure reports the non-zero gas saturation prior to hydrate dissociation. To cope with this problem in the numerical analysis, the classical power law for the gas relative permeability is modified as follows:

$$k_{rg} = \begin{cases} k_{rl} & S_g^* < S_{min} \\ \left(\dfrac{S_{min}}{S_g^*}\right)^m k_{rl} & S_{min} < S_g^* < nS_{min} \\ \left(1 - S_l^*\right)^b & nS_{min} < S_g^* \end{cases} \tag{28}$$

in which the value of liquid relative permeability is used for the gas relative permeability when the effective gas saturation is lower than the predefined minimum value for phase saturation and the classical power law is implemented for the range of effective gas saturation while its value is

19

higher than the n times of predefined minimum value. For the range of effective gas saturation between these two intervals, the gas relative permeability is a factor of the classical liquid relative permeability. This factor is considered to satisfy the continuity of the gas relative permeability on the whole range of gas saturation.

Figure.3.3 shows the classical power functions, the cubic law ($a=b=3$), for liquid and gas relative permeability. Also, the extended classical model for the gas relative permeability based on the parameters indicated in Table.3.1 is included for the sake of comparison.
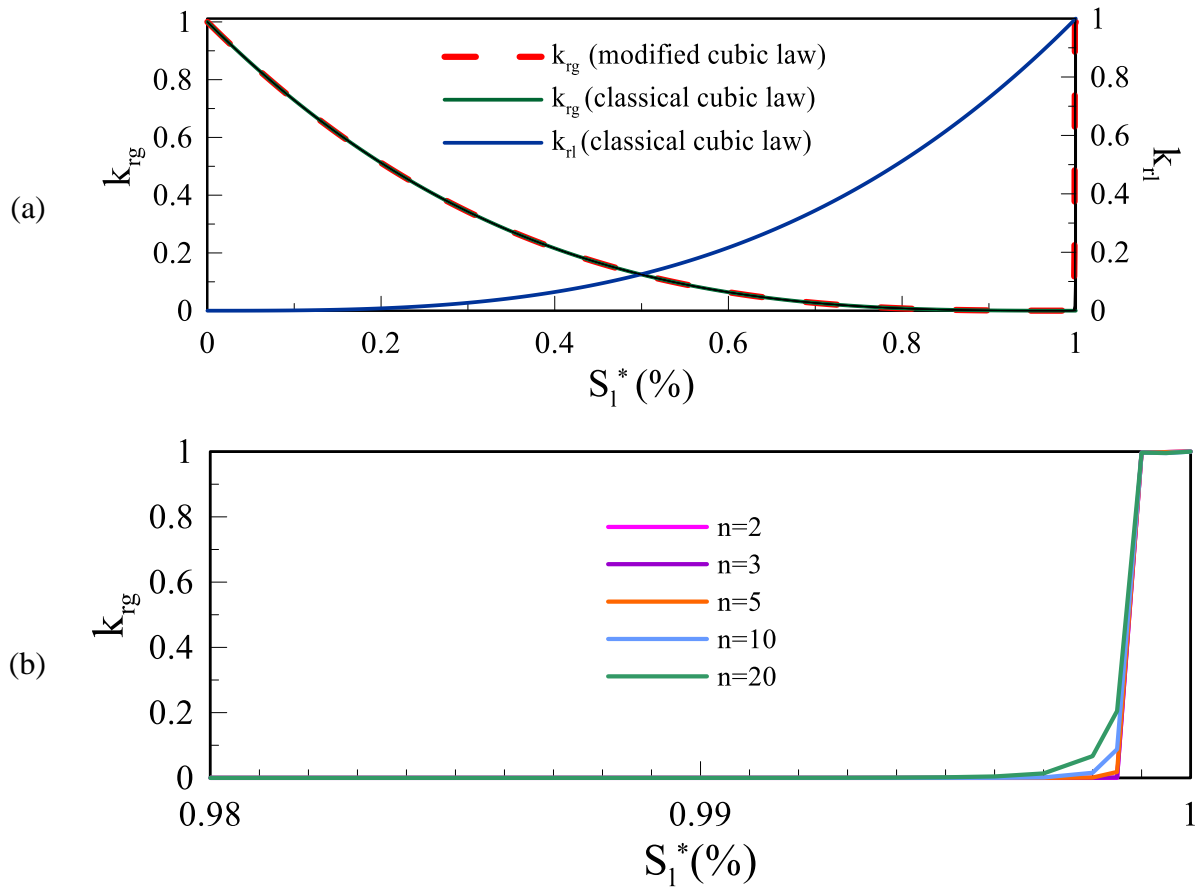
Figure 3.3 (a) Liquid and gas relative permeability based on the classical and modified cubic power law VS effective liquid saturation; (b) description of the gas relative permeability based on the modified cubic power law for different value of n, according to $S_{min}=0.001$ and the pertinent value of m shown in Table.3.1.

Table 3-1 Pertinent parameters for the modified cubic law based on $S_{min}=0.001$.

n	m
2	26.889
3	15.855
5	9.867
10	5.987
20	3.897

The hydraulic conductivity of sediments is highly affected by ice saturation, hydrate concentration, and hydrate morphology. Therefore, the modified permeability coefficient in HBS can be written as:

$$k_{HBS} = k_{Sed} \left(1 - S_h - S_i\right)^N \tag{29}$$

where N [-] is related to hydrate deposit morphology.

The interfacial tension between liquid and gas sustains the difference between the liquid and gas pressures P_ℓ and P_g. The capillary pressure and the effective liquid saturation S_ℓ^* are related (Van Genuchten, 1978):

$$S_\ell^* = \frac{S_\ell}{S_\ell + S_g} = \left[1 + \left(\frac{P_c}{P_o}\right)^{\frac{1}{1-\lambda}}\right]^{-\lambda} \tag{30}$$

where P_c is the capillary pressure, P_o, and λ are model parameters.

3.3. Phase Boundaries

Pressure and temperature define the phase boundary for methane hydrate and ice. The selected expression for the phase boundary of methane follows the format in Sloan & Koh (2008), but it is adjusted to satisfy values computed using the HWHYD software (2001).

$$P_{eq} = e^{\left(40.234 - \frac{8860}{T_{eq}[°K]}\right)} \tag{31}$$

where P_{eq} is the equilibrium pressure (KPa). Local equilibrium conditions are attained much faster than the duration of the global process in most THCM problems.

Moreover, the salinity of water affects the phase boundary of gas hydrate mixture. According to Kamath & Godbole (1987) studies, a linear relationship between the temperature of dissociation and the salinity weight concentration for a given pressure is assumed. The aforementioned equation is modified to account for the effect of salinity on hydrate phase boundary.

$$P_{eq} = e^{\left(40.234 - \frac{8860}{T_{eq} - \alpha_s I_s}\right)}$$

(32)

in which, α_s represents the slope of the temperature-salinity curve and I_s stands for the salinity weight concentration.

The phase boundary for ice-water transition, which exhibits low sensitivity to pressure is considered according to the equation provided by Wagner & Kretzschmar (2008):

$$P_{eq-ice} = 13.0\left(273.16 - T[°K]\right)$$

(33)

where P_{eq-ice} is the equilibrium pressure (*MPa*).

As illustrated in Figure.3.4, aforementioned two phase boundaries divide the pressure-temperature *P-T* space in four regions.
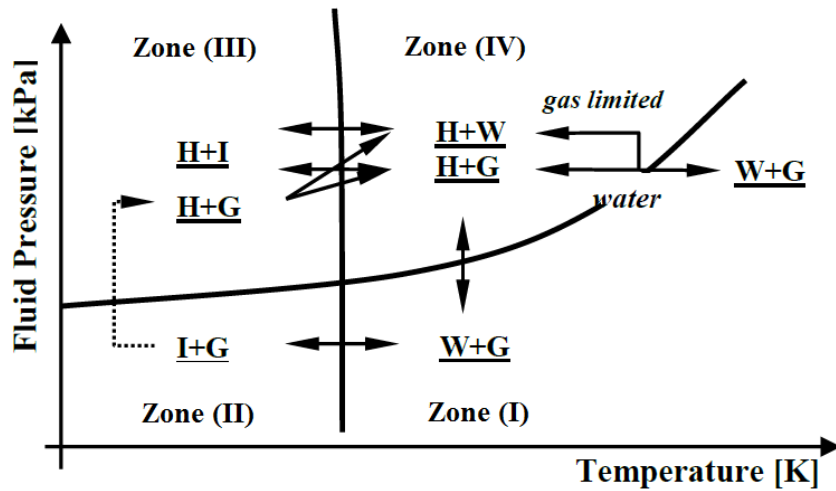
Figure 3.4 Four regions emerge when the ice-water and the hydrate stability phase boundary are superimposed on the pressure-temperature P-T space.

3.4. Pseudo Kinetic Model

A novel pseudo kinetic model for hydrate dissociation/formation and ice melting/formation is used. Based on this model, the rate of hydrate dissociation/formation and ice melting/formation is driven by the distance δ from the corresponding equilibrium phase boundary.

$$\delta = \sqrt{\left[\delta_T \left(T - T_{eq}\right)\right]^2 + \left[\delta_P \left(P - P_{eq}\right)\right]^2} \tag{34}$$

in which $\delta_T \left(°K^{-1}\right)$ and $\delta_P \left(MPa^{-1}\right)$ are scaling parameters and T_{eq} and P_{eq} are the corresponding temperature and pressure on phase boundary. The variation in phase saturations due to hydrate/ice formation/dissociation at each time step is a fraction $0 \leq \xi \leq 1$ of the potential change. This reduction factor is calculated based on the factor β, which is a rate of change, the phase saturation of the potential change (S_α), and the duration of the current time step $(dtime)$. The factor β is described as a function of the distance from the phase boundary.

$$\beta = 1 - q^\delta \tag{35}$$

where q is the parameter, which establishes the rate of change β. Therefore the updated saturation of the phase, which is not in the stable condition on the P-T space, at the current time step with duration of $dtime$ follows:

$$S_\alpha^u = S_\alpha \left(1 - \left(\frac{\beta}{S_\alpha}\right) dtime\right) = S_\alpha \left(1 - \xi\right) \tag{36}$$

3.5. Phase Transitions

In this study, two different methods are used to calculate the phase transitions as a result of hydrate/ice dissociation/formation. In the first method, the concept of the capillary pressure has been used to split the effective void volume, the portion of void volume occupied by the fluid phases, between the liquid and gas phases. In the second method, which is based on the single fluid pressure, the phase transitions are considered based on the mass amount of consumed/released water and methane due to the hydrate formation/dissociation respectively.

3.5.1. Phase Transitions Based on The Capillary Pressure

Since both ice and liquid phases are formed by the water species, the phase transition between these two is straightforward. However, splitting the partial volume of hydrate, which is dissociated to liquid water and methane gas, between the liquid and gas phases needs an additional effort. The same issue happens in the hydrate formation.

The effective void volume φ^* is defined as the portion of the porosity φ, which is occupied by the fluid phases (the liquid and gas phases). This portion is updated based on the hydrate/ice formation/dissociation at each time-step.

$$\varphi^* = \left[1 - \left(S_h + S_i\right)\right] = \left(S_l + S_g\right) \tag{37}$$

The partial of effective void volume, which is filled by liquid phase is known as the effective liquid saturation S_l^* and with a same trend the effective gas saturation S_g^* is calculated.

$$S_l^* = \frac{S_l}{S_l + S_g} \tag{38}$$

$$S_g^* = \frac{S_g}{S_l + S_g} = \left(1 - S_l^*\right) \tag{39}$$

According to Van Genuchten (1978), as shown previously in Eq. (30), the distribution of effective liquid and gas saturations in the effective void volume is a function of the capillary pressure. Therefore the volumetric amount of consumed/released fluid phases due to hydrate formation/dissociation should obey this distribution at any specified time-step. In following, any probable phase transitions corresponding to each zone, illustrated in Figure.3.4, will discuss.

At any specified temperature, if the pressure is below the equilibrium pressure with respect to the hydrate stability phase boundary, which is located in zone (I) or (II) on the P-T space, the hydrate dissociation occurs. According to the aforementioned pseudo kinetic model, the hydrate saturation and the effective void volume will be updated at each time-step as follows:

24

$$S_h^{i+1} = S_h^i \left(1 - \left(\frac{\beta}{S_h^i} \right) dtime \right) \tag{40}$$

$$\varphi *^{(i+1)'} = \left[1 - \left(S_h^{i+1} + S_i^i \right) \right] \tag{41}$$

Then by having the effective fluid phase saturation from retention curve, the updated liquid and gas saturation due to hydrate dissociation will be derived as:

$$S_l^{(i+1)'} = S_l^* \left(\varphi *^{(i+1)'} \right) = S_l^* \left[1 - \left(S_h^{i+1} + S_i^i \right) \right] \tag{42}$$

$$S_g^{i+1} = S_g^* \left(\varphi *^{(i+1)'} \right) = \left(1 - S_l^* \right) \left[1 - \left(S_h^{i+1} + S_i^i \right) \right] = 1 - \left(S_h^{i+1} + S_l^{(i+1)'} + S_i^i \right) \tag{43}$$

Notation *(i+1)'* in the superscript of the effective void volume and the liquid saturation indicates that they are not the final values at the current time-step. The values will be finalized after considering the ice formation/melting.

The pressure and temperature conditions in zone (III) and (IV) on the P-T space are favorable for the stability of the hydrate phase. Therefore, if both methane and water are available, the hydrate is forming, which leads to decreasing the partial void volume occupied by fluid phases. Based on hydrate formation, the phase saturation will be updated as follows:

$$\varphi *^{(i+1)'} = \varphi *^i \left[1 - \xi \right] \tag{44}$$

$$S_h^{i+1} = S_h^i + \left(\varphi *^i - \varphi *^{(i+1)'} \right) = S_h^i + \varphi *^i \ \xi \tag{45}$$

$$S_l^{(i+1)'} = S_l^* \left(\varphi *^{(i+1)'} \right) = S_l^* \left[1 - \left(S_h^{i+1} + S_i^i \right) \right] \tag{46}$$

$$S_g^{i+1} = S_g^* \left(\varphi *^{(i+1)'} \right) = \left(1 - S_l^* \right) \left[1 - \left(S_h^{i+1} + S_i^i \right) \right] = 1 - \left(S_h^{i+1} + S_l^{(i+1)'} + S_i^i \right) \tag{47}$$

in which fraction ξ is calculated based on either the case of excess water or the case of excess methane. Excess water is the case in which the available water is higher than the required amount to form hydrate with respect to the existing methane and oppose to this case, in the case of excess methane, the available methane is higher than the required to consume with potential water for hydrate formation. The case determination of excess methane or excess water depends on parameter δ' which is defined in Eq. (48).

$$\delta' = \frac{\alpha}{1-\alpha} \tag{48}$$

$$\frac{\rho_l S_l^i}{\rho_g S_g^i} > \delta' \to ExcessWater: \; \xi = \left(\frac{\beta}{S_g^i}\right) dtime \tag{49}$$

$$\frac{\rho_l S_l^i}{\rho_g S_g^i} < \delta' \to ExcessMethane: \; \xi = \left(\frac{\beta}{S_l^i}\right) dtime \tag{50}$$

It is important to consider that the amount of change in the effective void volume should not be higher than the existing gas/liquid saturation in the case of excess water/methane respectively.

After updating the hydrate, liquid, and gas saturations due to the probable hydrate formation/dissociation with respect to the corresponding phase boundary at each time-step, the liquid and ice saturations are modified by considering the ice stability phase boundary.

The existence of liquid phase under the P-T condition located in zone (II) and (III) is a potential for water freezing. Consequently, the ice and liquid saturations are modified as follows:

$$S_l^{i+1} = S_l^{(i+1)'}\left(1 - \left(\frac{\beta'}{S_l^{(i+1)'}}\right) dtime\right) \tag{51}$$

$$S_i^{i+1} = S_i^i + S_l^{(i+1)'}\left(\frac{\beta'}{S_l^{(i+1)'}}\right) dtime \tag{52}$$

in which β' is the rate of change due to the ice stability phase boundary and calculated according to Eq. (35).

Under the P-T condition prevailed in zone (I) and (IV), the existence of the ice phase is a potential to melt the ice and to make an increment in the liquid phase, which needs implementing the following modifications.

$$S_i^{i+1} = S_i^i\left(1 - \left(\frac{\beta'}{S_i^i}\right) dtime\right) \tag{53}$$

$$S_l^{i+1} = S_l^{(i+1)'} + S_i^i\left(\frac{\beta'}{S_i^i}\right) dtime \tag{54}$$

By having the updated saturation of all phases after considering both phase boundaries of methane and ice, the final value for the effective void volume can be derived.

$$\varphi *^{i+1} = \left[1 - \left(S_h^{i+1} + S_i^{i+1}\right)\right] = \left(S_l^{i+1} + S_g^{i+1}\right) \tag{55}$$

In all aforementioned equations, the minimum value should be considered for phase saturation. If any of the modified saturations in the time step ($i+1$) gets lower than this minimum value, calculation should be terminated.

3.5.2. Phase Transitions Based on Single Fluid Pressure

In this method, the ice and hydrate phase saturations will be updated based on the thermodynamic conditions, the single fluid pressure and the temperature, with respect to the corresponding phase boundaries. Consequently, saturation of the fluid phases will be affected by any variations in the ice and hydrate phases. Based on the molecular structure of methane hydrate, the mass of liquid water and methane gas which are consumed/released due to the formation/dissociation can be derived.

Eq. (56) represents the mass balance equation of the liquid phase, which only contains the species of water.

$$\frac{\partial}{\partial t}\left[\rho_w S_l^* \varphi^* \varphi\right] + \nabla \cdot \left[\rho_w q_l + \rho_w S_l^* \varphi^* \varphi \overset{\square}{u}\right] = f^l \tag{56}$$

where φ^* and S_l^* are the effective porosity and the effective liquid saturation respectively.

Therefore, the variation of effective liquid saturation will be derived.

$$\frac{DS_l^*}{Dt} = \frac{f_l}{\varphi^* \varphi \rho_l} - S_l^*\left(\frac{1}{\varphi^*}\frac{D\varphi^*}{Dt} + \frac{1}{\varphi}\frac{D\varphi}{Dt} + \frac{1}{\rho_l}\frac{D\rho_l}{Dt} + \nabla \cdot \overset{\square}{u}\right) - \frac{1}{\varphi^* \varphi}\nabla \cdot q_l - \frac{q_l}{\rho_l \varphi^* \varphi}\nabla \rho_l \tag{57}$$

By assuming the rigidity for the porous medium skeleton, the negligible variation of water density, and no erosion in solid phase, the aforementioned equation is simplified as follows:

$$\frac{\partial S_l^*}{\partial t} = \frac{1}{\varphi^*}\left(\frac{f^l}{\varphi \rho_w}\right) - S_l^*\left(\frac{1}{\varphi^*}\frac{\partial \varphi^*}{\partial t}\right) - \frac{1}{\varphi^* \varphi}\nabla \cdot q_l \tag{58}$$

in which f^l stands for a source/sink including an internal production/consuming liquid water due to any hydrate/ice dissociation/formation.

In following, the framework of how to calculate the variation of the ice and hydrate phase saturation and consequently the internal producing/consuming liquid water, f^l, due to the transition between different zones on the P-T space based on the aforementioned pseudo kinetic model and also according to the concept of volume expansion/contraction as a result of hydrate dissociation/formation is explained. It is worth noting that since the compressibility of liquid phase is considerably smaller than that of gas phase, it is assumed that volume compression/contraction is compensated by gas phase.

Zone (I) is defined by conditions in which pore pressure is lower than the equilibrium pressure on the methane hydrate stability phase boundary with respect to the corresponding temperature while temperature is greater than the equilibrium temperature on the ice-water phase boundary at the given pressure. Therefore, the stable phases in this zone are liquid and gas. This condition leads to dissociating hydrate and melting ice phases. Updated saturation of each phases due to hydrate/ice melting at current time step ($i+1$) is calculated based on the known phase saturation in previous time step (i) through following equations.

$$S_h^{i+1} = S_h^i \left(1 - \left(\frac{\beta}{S_h^i} \right) dtime \right) \tag{59}$$

$$S_i^{i+1} = S_i^i \left(1 - \left(\frac{\beta'}{S_i^i} \right) dtime \right) \tag{60}$$

$$S_l^{i+1} = \left(S_l^i + \left(\frac{\beta}{S_h^i} \right) dtime \left(S_h^i \right) \alpha \frac{\rho_h}{\rho_l} + \left(\frac{\beta'}{S_i^i} \right) dtime \left(S_i^i \right) \frac{\rho_i}{\rho_l} \right) \tag{61}$$

where α is the water mass fraction in hydrate solid compound. Also β and β' are determined based on Eq. (35) with respect to hydrate stability and ice-water phase boundary respectively.

The conditions in which pressure is lower than the equilibrium pressure with the corresponding temperature on the methane hydrate stability phase boundary and also temperature is lower than the equilibrium temperature at the given pressure on the ice-water phase boundary define zone (II). Since ice and gas phases are stable in this zone, any hydrate will dissociate and any liquid water will freeze.

28

$$S_h^{i+1} = S_h^i \left(1 - \left(\frac{\beta}{S_h^i} \right) dtime \right) \tag{62}$$

$$S_i^{i+1} = \left(S_i^i + \left(\frac{\beta'}{S_l^i} \right) dtime \left(S_l^i + \left(\frac{\beta}{S_h^i} \right) dtime \left(S_h^i \right) \alpha \frac{\rho_h}{\rho_l} \right) \frac{\rho_l}{\rho_i} \right) \tag{63}$$

$$S_l^{i+1} = \left(S_l^i + \left(\frac{\beta}{S_h^i} \right) dtime \left(S_h^i \right) \alpha \frac{\rho_h}{\rho_l} \right) \left(1 - \left(\frac{\beta'}{S_l^i} \right) dtime \right) \tag{64}$$

Prevailing conditions for zone (III) happen when pressure is higher than the equilibrium pressure on the hydrate stability phase boundary at the corresponding temperature while temperature is lower than the equilibrium temperature on the ice-water phase boundary at the given pressure. Ice and hydrate phases are stable in this zone. Therefore, any probable water will freeze, but since water is required for hydrate formation, no hydrate will form in this zone. The modified saturation due to ice formation at the current time step (*i+1*) will derived based on saturations in previous time step (*i*) according to following equations.

$$S_h^{i+1} = S_h^i \tag{65}$$

$$S_i^{i+1} = \left(S_i^i + \left(\frac{\beta'}{S_l^i} \right) dtime \left(S_l^i \right) \frac{\rho_l}{\rho_i} \right) \tag{66}$$

$$S_l^{i+1} = S_l^i \left(1 - \left(\frac{\beta'}{S_l^i} \right) dtime \right) \tag{67}$$

The favorable conditions of zone (IV) are described by pore pressure higher than the equilibrium pressure according to the corresponding temperature on the methane hydrate stability phase boundary and also temperature higher than the equilibrium temperature at the given pressure on the ice-water phase boundary. Consequently, hydrate phase is stable while ice phase is unstable under this condition. Two different cases may happen in zone (IV): the case of excess water and the case of excess methane. If the amount of water species is higher than the required amount for hydrate formation with the existing methane species, then after consuming that available methane, the excess amount of water remains in liquid phase. The same scenario happens for the amount of excess methane, which remains in gas phase. The case determination of excess methane or excess water depends on parameter δ' which is defined in Eq. (68). Modified phase saturations in both

cases of excess water and excess methane due to hydrate formation and ice thawing are described respectively as follows:

$$\delta' = \frac{\alpha}{1-\alpha} \tag{68}$$

$$\frac{\rho_l S_l^i}{\rho_g S_g^i} > \delta' \rightarrow ExcessWater: \tag{69}$$

$$S_h^{i+1} = \left(S_h^i + \left(\frac{\beta}{S_g^i} \right) dtime \left(S_g^i \right) \left(\frac{1}{1-\alpha} \right) \frac{\rho_g}{\rho_h} \right) \tag{70}$$

$$S_i^{i+1} = S_i^i \left(1 - \left(\frac{\beta'}{S_i^i} \right) dtime \right) \tag{71}$$

$$S_l^{i+1} = \left(S_l^i - \left(\frac{\beta}{S_g^i} \right) dtime \left(S_g^i \right) \delta' \frac{\rho_g}{\rho_l} + \left(\frac{\beta'}{S_i^i} \right) dtime \left(S_i^i \right) \frac{\rho_i}{\rho_l} \right) \tag{72}$$

$$\frac{\rho_l S_l^i}{\rho_g S_g^i} < \delta' \rightarrow ExcessMethane: \tag{73}$$

$$S_h^{i+1} = \left(S_h^i + \left(\frac{\beta}{S_l^i} \right) dtime \left(S_l^i \right) \frac{1}{\alpha} \frac{\rho_l}{\rho_h} \right) \tag{74}$$

$$S_i^{i+1} = S_i^i \left(1 - \left(\frac{\beta'}{S_i^i} \right) dtime \right) \tag{75}$$

$$S_l^{i+1} = S_l^i \left(1 - \left(\frac{\beta}{S_l^i} \right) dtime \right) + \left(\frac{\beta'}{S_i^i} \right) dtime \left(S_i^i \right) \frac{\rho_i}{\rho_l} \tag{76}$$

In all aforementioned equations, the minimum value should be considered for phase saturation. If any of the modified saturations in the time step ($i+1$) gets lower than this minimum value, calculation should be terminated.

Accordingly, an internal production/consuming liquid water due to any hydrate/ice dissociation/formation is calculated at each time-step as follows:

$$S_l^{i+1} - S_l^i = \frac{f^l}{\varphi \rho_w} \tag{77}$$

As a result, the updated effective liquid saturation, S_l^{*u}, at the current time-step is calculated as:

$$S_l^{*u} = S_l^* + \frac{1}{\varphi^*} \left[\frac{f_1^l}{\varphi \rho_w} - \frac{dtime}{\varphi} (\nabla . q_l) \right] - S_l^* \left(\frac{\Delta \varphi^*}{\varphi^*} \right) \tag{78}$$

where $dtime$ and S_l^* are the duration of the current time-step and the liquid phase saturation at the previous time step respectively.

Consequently, the updated liquid and the gas saturation, S_l^u and S_g^u, at the current time-step are derived based on following equations:

$$S_l^u = \varphi^{*u} S_l^{*u} = \left(1 - \left(S_h^{i+1} + S_i^{i+1} \right) \right) S_l^{*u} \tag{79}$$

$$S_g^u = \varphi^{*u} \left(1 - S_l^{*u} \right) = 1 - \left(S_l^u + S_h^{i+1} + S_i^{i+1} \right) \tag{80}$$

3.6.Simulation

With featuring sound and proven constitutive relations and satisfying fundamental conservation principles, truly coupled numerical models were used to address the complex THCM coupled phenomena in HBS. Figure.3.5 illustrates the geometry and the properties of these simple 1D models.

Parameter	Value
Intrinsic permeability in *HBS*	$k_{HBS}=2\times10^{-12}\text{m}^2$ (Isotropic: $k_x=k_y=k_z$)
Dry thermal conductivity	$\lambda_{dry}=0.47$ W/(m.K)
Wet thermal conductivity	$\lambda_{sa}=1.15$ W/(m.K)
Porosity of *HBS*	$\phi=0.33$
Liquid relative permeability model	$a=3$
Gas relative permeability model	$b=3$
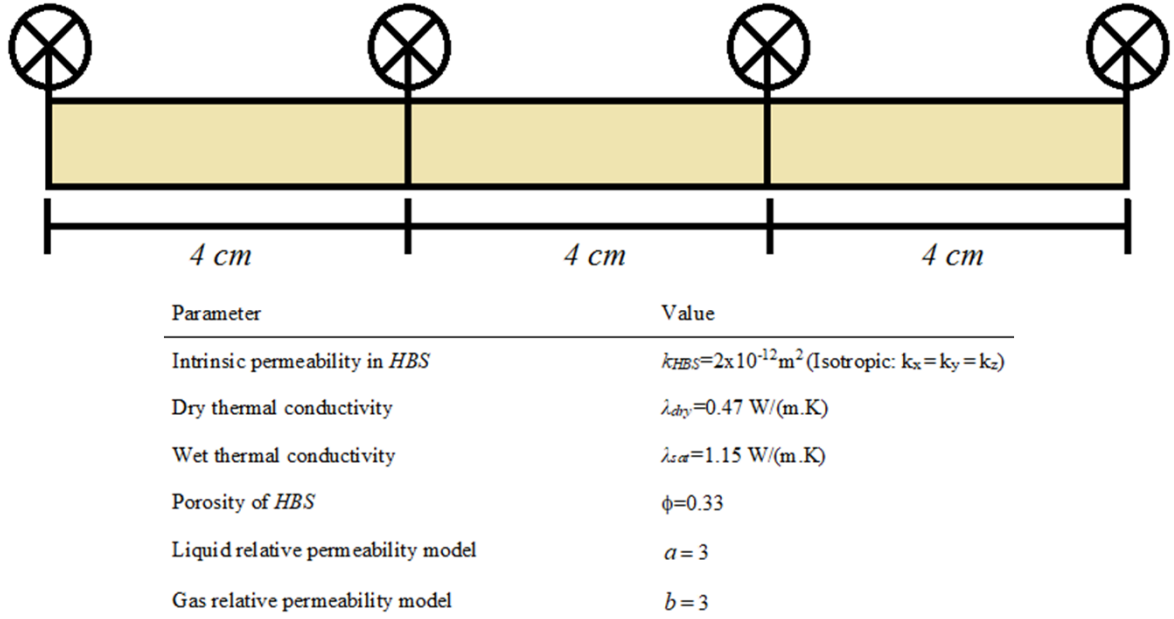
Figure 3.5 The geometry and general properties of simple 1D models.

Figure.3.6 illustrates the result of the case in which hydrate and ice are formed by decreasing temperature under a constant pressure condition. The P-T path starts form zone (I), then goes through zone (IV) and ends up in zone (III). Since pressure is assumed to be constant during hydrate formation, valves are opened and consequently flow in/out is allowed.

Hydrate formation by cooling method is also modeled under a constant volume condition, which is shown in Figure3.7. Similar to the previous case, hydrate is formed as the P-T path goes to zone (IV) form zone (I). Also, the remaining water freezes by passing form zone (IV) to zone (III).
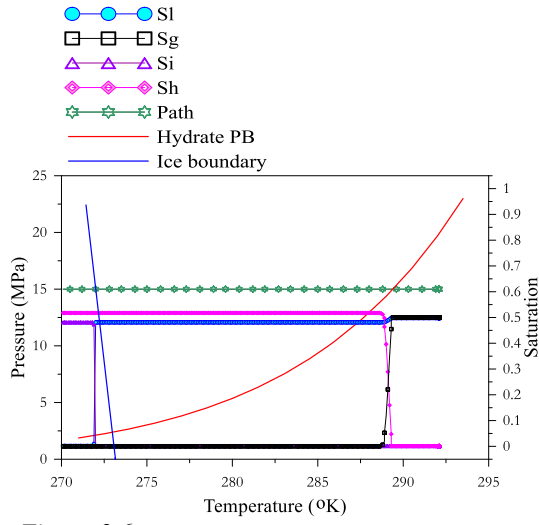
Figure 3.6 Hydrate formation at constant pressure.
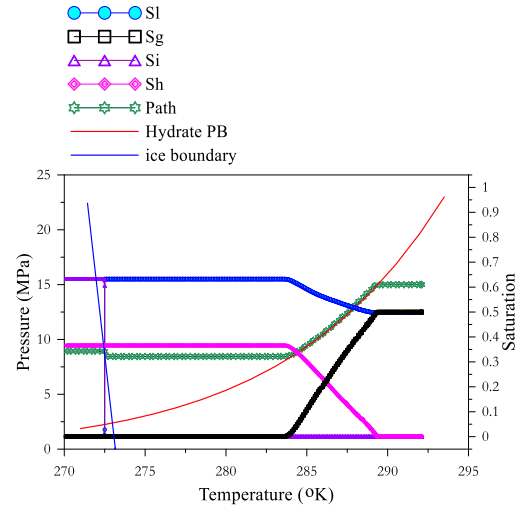
Figure 3.7 Hydrate formation at constant volume.
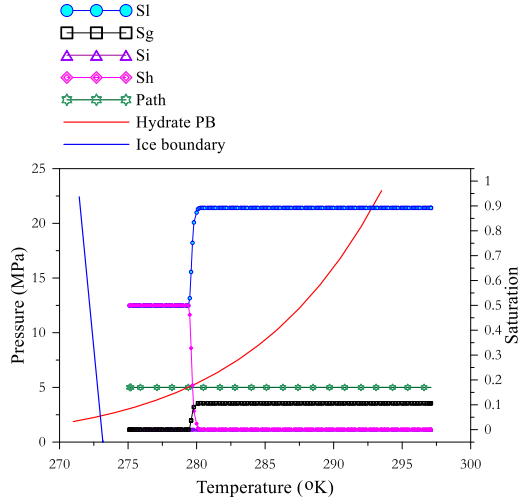
Figure 3.8 Hydrate dissociation induced by heat stimulation at constant pressure.
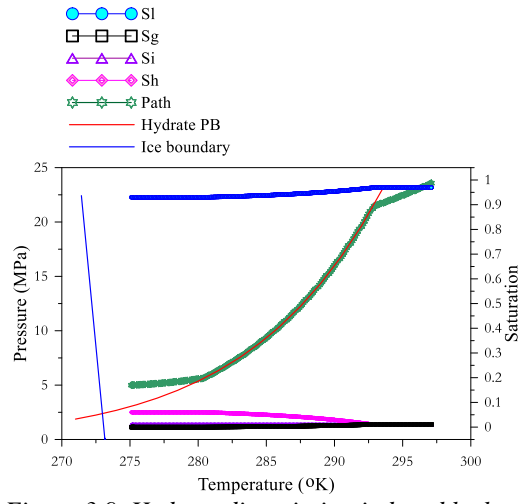
Figure 3.9 Hydrate dissociation induced by heat stimulation at constant volume.
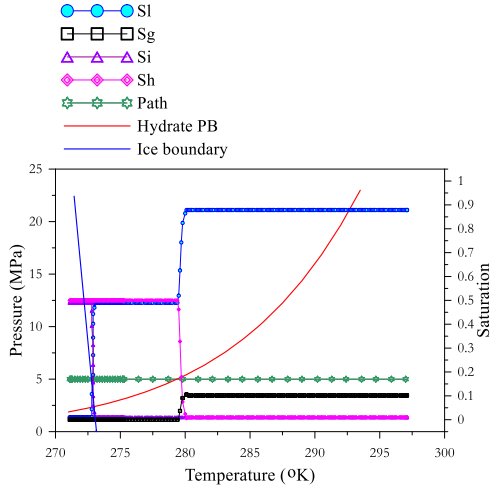
Figure 3.10 Hydrate dissociation induced by heat stimulation at constant pressure.
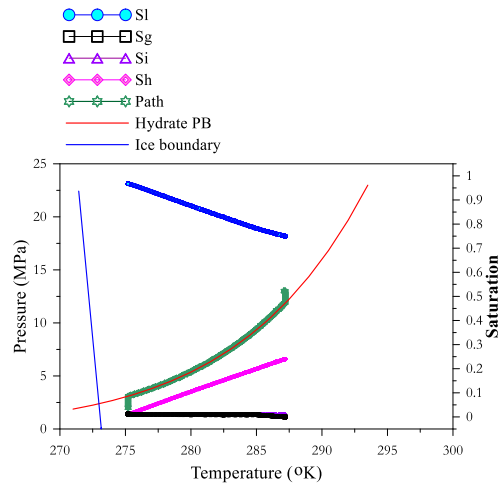
Figure 3.11 Hydrate dissociation induced by depressurization.

33

Figure.3.8 and Figure.3.9 represent the hydrate dissociation by heat stimulation in which initial pressure and temperature satisfy the prevailing conditions of zone (IV) and final conditions are in zone (I). Valves are opened during dissociation in the case shown in Figure.3.8 while they are closed for the other case illustrated in Figure.3.9.

In the case depicted in Figure.3.10, ice is melting when the P-T path passes zone (III) and goes to zone (IV). But since this case represents the excess water condition, no additional hydrate forms. Moreover, hydrate dissociates as the P-T path enters to zone (I). Both ice melting and hydrate dissociation are induced by heat stimulation under constant pressure.

Also, Results of hydrate dissociation induced by depressurization is shown in Figure.3.11.

The exothermic effect of formation and endothermic effect of dissociation are obviously shown in Figure.3.7, Figure.3.9 and Figure.3.11 on the P-T path.

All aforementioned data was verified with equations, which are explained in *Chapter.2* and derived by studying on natural behavior of HBS. The comparative results are very satisfactory.

3.7.Discussion

Numerical simulation of methane hydrate gas production is challenged by the complex behavior of HBS since hydrate dissociation comes along with interrelated THCM processes. Moreover, the potential ice formation during hydrate dissociation possess additional difficulties in numerical modeling. Complex stress paths in the P-T space with two phase boundaries (i.e. ice-liquid and gas-hydrate phase lines) are anticipated during gas production, including secondary ice and hydrate formation.

The fully coupled THCM numerical code, which incorporates the different phases and species existing in HBS including hydrate and ice has been developed to analyze gas production from HBS. This numerical analysis helps to expand the current knowledge in HBS; to address the issues associated with previous filed trial tests; to optimize/investigate the upcoming long term production strategies and implications.

Implementing the novel pseudo kinetic model paves the path to simulate the two-way phase transitions for both ice and hydrate and avoids complexities in the classical model.

34

Considering fully coupled THCM formulations instead of sequential methods makes the numerical analysis much more straightforward and accurate because of preventing linking two or more different numerical codes to study the problems involving HBS and avoiding one-way coupling, which cannot truly replicate the inherent behavior of HBS.

According to the presented framework, comprehensive 1D models are studied to address the inherent behavior of HBS and the proposed numerical code successfully captures the complex phenomena associated with hydrate formation/dissociation.

4. ANALYTICAL SOLUTION: PREDICTING THE MAXIMUM RECOVERABLE GAS FROM HBS

When solving engineering problems both transient and steady state analyses are relevant. Transient solutions are typically used, amongst others, to learn about gas production rate, to investigate optimal production strategies, and to perform sensitivity studies aimed at understanding the impact of material parameters (and other factors) on gas production. Steady state analyses are equally relevant because they demonstrate about the limit (or the final condition) of the problem under study.

In this chapter, an analytical solution is studied for the steady state condition involving fluid flow in an axisymmetric cylindrical geometry with various confining situations and accounting for the presence of two zones of different permeability coefficients for hydrate bearing sediments and free hydrate sediments within the reservoir. This solution can be very useful in problems encompassing HBS as it provides the physical limit to the zone around a well that can experience dissociation triggered by depressurization. From this solution, it is possible to learn about the maximum amount of gas that can be produced from a given reservoir under these assumptions.

As it will be discussed, the analytical solution for a radial flow is a function of following main factors: the radius of the wellbore area and the imposed pressure at the wellbore; the pressure at the dissociation front (which depends on the reservoir temperature through the methane-hydrate phase boundary); the pressure at a distant boundary (equal to the reservoir initial pressure); the ratio between the permeability coefficients of the already dissociated hydrate sediments 'k_{Sed}' and that of the HBS 'k_{HBS}'; the length and the permeability coefficient of confining layers.

The corresponding radial flow problem was solved using the coupled THCM numerical code developed to analyze problems involving HBS. The finite element (FE) computer program takes into consideration thermal and hydraulic processes in deformable sediments, and it also accounts for the changes in sediment properties in the presence of hydrate dissociation. It is based on a fully coupled formulation that incorporates the different phases and species existing in HBS (including

hydrate and ice) and it has been implemented in CODE_BRIGHT (Olivella et al., 1996), an existing coupled multiphysics program for geological media.

To validate the FE program, the results of the analytical solution were compared against the outputs of a numerical model replicating the same conditions. The effects of critical factors were also analyzed. The comparisons between the outcome of the analytical solution and that of the finite element model were very satisfactory.

4.1. Cylindrical Flow Between Two Impermeable Layers at Steady State Conditions

At steady-state conditions, the pressure distribution in a radial flow through the reservoir confined by impermeable overburden and underburden layers is inversely proportional to the logarithm of the radial distance to the well. Therefore, there is a physical limit to the zone around a well that can experience pressure-driven dissociation. A simple yet robust set of equations to estimate limits for gas production from the HBS using depressurization has been proposed.

Considering radial flow conditions governed by Darcy's law in a thin and confined reservoir with impermeable layers, the following equations are derived:

$$v = k \frac{dh}{dr} \tag{81}$$

$$v = \frac{q}{2\pi r H} \tag{82}$$

where v [m/Sec] is the flow velocity at any specified point, k [m/Sec] is the hydraulic conductivity of medium, h [m] is the head of pressure at any specified point of the reservoir (since it is a thin reservoir, the variation of pressure head due to the elevation is negligible), r [m] is the radius of any specified point from the center of the wellbore area, q [m^3/Sec] defines the flow at any specific point and H [m] is the thickness of sediments. By combining these two equations and solving them in cylindrical coordinates, the flow equation could be written as:

$$\int_{r_1}^{r_2} \frac{q\,dr}{r} = -\int_{h_1}^{h_2} (2\pi H k)\,dh \tag{83}$$

The flow between two given points can be calculated as:

$$q = -\frac{2\pi H k (h_2 - h_1)}{\ln(\frac{r_2}{r_1})}$$

(84)

Two zones can be identified under steady state conditions when the pressure drop is kept constant and hydrates stop dissociating: the inner zone where hydrate has been depleted and the outer zone where hydrate remains stable (Figure.4.1). Let us define the size of the produced zone as r^* [m], and the head of pressure at a distant boundary as h_{far} [m]. The inner zone is characterized by the permeability of the sediment without hydrates 'k_{Sed}' and the outer zone by the permeability of the HBS 'k_{HBS}'. Clearly, gas was released from the inner zone '$r \leq r^*$'. Therefore, the following equations are valid at steady state conditions:

$$q_{Sed} = q_{HBS}$$

(85)

$$\frac{2\pi H k_{Sed}\left(h^* - h_w\right)}{\ln\left(\dfrac{r^*}{r_w}\right)} = \frac{2\pi H k_{HBS}\left(h_{far} - h^*\right)}{\ln\left(\dfrac{r_{far}}{r^*}\right)}$$

(86)

In the above equations, h^* [m] and h_w [m] are the head of pressure at the dissociation front and at the wellbore area respectively, and r_w [m] is the radius of well. Based on the aforementioned equation, at steady state conditions, the ultimate radius 'r^*' of the dissociated area is:

$$r^* = \left(r_w r_{far}^{\left(\frac{k_{Sed}}{k_{HBS}}\right)\left(\frac{h^* - h_w}{h_{far} - h^*}\right)} \right)^{\left(1 + \left(\frac{k_{Sed}}{k_{HBS}}\right)\left(\frac{h^* - h_w}{h_{far} - h^*}\right)\right)^{-1}}$$

(87)

It is worth mentioning that the length of reservoir 'r_{far}' is determined based on the ultimate radius of impermeable confining layers, since the sufficient flow into the reservoir keeps the head of pressure equal to the initial value at this point under the steady state condition.
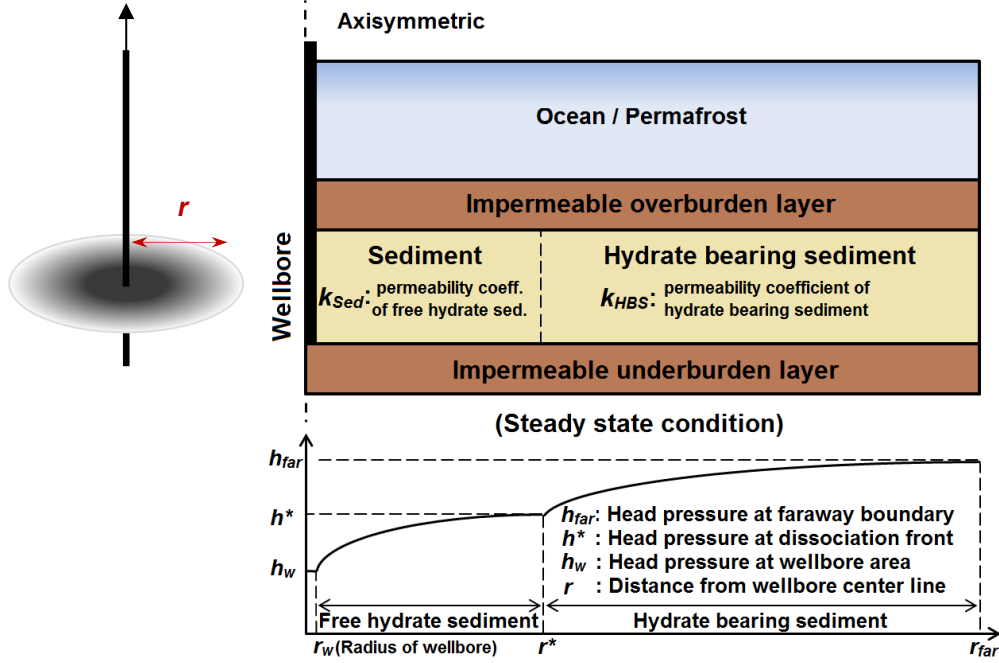
Figure 4.1 Two zones can be identified under steady state conditions when the pressure drop is kept constant and hydrate stops dissociating: an inner zone where hydrate has been depleted and an outer zone where hydrate remains stable.

As shown above, according to this simple yet robust analytical solution, the ultimate radius of pressure induced dissociation front in a thin and confined hydrate deposit is a function of 1) the radius of the wellbore area 'r_w' and the imposed pressure head at this radius 'h_w'; 2) the head of pressure at the dissociation front 'h^*' (which in turn depends on the reservoir temperature through the methane hydrate phase boundary); 3) the head of pressure at a distant boundary 'h_{far}' (equal to the reservoir initial pressure); and 4) the ratio between the hydraulic conductivity of the already dissociated hydrate sediments 'k_{Sed}' and that of the hydrate bearing sediments 'k_{HBS}' (Figure.4.1).

4.2. Steady State Cylindrical Flow Between Two Low Infinite Permeable Layers

Based on the law of refraction of streamlines (Bear, 1979) at boundary of two homogeneous layers with different permeability coefficients, the refraction of flow line is described as follows:

$$\frac{k_1}{\tan \delta_1} = \frac{k_2}{\tan \delta_2} \tag{88}$$

where k_1 and k_2 stand for the hydraulic conductivity of each layer while δ_1 and δ_2 are the angles, which streamlines in corresponding layers make with the normal vector of boundary surface. It follows that when $k_1 >> k_2$ then $\delta_1 >> \delta_2$ and the refracted streamline approaches the normal to the boundary surface on passing from one porous medium to another, less permeable than the first. Similarly, the refracted streamline tends to become almost parallel to the common boundary on passing from less to higher permeable layers. Therefore, if the reservoir is coffined between two very low permeable layers then horizontal flow lines in the reservoir and vertical flow lines in the low permeable confining layers can be assumed. Hence an approximate solution can be derived by following additional assumptions: 1) the flow in the less permeable layers ascend or descend vertically based on the direction of the hydraulic gradient within these layers; 2) the head of pressure above/below the less permeable overburden/underburden layer is constant; 3) reservoir and confining layers are homogeneous, therefore corresponding coefficients of permeability are constant within each layer; 4) the variation of pressure head due to the elevation is negligible by considering the thickness of layers; 5) and the length of very low permeable layer is theoretically infinite, which is explained in detail in Section 4.4., then at the steady state condition, flow in the reservoir is sustained almost entirely by the leakage. According to Eq. (81) and Eq. (82) the flow at any specific radius of reservoir *'r'* is derived as:

$$q_r = 2\pi r H k \frac{\partial h}{\partial r} \tag{89}$$

As illustrated in Fiqure.4.2 by considering the equilibrium at the steady state condition for a tiny section of reservoir, the following equations yield:

$$2\pi r H k \frac{\partial h}{\partial r} - 2\pi (r+dr) H k \frac{\partial h}{\partial r} - \pi \left[(r+dr)^2 - r^2 \right] k' \frac{h_0 - h_r}{H'} = 0 \tag{90}$$

$$k \frac{\partial h}{\partial r}\bigg|_r 2rH - k \frac{\partial h}{\partial r}\bigg|_{r+dr} 2(r+dr)H - 2rdrk' \frac{h_0 - h_r}{H'} = 0 \tag{91}$$

$$\frac{\frac{\partial h}{\partial r}\big|_r - \frac{\partial h}{\partial r}\big|_{r+dr}}{dr} rH - \frac{\partial h}{\partial r}\bigg|_{r+dr} H - k' \frac{h_0 - h_r}{H'.k} r = 0 \tag{92}$$

40

a) Plan View

b) Cross Section
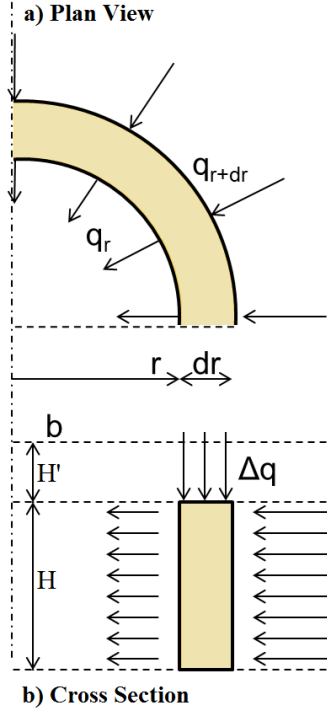
Figure 4.2 General description for a half depth of reservoir confined by less permeable layers. If $k' \ll k$ then horizontal streamlines within reservoir and vertical ascended/ descended flow lines into reservoir from less permeable confining layers can be assumed.

$$\frac{\partial^2 h}{\partial r^2} - \frac{1}{r}\frac{\partial h}{\partial r} - \frac{k'}{k}\frac{h_0 - h_r}{H.H'} = 0 \tag{93}$$

in which, as shown in Figure.4.3, H [m] and H' [m] are the half depth of the symmetric reservoir and the depth of each confining layer, k [m/Sec] and k' [m/Sec] stand for the hydraulic conductivity of the reservoir and confining layers respectively. As it is illustrated in Figure.4.4, if the reservoir is confined by both an impermeable layer from one side and a less permeable one from another side then H should be considered as the full depth of reservoir. h_0 [m] represents the initial reservoir head of pressure which is equal to h_{far} in the previous section. Modified Bessel Functions of order zero provides the general solution for Eq. (93) (De Glee 1951):

$$h_0 - h_r = \alpha_1 I_0(\frac{r}{\beta}) + \alpha_2 K_0(\frac{r}{\beta}) \tag{94}$$

in which I_0 and K_0 are the first and the second kind of Modified Bessel Function respectively and β stands for the leakage factor which is defined as:
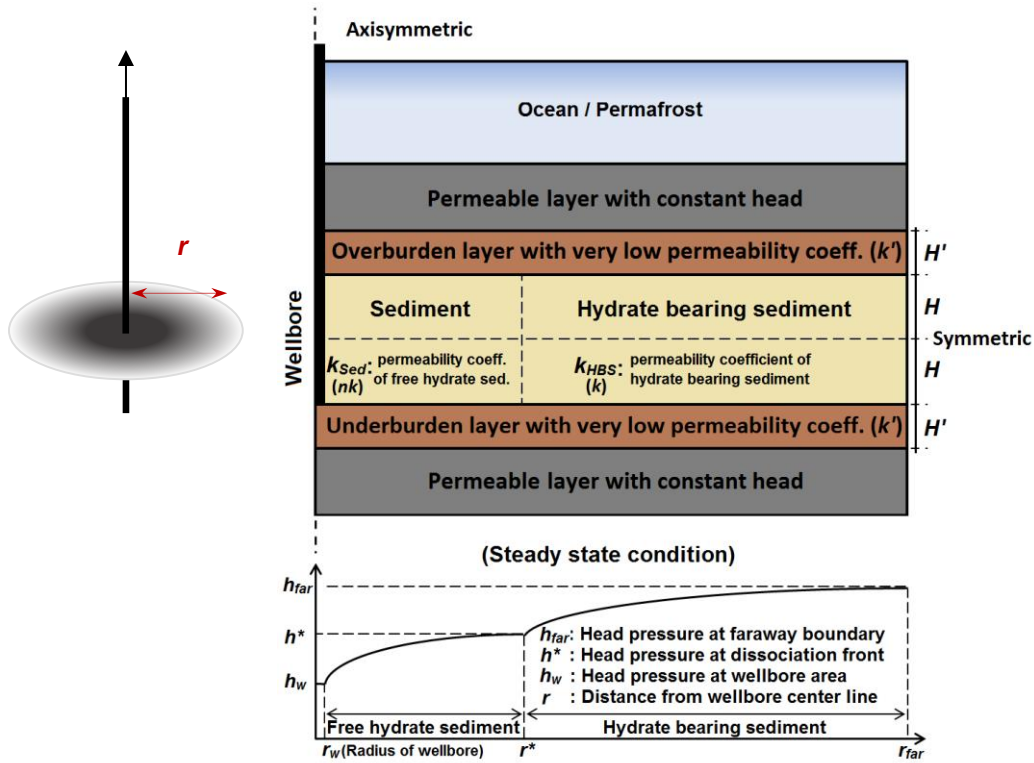
Figure 4.3 Axisymmetric HBS reservoir confined between less permeable layers. At steady state condition, reservoir is divided in two zones of free hydrate sediments and HBS by an interface radius know as dissociation front (r*).
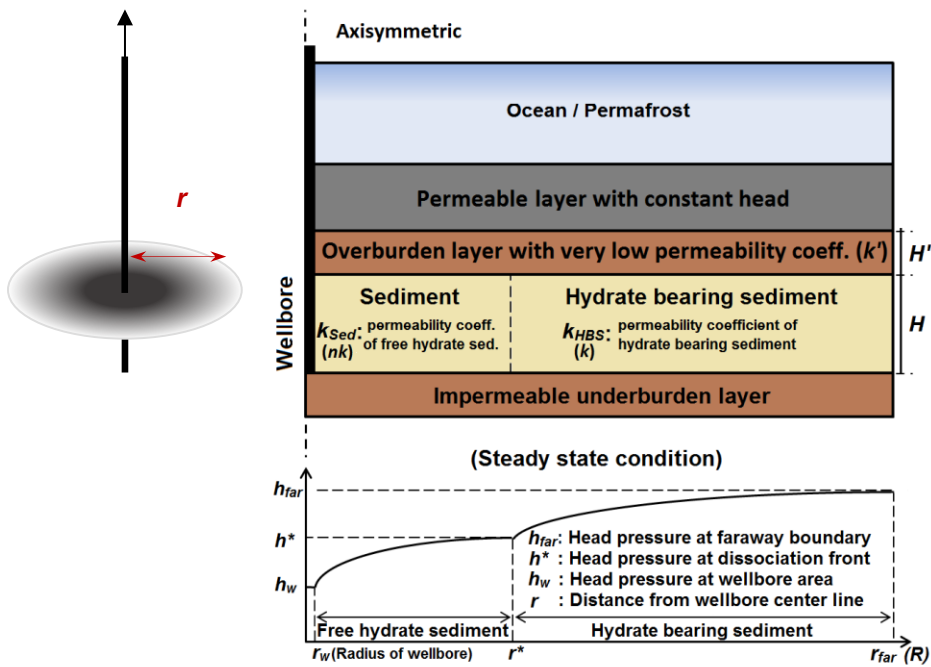
Figure 4.4 Axisymmetric HBS reservoir confined between impermeable layer from one side and less permeable layer from another side.

42

$$\beta = \sqrt{\frac{kHH'}{k'}} \tag{95}$$

Two boundary conditions can be considered: no drawdown at far distance and the constant discharge at the wellbore area. Since the second kind of Modified Bessel Function at infinity goes to zero $\left[K_0(\infty) = 0 \right]$ then:

$$(r = \infty) \rightarrow h_r = h_0 \rightarrow \alpha_1 I_0\left(\frac{r}{\beta}\right) + \alpha_2 K_0\left(\frac{r}{\beta}\right) = 0 \rightarrow \alpha_1 = 0 \tag{96}$$

The hydraulic gradient at each radius of the confined reservoir between two infinite low permeable layers can be derived by implementing α_1 from Eq. (96) into Eq. (94) then derivative of Eq. (94):

$$\frac{\partial h_r}{\partial r} = \frac{\partial\left(h_0 - \alpha_2 K_0\left(\frac{r}{\beta}\right) \right)}{\partial r} = \alpha_2 K_1\left(\frac{r}{\beta}\right)\frac{1}{\beta} \tag{97}$$

in which K_1 is the second kind of Modified Bessel Function of first order. By considering the constant discharge at the wellbore area, Eq. (89) and Eq. (97), α_2 is derived as:

$$q_w = 2\pi r_w H k \left.\frac{\partial h}{\partial r}\right|_{r=r_w} = 2\pi r_w H k \alpha_2 K_1\left(\frac{r_w}{\beta}\right)\frac{1}{\beta} \rightarrow \alpha_2 = \frac{q_w}{2\pi k H\left(\frac{r_w}{\beta}\right)K_1\left(\frac{r_w}{\beta}\right)} \tag{98}$$

Hence, based on Eq. (94), Eq. (96), and Eq. (98) the drawdown 'S_r' at any specified radius of a reservoir, which is confined by infinite low permeable layers is derived as follows:

$$S_r = h_0 - h_r = \frac{q_w}{2\pi H k}\frac{K_0\left(\frac{r}{\beta}\right)}{\left(\frac{r_w}{\beta}\right)K_1\left(\frac{r_w}{\beta}\right)} \tag{99}$$

in which q_w is calculated by knowing the drawdown at the wellbore area:

$$q_w = \frac{2\pi H k \left[h_0 - h_w \right] \left(\dfrac{r_w}{\beta} \right) K_1 \left(\dfrac{r_w}{\beta} \right)}{K_0 \left(\dfrac{r_w}{\beta} \right)} \tag{100}$$

At steady state conditions, when the pressure drop is kept constant and hydrates stop dissociating, from the wellbore area up to the dissociation front '$r*$' hydrates have been depleted and also remain stable beyond that radius. The inner zone is characterized by the permeability of the sediment without hydrates 'k_{Sed}' and the outer zone by the permeability of the hydrate bearing sediment 'k_{HBS}'. Consequently, the reservoir cannot be assumed as a homogeneous porous medium anymore, therefore the aforementioned equation should be modified. The concept of the equivalent section is implemented in this regard; if n is the ratio of the hydraulic conductivity of free hydrate sediments over that of HBS, then the section of reservoir containing free hydrate sediments with the length of $r*$ can be represented by the n times longer equivalent section having the same permeability coefficient of HBS. But since this modification does not deal with the leakage through confining layers, the new leakage factor β' should be used for this section by considering the hydraulic conductivity of free hydrate sediments with respect to that of confining layers. As a result, if $h*$[m] is the head of pressure at the dissociation front '$r*$' based on the corresponding temperature on the hydrate phase stability boundary diagram then $S*$ is the drawdown at this radius. Therefore at steady state conditions, the ultimate radius of the dissociated area '$r*$' is calculated as:

$$n = \frac{k_{Sed}}{k_{HBS}} \rightarrow r* = n.r_{eq} \tag{101}$$

$$\beta = \sqrt{\frac{k_{HBS} H H'}{k'}}, \beta' = \sqrt{\frac{k_{Sed} H H'}{k'}} \tag{102}$$

$$S* = h_0 - h* = \frac{q_w}{2\pi H k_{HBS}} \frac{K_0 \left(\dfrac{r_{eq}}{\beta'} \right)}{\left(\dfrac{r_w}{\beta} \right) K_1 \left(\dfrac{r_w}{\beta} \right)} = \frac{q_w}{2\pi H k_{HBS}} \frac{K_0 \left(\dfrac{r*}{n.\beta'} \right)}{\left(\dfrac{r_w}{\beta} \right) K_1 \left(\dfrac{r_w}{\beta} \right)} \tag{103}$$

44

$$r* = K_0^{-1} \left[\frac{S * 2\pi H k_{HBS} \left(\frac{r_w}{\beta} \right) K_1 \left(\frac{r_w}{\beta} \right)}{q_w} \right] \times (n.\beta') \tag{104}$$

As shown in Eq. (100) and Eq. (104), the ultimate radius of the pressure induced dissociation front in a thin hydrate deposit confined by infinite low permeable layers is a function of 1) the radius of the wellbore area 'r_w' and the imposed head of pressure at this radius 'h_w'; 2) the head of pressure at the dissociation front '$h*$' (which in turn depends on the reservoir temperature through the methane hydrate phase boundary); 3) the initial reservoir head of pressure 'h_0'; 4) the ratio between the hydraulic conductivity of the already dissociated hydrate sediment 'k_{Sed}' and that of the hydrate bearing sediments 'k_{HBS}'; 5) the leakage factor, which depends on the square root of ratio between the permeability coefficient of reservoir sediments and that of confining layers as well as a function of their corresponding thicknesses.

4.3. Steady State Cylindrical Flow Between Two Low Finite Permeable Layers

If the reservoir is confined by low permeable layers extended to the radius of '$r=R$' and at the end of those layers, there are permeable confining layers providing a sufficient flow into the reservoir to keep the pressure equal to the initial one, then new boundary conditions should be applied to Eq. (94) at '$r=R$':

$$r = R \rightarrow h_R = h_0 \rightarrow \alpha_1 I_0 \left(\frac{R}{\beta} \right) + \alpha_2 K_0 \left(\frac{R}{\beta} \right) = 0 \rightarrow \frac{\alpha_1}{\alpha_2} = -\frac{K_0 \left(\frac{R}{\beta} \right)}{I_0 \left(\frac{R}{\beta} \right)} \tag{105}$$

By assuming small radius of the wellbore with respect to the leakage factor that results in $\left[\left(\frac{r_w}{\beta} \right) K_1 \left(\frac{r_w}{\beta} \right) = 1 \right]$, and considering the constant discharge at the wellbore area, Eq. (94) and Eq. (105), the drawdown at any radius of the reservoir confined by finite low permeable layers is calculated as:

$$S_r = h_0 - h_r = \frac{q_w}{2\pi Hk}\left[K_0\left(\frac{r}{\beta}\right) - I_0\left(\frac{r}{\beta}\right)\frac{K_0\left(\frac{R}{\beta}\right)}{I_0\left(\frac{R}{\beta}\right)}\right] \qquad (106)$$

If the ultimate radius of both the reservoir and confining low permeable layers is limited to the radius of *'r=R'* at which there is an impermeable rock that makes it impossible to have any horizontal flow beyond that radius into either the reservoir or confining layers, then the hydraulic gradient at this point should be equal to zero. Hence, by considering Eq. (94) the boundary condition at *'r=R'* is modified as follows:

$$\left.\frac{\partial h_r}{\partial r}\right|_{r=R} = 0 \rightarrow \left.\frac{\partial\left(h_0 - \alpha_1 I_0\left(\frac{r}{\beta}\right) - \alpha_2 K_0\left(\frac{r}{\beta}\right)\right)}{\partial r}\right|_{r=R} = 0 \rightarrow -\alpha_1\left(\frac{1}{\beta}\right)I_1\left(\frac{R}{\beta}\right) + \alpha_2\left(\frac{1}{\beta}\right)K_1\left(\frac{R}{\beta}\right) = 0 \rightarrow \frac{\alpha_1}{\alpha_2} = \frac{K_1\left(\frac{R}{\beta}\right)}{I_1\left(\frac{R}{\beta}\right)} \qquad (107)$$

Assuming a small radius of the wellbore with respect to the leakage factor, the constant discharge, the aforementioned boundary condition at *'r=R'*, and Eq. (94), the following equation yields the drawdown at any specified radius for this particular problem:

$$S_r = h_0 - h_r = \frac{q_w}{2\pi Hk}\left[K_0\left(\frac{r}{\beta}\right) + I_0\left(\frac{r}{\beta}\right)\frac{K_1\left(\frac{R}{\beta}\right)}{I_1\left(\frac{R}{\beta}\right)}\right] \qquad (108)$$

Similar to the confining reservoir by infinite low permeable layers, under steady state conditions, the reservoir is divided in two zones of free hydrate sediments and HBS. By modifying the model based on the aforementioned concept of the equivalent section, the radius *'r*'* within that dissociation takes place for the cases of a permeable medium's presence beyond *'r=R'* and also an existence of an impermeable rock at this radius, can be derived by solving Eq. (106) and Eq. (108) respectively:

$$if\left(r=R\rightarrow h_R=h_0\right):$$

$$S^*=h_0-h^*=\frac{q_w}{2\pi Hk_{HBS}}\left[K_0\left(\frac{r_{eq}}{\beta'}\right)-I_0\left(\frac{r_{eq}}{\beta'}\right)\frac{K_0\left(\frac{(R-r^*)}{\beta}+\frac{r_{eq}}{\beta'}\right)}{I_0\left(\frac{(R-r^*)}{\beta}+\frac{r_{eq}}{\beta'}\right)}\right]=\frac{q_w}{2\pi Hk_{HBS}}\left[K_0\left(\frac{r^*}{n.\beta'}\right)-I_0\left(\frac{r^*}{n.\beta'}\right)\frac{K_0\left(R+r^*\left(\frac{1}{n^{3/2}}-1\right)\bigg/\beta\right)}{I_0\left(R+r^*\left(\frac{1}{n^{3/2}}-1\right)\bigg/\beta\right)}\right]\quad(109)$$

$$K_0\left(\frac{r^*}{n.\beta'}\right)-I_0\left(\frac{r^*}{n.\beta'}\right)\left[\frac{K_0\left(R+r^*\left(\frac{1}{n^{3/2}}-1\right)\bigg/\beta\right)}{I_0\left(R+r^*\left(\frac{1}{n^{3/2}}-1\right)\bigg/\beta\right)}\right]=\frac{S^*2\pi Hk_{HBS}}{q_w}\quad(110)$$

$$if\left(r=R\rightarrow\frac{\partial h_r}{\partial r}\bigg|_{r=R}=0\right):$$

$$S^*=h_0-h^*=\frac{q_w}{2\pi Hk_{HBS}}\left[K_0\left(\frac{r_{eq}}{\beta'}\right)+I_0\left(\frac{r_{eq}}{\beta'}\right)\frac{K_1\left(\frac{(R-r^*)}{\beta}+\frac{r_{eq}}{\beta'}\right)}{I_1\left(\frac{(R-r^*)}{\beta}+\frac{r_{eq}}{\beta'}\right)}\right]=\frac{q_w}{2\pi Hk_{HBS}}\left[K_0\left(\frac{r^*}{n.\beta'}\right)+I_0\left(\frac{r^*}{n.\beta'}\right)\frac{K_1\left(R+r^*\left(\frac{1}{n^{3/2}}-1\right)\bigg/\beta\right)}{I_1\left(R+r^*\left(\frac{1}{n^{3/2}}-1\right)\bigg/\beta\right)}\right]\quad(111)$$

$$K_0\left(\frac{r^*}{n.\beta'}\right)+I_0\left(\frac{r^*}{n.\beta'}\right)\left[\frac{K_1\left(R+r^*\left(\frac{1}{n^{3/2}}-1\right)\bigg/\beta\right)}{I_1\left(R+r^*\left(\frac{1}{n^{3/2}}-1\right)\bigg/\beta\right)}\right]=\frac{S^*2\pi Hk_{HBS}}{q_w}\quad(112)$$

According to Eq. (110) and Eq. (112), the ultimate radius of the pressure induced dissociation front in a thin hydrate deposit confined by finite low permeable layers not only depends on the five aforementioned factors for the reservoir confined by infinite less permeable layers but also is a function of the ultimate radius of confining layers *'R'*, as well as if the reservoir is vertically confined by an impermeable boundary at this ultimate radius.

4.4.Criteria for Considering Finite or Infinite Length of Confining Layers

At any specified radius $'r'$, some portion of the well discharge $'q_w'$ flows through reservoir $'q_r'$ while the remaining part $'q_w - q_r'$ enters the aquifer through the leakage from low permeable confining layers. The ratio of q_r/q_w is obtained as follows (Bear, 1979):

$$\frac{q_r}{q_w} = \left(\frac{r}{\beta}\right) K_1\left(\frac{r}{\beta}\right) \tag{113}$$

With an accepted error, as shown in Figure.4.5, at $r = 6\beta$ all the well discharge flows through the leakage from less permeable confining layers. Therefore, for the sake of simplicity, if the radius of less permeable confining layer is six times higher than the leakage factor then those confining layers can approximately be assumed as the infinite value. Otherwise the boundary condition related to finite confining layers should be implemented.

Moreover, this concept may help to obtain more realistic and accurate results from numerical models by having a good understanding of reservoir boundary conditions and the radius of depressurization influenced zone with respect to adjacent layers of HBS deposit.
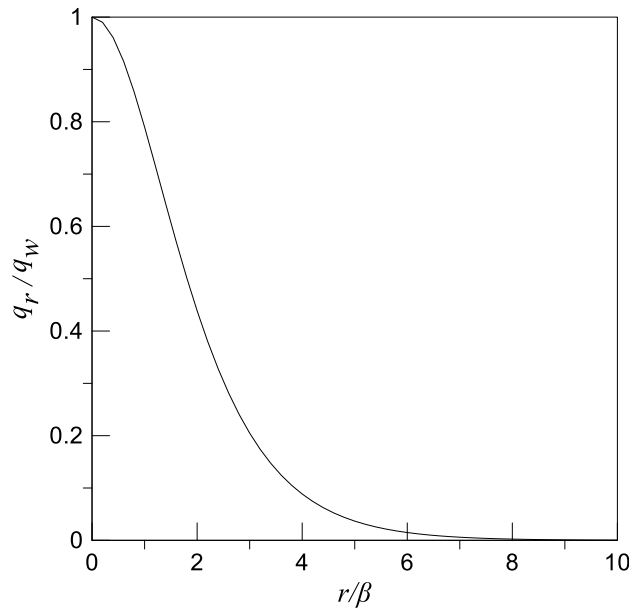
Figure 4.5 Approximately at $r = 6\beta$ all the well discharge flowing through leakage from less permeable confining layers.

48

4.5.Simulation and Discussion

To validate the developed FE program, the results of the analytical solution discussed above ware compared against the outputs of a numerical model replicating the same conditions. The effects of critical factors are also analyzed.

Several models were prepared based on various reservoir initial and boundary conditions and also different production strategies by imposing a variety of possible pressures at the wellbore to verify the code performance when compared against the results from the analytical solution. These analyses also allowed studying the effect of crucial parameters and factors related to the problem of hydrate dissociation induced by depressurization. Table.4.1 presents the initial reservoir conditions and also the imposed pressure at the wellbore for the cases studied for this purpose.

The intrinsic permeability coefficient for hydrate bearing sediments k_{HBS}=1x10^{-12} m^2 was considered in all the models. An initial hydrate saturation S_h=0.5 was adopted. The different ratios between already dissociated hydrate sediment permeability coefficient 'k_{Sed}' and k_{HBS} were obtained by adopting different values of the hydrate morphology coefficients N according to Eq. (29). Also details about the porosity, the capillary pressure model, and the liquid/gas relative permeability models are shown in Table.4.2.

Table 4-1 Cases considered in the analysis

Case	h_{far} (m)	h_w (m)	T (°C)	$\dfrac{h^* - h_w}{h_{far} - h^*}$
A	1020	306	12	7.14
B	1224	306	12	2.14
C	1224	510	12	1.44
D	1224	306	10	0.91
E	1224	306	8	0.47

Table 4-2 Model parameters used in numerical simulation

Parameter	Value
Initial saturation	S_h=0.50, S_l=0.50, S_g=0.00
Intrinsic permeability in HBS	k_{HBS}=1x10-12 m2 (Isotropic: $k_x = k_y = k_z$)
Porosity of HBS	φ=0.40
Porosity of less permeable confining layers	φ=0.40
Capillary pressure model	Po=100 kPa; λ=0.5
Liquid relative permeability model	$a = 3$
Gas relative permeability model	$b = 3$

Figure.4.6 presents the results from the analytical solution discussed above (lines) for the different cases listed in Table.4.1, showing the interplay between the relative sediment permeability coefficients k_{Sed}/k_{HBS} and the relative pressure dissociation. For example, it is predicted that the dissociation front is the farthest (from the well) when the permeability contrast between already dissociated and hydrate sediments is the highest. This implies that the permeability enhancement during dissociation plays an essential role in the depressurization propagation in hydrate reservoirs. For a fixed k_{Sed}/k_{HBS}, Cases B, D and E allow assessing the effect of the reservoir initial temperature (i.e. all the other factors are identical) showing that the larger amount of gas is released from warmer reservoirs. Cases A and C have the same hydraulic gradient, as well as, the same initial temperature, but different initial pressures. Under these conditions the lower the initial reservoir pressure, the higher the amount of gas produced. Similar meaningful discussions can be conducted involving other variables and factors, showing the usefulness of this type of solution.

The proposed analytical solution is also very useful to validate the numerical program. A 2-D axisymmetric model including a single vertical producing well that replicates the conditions of the analytical solution was developed. A thin and long (L=1200 m) reservoir confined by impermeable layers was adopted. The mesh discretization along the radial direction was not uniform, increasing logarithmically from 0.12m at rw to 0.80 m at rmax. The final discretization consists of a 2503 elements. We conducted a mesh sensitivity analysis to confirm that the adopted domain discretization was appropriate.
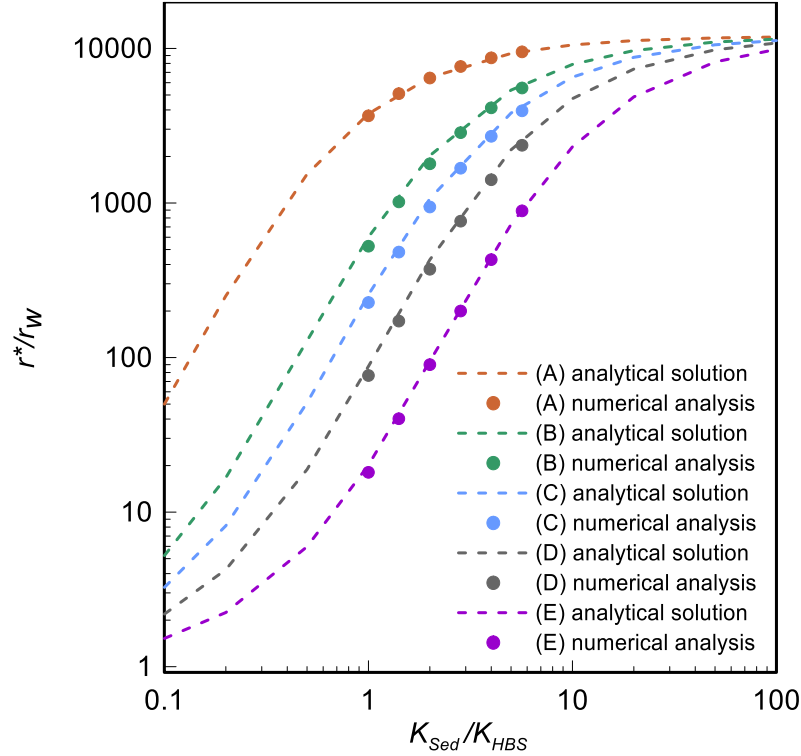
Figure 4.6 Results obtained with the analytical solution and numerical models related to reservoir with impermeable confining layers for the different cases listed in Table 1.

Each FE steady state simulation corresponds to a point in Figure.4.6, we conducted a total of 30 analyses (indicated by symbols). To reach the steady state condition we considered a long-term depressurization in the simulations. Therefore, the cases were run until practically no changes in the variables were observed. A very satisfactory agreement between numerical and analytical results was obtained, indicating that the proposed approach is able to capture the main features of HBS behavior associated with this particular conditions and could be extended to other conditions.

For the sake of modeling a reservoir confined by infinite less permeable layers, a long reservoir (L=4km) with thickness of ten meters (H=5m) confined by two meters thickness of each overburden and underburden (H'=2m) was adopted. The mesh discretization was increasing logarithmically from 0.183m adjacent to r_w to 15.98m at r_{max} through the radial direction while there was a uniform discretization along vertical direction. The final discretization consists of 7831 nodes and 7216 elements.

To reach the steady state condition, a long term depressurization was considered in the numerical analyses. In some occasions, the steady state condition was not fully achieved (even for the very long time duration performed analyses). In these cases, the final conditions were not very far from the steady state ones. In fact, for some of the cases analyzed, the analytical solution predicted a little bit further dissociation front than the FE solution. Therefore, it appears that if those models would run for longer times, both results could match even better. In all the cases, the radii of the wellbore area was r_w=0.1m. It is also assumed that the rate of heat conductivity is high enough to compensate the temperature reduction due to the endothermic behavior of hydrate dissociation by reaching the steady state condition. Therefore the head of pressure at dissociation front 'h^*' is derived from the methane hydrate phase boundary diagram for a given reservoir initial temperature.

Figure.4.7 presents the results of the analytical solution for the reservoir confined by infinite less permeable layers corresponding to the different cases listed in Table 1, showing the interplay between the leakage factor 'β' and the relative pressure dissociation '$(h^* - h_w)/(h_{far} - h^*)$'.

Also, Figure.4.8 shows the drawdown through the reservoir confined by infinite less permeable layers and having the same properties of *Case B* with two different leakage factors. As illustrated, the result of the numerical analysis perfectly matches with the prediction of the analytical solution.

Generally, the most efficient depressurization is related to a perfectly confined reservoir, but for the reservoir which is confined by low permeable layers, favorable condition is the existence of a vertical impermeable rock around the ultimate radius affected by depressurization derived as a function of the leakage factor. Also depressurization has the lowest efficiency in the reservoir confined by finite low permeable layers with the length shorter than affected radius of depressurization and connected to high permeable porous medium beyond that point.

The suggested analytical solution can predict the ultimate radius of the depressurization induced dissociation front in HBS at the steady state equilibrium based on reservoir initial conditions, hydrate morphology and its pertinent effect on sediment properties, induced pressure at the vertical well, and the most important of all, the boundary conditions, geometries and properties of reservoir confining layers.
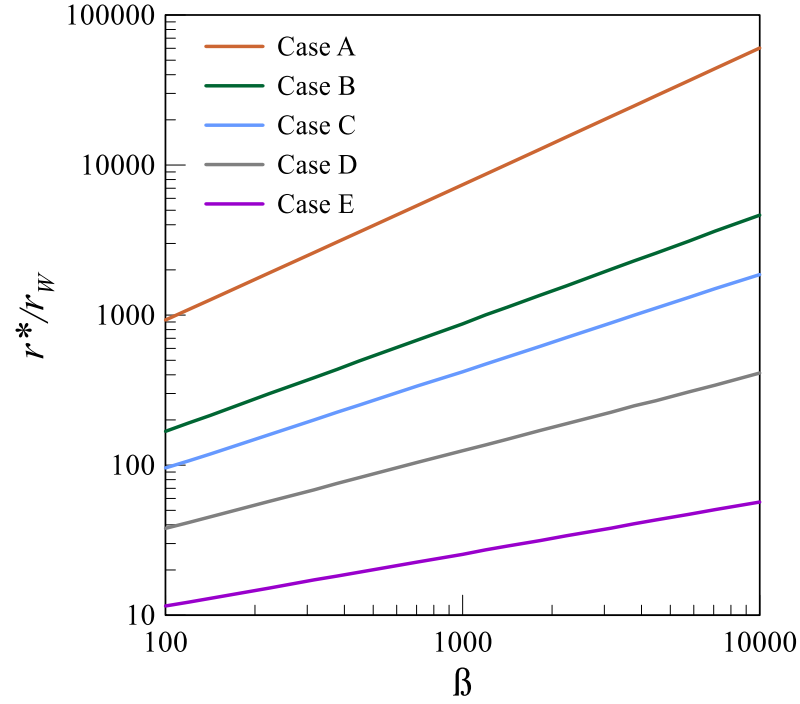
Figure 4.7 Results obtained with the analytical solution related to the reservoir confined by infinite less permeable layers for the different cases listed in Table 1. Numerical results are very satisfactory when compared against that of the analytical solution.
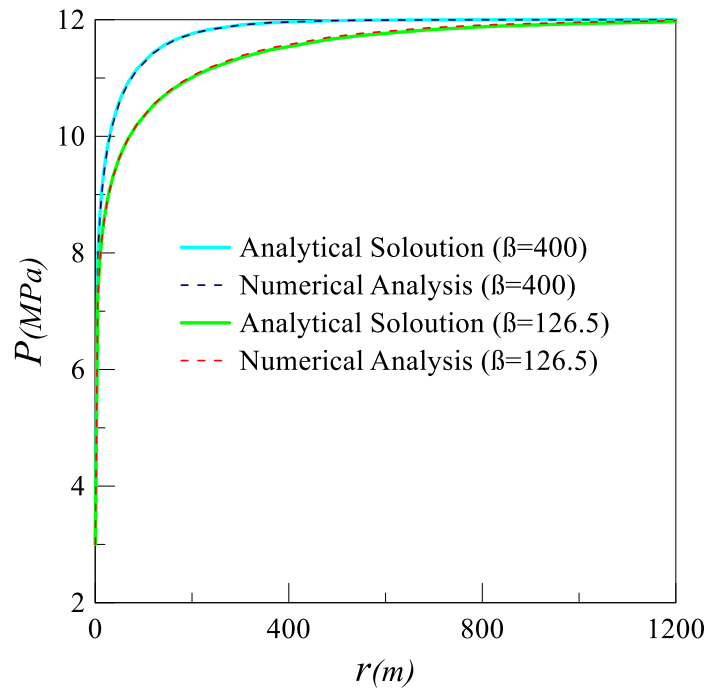
Figure 4.8 Profile of pore pressure through reservoir at steady state condition. Obviously, the result of numerical analysis is compatible with the prediction of analytical solution.

53

In addition, defining realistic boundary conditions is the most essential requirement to get reasonable results from numerical modeling. By having proper simple data from reservoir horizontal and vertical confining layers, the suggested analytical solution can help to define realistic boundaries and also determine the influence zone of depressurization.

As discussed, the analytical solution also depends on crucial factors which affect hydrate dissociation like the dependency of sediments properties on the hydrate morphology, the induced pressure at the wellbore, the initial pressure, and the temperature of HBS deposit. The comparative study was done about the effect of those parameters and the results of both analytical solution and numerical models are compatible.

5. SAND PRODUCTION:

A SIDE EFFECT OF PRODUCING GAS FROM HBS

5.1.State of the Art

Sand production usually takes place in an unconsolidated sandstone (UCSS) reservoir as a side effect of oil and gas production. Sediment degradation and disaggregation of the material around the cavity, together with (relatively high) seepage forces (generated by well operation) remove the disaggregated particles leading to sand production. This complex phenomenon depends on various factors, such as the stress level, stress history, stress distribution (especially around the wellbore), seepage forces, as well as sediment and fluids properties. This process is generally associated with two main mechanisms; sediment plastification and localized failure of the solid phase (i.e. mechanical instability), as well as erosion induced by the fluid drag forces, resulting in the dislodgment and migration of loose particles (i.e. hydro-mechanical instability). Moreover, these mechanisms are strongly coupled and inter related. Particle disaggregation weakens the sediment, decreasing its strength, inducing also stress concentration that leads to local failure and the releasing of more particles. Furthermore, seepage velocity also increases with the porosity enhancement induced by this process, increasing in turns the ability of the fluid to drag bigger particles. These are processes which feed back into each other, exacerbating the problem.

Since this phenomenon could lead to various problems such as early well completion, numerous studies have been conducted in order to anticipate its occurrence and extremeness. Based on these studies, proper techniques can be implemented in order to control sanding. Sand screens, liners and gravel packs are typically used to limit sand production. Detailed sanding analysis are generally required to provide the best well design and also to estimate amount of sand to be produced.

Issues associated with sand production have also been observed in field tests of methane production from HBS. For example, sanding was observed during ConocoPhillips gas production test from gas hydrate sediments on North Slope of Alaska. Although, sanding was anticipated (i.e.

Delta Elite 200 micron screens were implemented before the start of the test) the magnitude of sand production was unexpected (i.e. more than 67bbl of sand with a mean particle size of 148μm were produced along with gas and water). Some valves were damaged and the tanks and separator contained considerable amount of sand at the end of the field trial test. Moreover, during the 1st offshore gas hydrate field trial production at Nankai Trough (Japan) in 2013, the operation was terminated on day 6 due to severe sanding, although the perforation was equipped with gravel pack. More than 30 m^3 of sand was produced during this short-term field test.

Sand production is a relatively well-known problem that has been extensively studied in the context of hydrocarbon production from conventional reservoirs. However, this problem associated with methane production from HBS possess new and significant challenges that require further research. A significant difference is that hydrate dissociation induces profound changes in the sediment structure, facilitating even more disaggregation of particles and their subsequent transport. In the following, a review of current methods to study sand production are briefly introduced.

The first methods for anticipating sand production were derived from empirical relationships in terms of fluid velocity, formation strength and grains size. Ishunwa et al. (2010) proposed a simple analytical model for predicting sand production in the Niger delta oil filed. The equation was on stablishing the equilibrium between buoyancy and drag forces associated with fluids flow in reservoir. This approach is similar to one proposed before by Bratli-Risnes, which shows the effect of flow rate, fluid viscosity, grain size, grain density and cavity height on sand production. Fjaer et al. (2004) proposed a simple analytical model based on both mechanical behavior and erosion equations. This simple model depends on the amount of reducing well pressure blew the critical sand production pressure, fluid flow rate, fluid viscosity, and rock cementation. They assumed that the removal of sand from the rock is an erosion process driven by the fluid flow, in such a way that the rate of produced sand is proportional to the hydrodynamic forces acting on the grains. Also there is a minimum force which is required to uphold the erosion process. Wang et l. (2011) proposed a model based on the momentum and mass balance equations that simulates the sand removal process by equipping it with Eulerian boundary and automatic adaptive re-meshing. This model is especially useful for studying the complex behavior of wormhole production during cold heavy oil production with sand. According to Papamichos & Vardoulakis (2005) porosity diffusion model illustrates erosion in mono-disperse media as opposed to filtration of fines in a

coarse matrix. A simple model for fluidized particles discharge is a gradient law that enforces particles to exit from regions of increasing porosity. This may be seen as a piping erosion law which enforces the flow line of eroded particles to follow the porosity gradient. Papamichos (2004) suggested that the rate of fluidized particles mass per unit volume is related to the magnitude of the pore pressure gradient.

Uchida et al. (2016) also studied on sand production model in gas hydrate sediments by implementing thermo-hydro-mechanical coupling and enhanced the numerical code which they prepared for simulating methane hydrate gas production. They assumed that eroded particles are divided into two groups of fluidized and settled particles based on considering two threshold values for hydraulic gradient which are functions of hydrate saturation. In fact by satisfying the upper value, eroded soil particles are transported by fluid phase. In this model, increasing hydraulic gradient does not have any effect on the severity of sanding, which is not realistic. Also, there are several factors implemented in this model that should be determined by experimental tests.

According to previous studies, continuous modeling by considering both mechanical behavior of material and erosion equations is the most accurate way to predict and evaluate the sand production (Rahmati et al. 2013).

5.2.Methodology

The framework of the numerical code explained in *Chapter.3* is capable to be enhanced for considering the soil erosion during the methane hydrate gas production.

As an adjustment, it is assumed that the liquid phase is composed by two species of eroded minerals and water (Figure.5.1). Accordingly, the density of liquid phase can be written as:

$$\rho_l = (1-c)\rho_w + c\rho_s \tag{114}$$

in which ρ_w and ρ_s are the densities of water and mineral species respectively and c stands for the volumetric concentration of fluidized minerals due to erosion in the liquid phase.

Therefore, the modified mass balance equation for the water species can be expressed as:

$$\frac{\partial}{\partial t}\Big[\big(\rho_w(1-c)S_l + \alpha\rho_h S_h + \rho_i S_i\big)\varphi\Big] + \nabla\cdot\Big[(1-c)\rho_w q_l + (1-c)\rho_w S_l\varphi\dot{u} + \alpha\rho_h S_h\varphi\dot{u} + \rho_i S_i\varphi\dot{u}\Big] = f^w \tag{115}$$

where $\rho_w \left[\frac{M}{L^3} \right] \left(\frac{Kg}{m^3} \right)$, ρ_h, and ρ_i represent the mass density of water specie, hydrate phase, and ice phase respectively. S_β ($\beta=l,h,i$) indicates the phase saturation, α is the mass fraction of water in hydrate, c is the volumetric concentration of fluidized particle in liquid phase (due to erosion), and $f^w \left[\frac{M}{L^3 t} \right] \left(\frac{Kg}{m^3 \, Sec} \right)$ stands for the external water mass supply per unit volume of the medium.
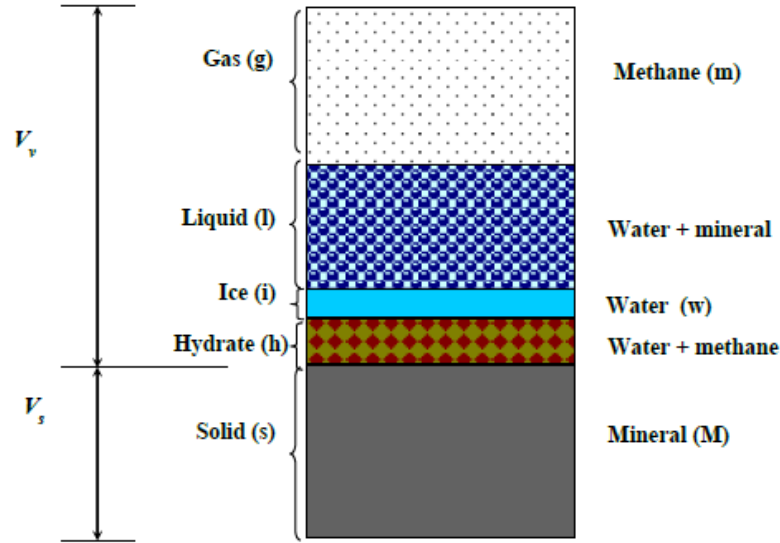
Figure 5.1 Components of HBS grouped into phases and species (considering soil erosion).

Moreover, the mass balance equation of the mineral species, which is found in the solid and liquid phases, should be adjusted as follows:

$$\frac{\partial}{\partial t} \left[\rho_s \left((1-\varphi) + cS_l \varphi \right) \right] + \nabla \cdot \left[c\rho_s q_l + \rho_s cS_l \varphi \dot{u} + \rho_s (1-\varphi) \dot{u} \right] = 0$$

(116)

where $\rho_s \left[\frac{M}{L^3} \right] \left(\frac{Kg}{m^3} \right)$ is the mass density of the minerals that make the soil particles.

As mentioned previously, sand production is initiated by the fluid seepage force when failure occurs based on the soil mechanical behavior. The pore pressure gradient model, introduced by Papamichos (2004), is implemented in this framework. According to this model, the rate of

fluidized particles mass per unit volume of the porous medium is a function of the plastic shear strain and also the pore pressure gradient.

$$\frac{\partial m_s}{\partial t} = \rho_s \lambda \nabla P \tag{117}$$

where $\frac{\partial m_s}{\partial t} \left(\frac{Kg}{m^3 \, \text{Sec}} \right)$ is the rate of sand erosion per unit volume of the medium, ρ_s is the density of minerals, ∇P is the pore pressure gradient, and $\lambda \left[\frac{L^2 t}{M} \right] \left(\frac{m^2 \, \text{Sec}}{Kg} \right)$ is the sand production coefficient, which is determined as a function of plastic shear strain by an experiment (Figure5.2).

$$\lambda \left[\frac{L^2 t}{M} \right] = \begin{cases} 0 \rightarrow \varepsilon_q^p \leq \varepsilon_q^{p^*} \\ \lambda_1 \left(\varepsilon_q^p - \varepsilon_q^{p^*} \right) \rightarrow \varepsilon_q^{p^*} \leq \varepsilon_q^p \leq \varepsilon_q^{p^*} + \lambda_2/\lambda_1 \\ \lambda_2 \rightarrow \varepsilon_q^{p^*} + \lambda_2/\lambda_1 \leq \varepsilon_q^p \end{cases} \tag{118}$$

in which ε_q^p stands for the plastic shear strain, $\varepsilon_q^{p^*}$ is the threshold value at which sand erosion is initiated, λ_1 is the increment rate of sand production coefficient untill it reaches the maximum value of λ_2. Although the value of sand production coefficient is determined by an experiment, but it would be a function of soil mechanical behavior and also inherent fluid properties like the viscosity and the density.

This numerical code is already equipped with Hierarchical Single Surface model (HISS) which is an accurate mechanical modeling with respect to the inherent behavior of HBS. In fact, the effects of hydrate saturation and morphology are considered in the mechanical modeling. Therefore, the plastic shear strain is calculated by considering those effects and consequently, soil erosion is implicitly affected by hydrate saturation and morphology. In the other words, this model is taking into account both the accurate mechanical behavior of HBS and also the erosion due to flow according to the fluid properties.

By considering the aforementioned rate of sand erosion, the mass balance equation of intact soil particles in solid phase is written as:

$$\frac{\partial}{\partial t} \left(\rho_s \left(1 - \varphi \right) \right) + \nabla . \left[\rho_s \left(1 - \varphi \right) \dot{u} \right] = -\rho_s \lambda \nabla P \tag{119}$$

where φ represents the porosity and $\overset{\bullet}{u}\left(\frac{m}{Sec}\right)$ is the velocity of porous medium motion relative to the fixed reference system. By implementing the definitions of material derivative with respect to the solid velocity, the variation in porosity is derived as:

$$\frac{D\varphi}{Dt} = \frac{(1-\varphi)}{\rho_s}\frac{D\rho_s}{Dt} + (1-\varphi)\nabla.\overset{\bullet}{u} + \lambda\nabla P \tag{120}$$

Apparently, as indicted in the above equation, the porosity of porous medium increases with sand production. Consequently, there is an expansion in the volume of void while the volumes of all phases remain constant except that of liquid phase. Therefore after considering the hydrate/ice formation/dissociation at any time step, the phase saturation should be modified based on the mass balance equation for the corresponding phase.
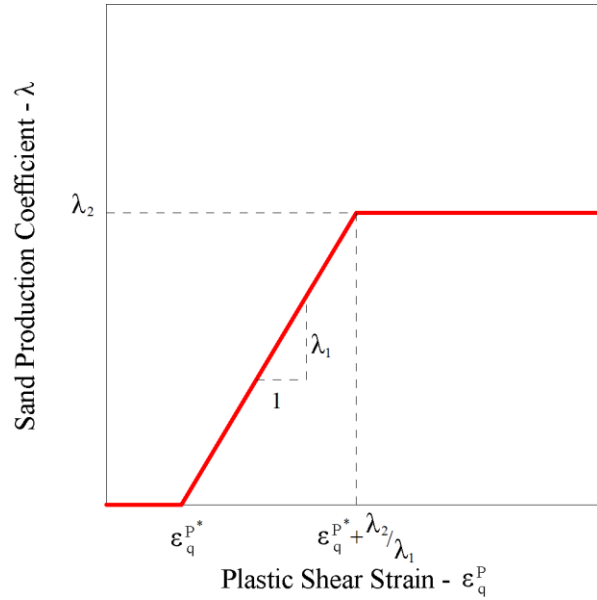
Figure 5.2 Sand production coefficient is a function of plastic shear strain determined by an experimental observation. Both porous medium mechanical behavior and the properties of fluid flow affect this parameter.

Accordingly, the updated ice saturation is derived by considering the mass balance equation for the ice phase as shown in Eq. (123) in which $\left(\frac{f^i}{\varphi\rho_i}\right)$ represents for the variation of the ice

saturation due to the ice formation/melting calculated based on the pseudo kinetic model explained in *Chapter.3*.

$$\frac{\partial}{\partial t}\left[\rho_i S_i \varphi\right] + \nabla.\left[\rho_i S_i \varphi \dot{u}\right] = f^i \tag{121}$$

$$\frac{DS_i}{Dt} = \left(\frac{f^i}{\varphi \rho_i}\right) - S_i\left(\frac{1}{\varphi}\frac{D\varphi}{Dt} + \frac{1}{\rho_i}\frac{D\rho_i}{Dt} + \nabla.\dot{u}\right) \tag{122}$$

$$S_i^{i+1} - S_i^i = \frac{f^i}{\varphi \rho_i} \tag{123}$$

With a same trend, the updated hydrate saturation is calculated according to the mass balance equation for the hydrate phase as shown in Eq. (126) in which $\left(\frac{f^h}{\varphi \rho_h}\right)$ represents for the variation of the hydrate saturation due to the hydrate formation/dissociation derived based on the pseudo kinetic model described in *Chapter.3*.

$$\frac{\partial}{\partial t}\left[\rho_h S_h \varphi\right] + \nabla.\left[\rho_h S_h \varphi \dot{u}\right] = f^h \tag{124}$$

$$\frac{DS_h}{Dt} = \left(\frac{f^h}{\varphi \rho_h}\right) - S_h\left(\frac{1}{\varphi}\frac{D\varphi}{Dt} + \frac{1}{\rho_h}\frac{D\rho_h}{Dt} + \nabla.\dot{u}\right) \tag{125}$$

$$S_h^{i+1} - S_h^i = \frac{f^h}{\varphi \rho_h} \tag{126}$$

Also, at each time-step, the liquid saturation is updated based on mass balance equation for liquid phase:

$$\frac{\partial}{\partial t}\left[\rho_w S_l^* \varphi^* \varphi(1-c) + \rho_s S_l^* \varphi^* \varphi c\right] + \nabla.\left[(1-c)\rho_w q_l + c\rho_s q_l + \rho_w S_l^* \varphi^* \varphi(1-c)\dot{u} + \rho_s S_l^* \varphi^* \varphi c \dot{u}\right] = f^l \tag{127}$$

where φ^* and S_l^* are the effective porosity and the effective liquid saturation respectively.

$$\varphi^* = \left(S_l + S_g\right) = 1 - \left(S_i + S_h\right) \tag{128}$$

$$S_l^* = \frac{S_l}{S_l + S_g} \tag{129}$$

By substituting the Darcy's equation and the density of liquid phase in Eq. (127), the variation of effective liquid saturation will be derived.

$$\frac{\partial}{\partial t}\left[\rho_l S_l^* \varphi^* \varphi\right] + \nabla.\left[\rho_l q_l + \rho_l S_l^* \varphi^* \varphi \dot{u}\right] = f^l \tag{130}$$

$$\frac{DS_l^*}{Dt} = \frac{f_l}{\varphi^* \varphi \rho_l} - S_l^*\left(\frac{1}{\varphi^*}\frac{D\varphi^*}{Dt} + \frac{1}{\varphi}\frac{D\varphi}{Dt} + \frac{1}{\rho_l}\frac{D\rho_l}{Dt} + \nabla.\dot{u}\right) - \frac{1}{\varphi^* \varphi}\nabla.q_l - \frac{q_l}{\rho_l \varphi^* \varphi}\nabla\rho_l \tag{131}$$

$$\frac{DS_l^*}{Dt} = \left(\frac{1}{\varphi^*}\frac{f_1^l}{\varphi\rho_w}\frac{\rho_w}{\rho_l} + \frac{\lambda\nabla P}{\varphi^* \varphi}\frac{\rho_s}{\rho_l}\right) - S_l^*\left(\frac{1}{\varphi^*}\frac{D\varphi^*}{Dt} + \frac{1}{\varphi}\frac{D\varphi}{Dt} + \frac{1}{\rho_l}\frac{D\rho_l}{Dt} + \nabla.\dot{u}\right) - \frac{1}{\varphi^* \varphi}\nabla.q_l - \frac{q_l}{\rho_l \varphi^* \varphi}\nabla\rho_l \tag{132}$$

in which f_1^l and $\lambda\nabla P\rho_s$ represent the source or sink of the liquid phase due to hydrate/ice formation /melting and erosion respectively.

The variation of liquid saturation due to hydrate/ice formation/melting is calculated based on the time independent kinetic model introduced in *Chapter.3* as follows:

$$S_l^{i+1} - S_l^i = \frac{f^l}{\varphi\rho_w} \tag{133}$$

Therefore, the updated effective liquid saturation is calculated as:

$$S_l^{*u} = S_l^* + \frac{1}{\varphi^*}\left[\frac{f_1^l}{\varphi\rho_w}\frac{\rho_w}{\rho_l} + \frac{\Delta t}{\varphi}\left(\lambda\nabla P\left(\frac{\rho_s}{\rho_l}\right) - \nabla.q_l\right)\right] - S_l^*\left(\frac{\Delta\varphi^*}{\varphi^*} + \frac{\Delta\varphi}{\varphi} + \frac{\Delta\rho_l}{\rho_l}\right) - \Delta t\left(S_l^*\nabla.\dot{u} + \frac{q_l}{\rho_l \varphi^* \varphi}\nabla\rho_l\right) \tag{134}$$

where Δt and S_l^* are the duration of the current time step and the liquid phase saturation at the previous time step respectively.

Consequently, the liquid and the gas phase saturation are derived based on following equations:

$$S_l^u = \varphi^{*u} S_l^{*u} = \left(1 - \left(S_h^u + S_i^u\right)\right)S_l^{*u} \tag{135}$$

$$S_g^u = \varphi^{*u}\left(1 - S_l^{*u}\right) = 1 - \left(S_l^u + S_h^u + S_i^u\right) \tag{136}$$

Finally, the volumetric concentration of eroded mineral particles c in the liquid phase is calculated based on the mass balance equation for fluidized soil particles.

$$\frac{\partial}{\partial t}\left(\rho_s c s_l \varphi\right) + \nabla.\left(\rho_s c q_l + \rho_s c s_l \varphi \dot{u}\right) = \rho_s \lambda\nabla P \tag{137}$$

$$\frac{Dc}{Dt} = -\left[\frac{c}{\rho_s} \frac{D\rho_s}{Dt} + \frac{c}{s_l} \frac{Ds_l}{Dt} + \frac{c}{\varphi} \frac{D\varphi}{Dt} + c\nabla.\dot{u} + \frac{c}{s_l\varphi} \nabla.q_l + \frac{cq_l}{s_l\varphi\rho_s} \nabla\rho_s + \frac{q_l}{s_l\varphi} \nabla c - \frac{\lambda\nabla P}{s_l\varphi} \right] \quad (138)$$

$$\frac{Dc}{Dt} = -\left[\frac{c}{\rho_s} \frac{D\rho_s}{Dt} + \frac{c}{s_l} \frac{Ds_l}{Dt} + \frac{c}{\varphi} \frac{D\varphi}{Dt} + c\nabla.\dot{u} - \frac{c}{s_l\varphi} \left(\frac{k\,k_{rl}}{\mu_l} \nabla^2 P + \nabla P \nabla.\left(\frac{k\,k_{rl}}{\mu_l} \right) \right) + \frac{cq_l}{s_l\varphi\rho_s} \nabla\rho_s + \frac{q_l}{s_l\varphi} \nabla c - \frac{\lambda\nabla P}{s_l\varphi} \right] (139)$$

6. CODE VALIDATIONS AND APPLICATIONS

A general mathematical formulation has been developed further to analyze coupled THCM problems involving HBS (*Chapter.3*). This truly coupled formulation incorporates the different phases (including solid, liquid, gas, hydrate, and ice) and species (i.e., water, methane, solutes and minerals). It takes into consideration thermal processes (i.e., conduction, phase transformation), hydraulic processes (i.e., multiphase multicomponent flow), effective-stress dependent sediment response, presence of solutes, and changes in sediment properties in the existence of hydrates. The formulation was implemented in CODE_BRIGHT, an existing fully coupled multiphysics 3D finite element program for geological media (Olivella et al. 1996), in order to advance the current understanding of HBS as well as to investigate/optimize production strategies and implications.

The proposed numerical framework was verified against the analytical solutions, which were developed as a part of this study (*Chapter.4*).

The simulation of two gas production tests, under controlled conditions on natural samples from the Krishna-Godavari Basin and the Ulleung Basin, conducted in the lab were also analyzed. These experiments are very useful for both, to advance the current knowledge about the complex behavior of sediments under these conditions, and to validate numerical tools. The main tendencies observed in the experiments, in terms of pressure evolution, gas produced, and temperature were qualitatively well captured by the models. The models also assist to understand the propagation of the dissociation fronts inside the samples and the patterns of ice formation during the experiments.

Moreover, two models were developed that replicate the temperature and pressure evolutions during (around) $2,000 \times 10^3$ years that have led to the formation of gas hydrate at Mount Elbert site, Alaska.

6.1. Code Validation Against Experimental Data

6.1.1. The Pressure Core Testing at the Krishna-Godavari Basin

Yun et al. (2010) characterized a natural HBS recovered from the Krishna-Godavari Basin offshore India during the first Indian National Gas Hydrate Program expedition in 2006. The Instrumented Pressure Testing Chamber, IPTC, was used to gather good quality specimens and maintain them at 4° C and 13 MPa. A 21C-02E core of 380mm length and 50mm diameter was subsampled under pressure to simulate depressurization induced gas production. The index properties of this specimen are shown in Table.6.1 and fully reported in Yun et al. (2010). Figure.6.1 presents the X-ray image of the sample prior to testing in which darker colors represent high density sediments while lighter colors indicate low density materials like gas hydrates or cavities. The controlled depressurization of the pressure core begun with a gradual decrease of the hydrostatic pressure at an average rate of 0.18 MPa/min, until reaching the hydrate stability phase boundary. The depressurization rate was reduced afterwards, up to about 0.025 MPa/min, until reaching the atmospheric pressure. The temperature was continuously measured during the controlled depressurization with a thermocouple located 54mm away from the valve (Figure.6.1a).

Table 6-1 Index properties of the 21C-02E core specimen (from Yun et al. 2010)

Properties	Values	Device/Technique
pH	7.75-8.5	Nonbleeding pH strip ($\pm$ 0.25)
Specific surface (S_a, m^2/g)	87-94	Methylene blue adsorption
Liquid limit (w_L, %)	73-75	Fall cone
Plastic limit (w_P, %)	34-36	ASTM D4318-05
Plastic index (w_L-w_P)	40	
Gravimetric water content (w_C, %)	60-65	Oven dry (ASTM D2216)
Porosity (φ)	0.61-0.63	Computed from w_C assuming specific gravity G_S = 2.65

To represent the cylindrical sample, a 2-D axisymmetric model was adopted with a uniform mesh discretization consisting of 750 elements. The first analysis is based on assuming a homogeneous hydrate distribution of 0.298 (Yun et al., 2010). The initial conditions correspond to the experimental ones: P=13 MPa, T=4° C and φ=0.61. An impermeable flow boundary around the shell is considered except at the ball-valve position imposed the depressurization rate discussed above. A heat radiation condition around the shell for the thermal problem is implemented. Furthermore, the hydrate phase boundary described by Eq. (32) for a salt concentration of around 4 % and the ice-liquid water phase boundary given by Eq. (33) are applied. The other parameters implemented in the numerical models are summarized in Table.6.2.

Table 6-2 Model parameters used in numerical simulation of the 21C-02E core specimen.

Parameter	Value
Average initial saturation	S_h=0.298, S_l=0.702, S_g=0.00
Intrinsic permeability in HBS	k_{HBS}=1.9x10^{-12} m^2 (Isotropic: $k_x = k_y = k_z$)
Porosity of HBS	φ=0.61
Capillary pressure model	Po=100 kPa; λ=0.5
Liquid relative permeability model	$a = 3$
Gas relative permeability model	$b = 3$

(a)   (b)   (c)

Figure 6.1 Schematic view of a HBS subsample specimen (21C-02E), indicating the position of ball-valve, and the thermocouple (from Yun et al., 2010); b) image selected for developing the 3D heterogeneous model; c) distribution of hydrate saturation in the heterogeneous model.

The evolution of the experimental and modeling P-T trajectory are presented in Figure.6.2a. The endothermic character of the hydrate dissociation is well captured by the model, predicting a sharp change of the P-T path direction (i.e. towards the left, in the P-T plane), once the hydrate phase boundary is touched. The heat consumed during hydrate dissociation induces a significant

cooling of the sample reaching subzero temperatures. Once the hydrate dissociation is completed, the path leaves the phase boundary and the temperature increases because of the ambient heat and the exothermic of ice formation. The simulated P-T trajectory satisfactorily reassemble the experiment one. Figure.6.2b shows the experimental and simulated pressure evolution versus time, where the two depressurization rates discussed above are clearly observed. Figure.6.2c presents the comparison between experimental and simulated gas production. The model predicts well the maximum amount of produced gas, but at a faster rate at advanced stages of the experiment. The main trends observed in terms of temperature evolution are qualitatively well simulated (Figure.6.4d), but the minimum temperature is underpredicted by the model (i.e. model~-5 °C, test~-2.5 °C). The thermocouple was located (Figure.6.1a) in a zone in which hydrate saturation is lower than the average value, it is then possible that the local temperature at that position may be higher than the ones developed in other sections. A model based on a homogenous hydrate distribution cannot capture this type of trend. Therefore, a model considering a heterogeneous hydrate distribution was developed to achieve a better description of the test conditions.

Figure.6.3 presents the contours of hydrate distribution during depressurization. The dissociation front propagates initially from the bottom of the sample (where the depressurization is induced) and stabilizes at a distance of around 6.5 cm from the bottom. After 110' (approximately) a radial front also develops (i.e. triggered by the ambient heat transfer from outside), which progresses towards the center of the sample until the end of the experiment.

One of the core X-ray images (Figure.6.1b) was adopted to develop a 3D model considering a 2D axisymmetric geometry (Figure.6.1c) using MATLAB tools to assign different hydrate saturations based on the specimen grayscale color. According to the experiment, the volume of hydrate in the 21C-02E subsample was estimated as 136cm^3, which results in an average hydrate saturation of 0.298. This model perhaps does not capture the full complexity and variability of hydrates saturation observed in the natural sample, but do represent an improvement respect to the homogenous model. The new model simulation was conducted under the same conditions adopted for the homogeneous model. Figure.6.4 presents the main results associated with this modelling. The main difference respect to the previous analysis is that now the minimum temperature recorded during the test is perfectly captured by the heterogonous model.

67
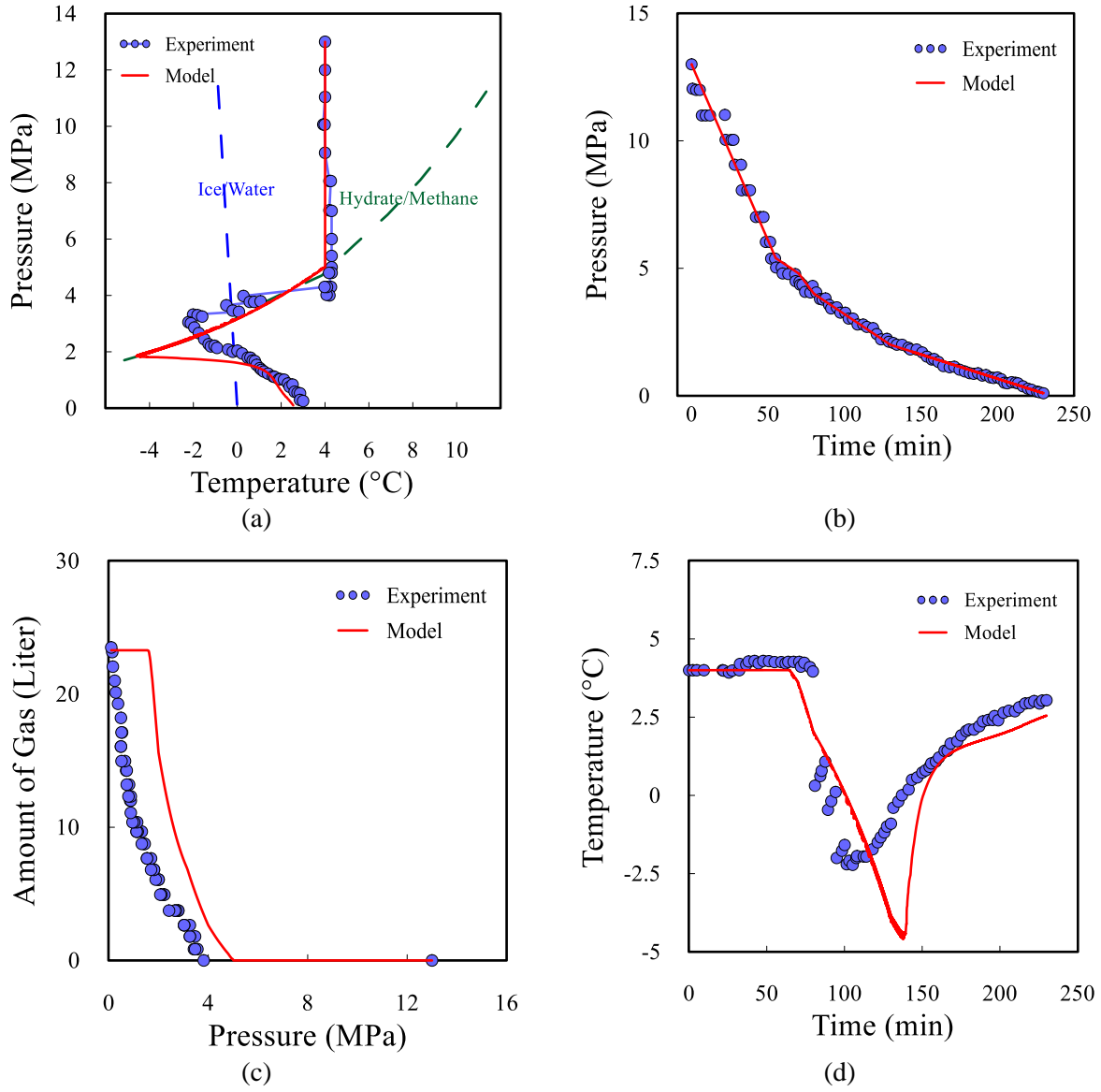
Figure 6.2 Experimental results versus numerical analysis based on the homogeneous hydrate distribution: a) the P-T paths and phase boundaries, b) time evolution of pressure, c) gas produced in terms of pressure evolution, and d) temperature evolution during the experiment.
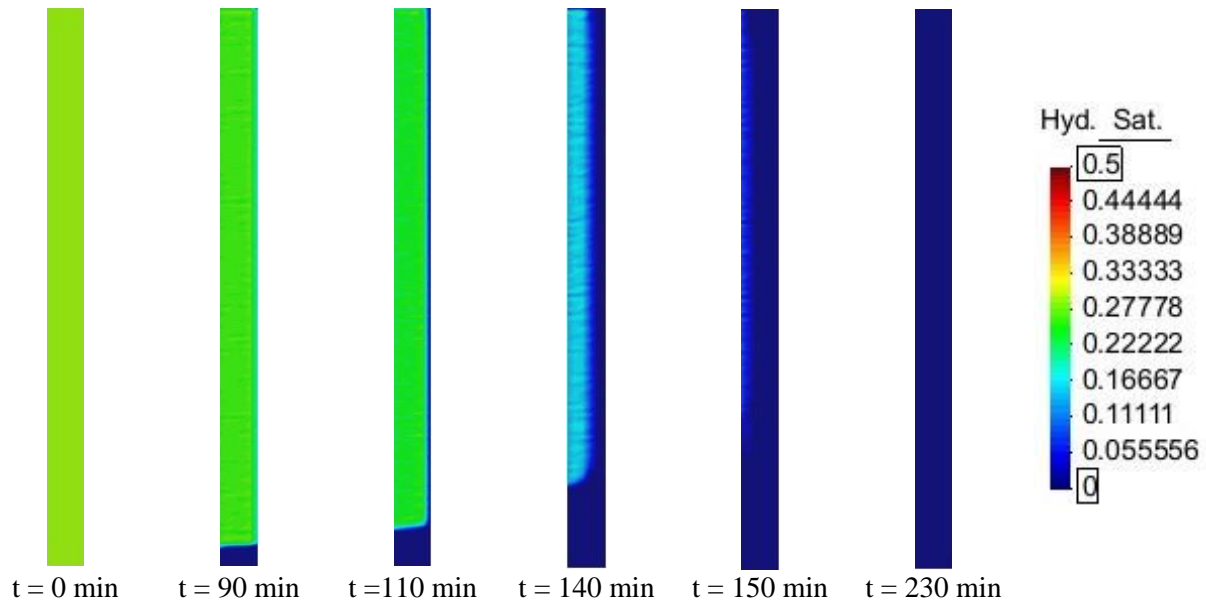
Figure 6.3 Evolution of contours of S_h with time, analysis assuming a homogenous hydrate distribution.

In the P-T plane, the changes in hydrate and ice saturations are also included during the experiment (Figure.6.4a). S_h starts to decrease when the hydrate boundary is reached by the P-T path (i.e. point 1) and continues reducing until point 3, when all the hydrate dissociates. S_i starts to from when the P-T trajectory reaches the ice-liquid water transition (i.e. point 2), and continues forming until the phase transition is reached again (i.e. point 4), during the heating of the sample induced by the surrounding and also the exothermic of ice formation. Beyond this point, the ice starts to decrease because of thawing.
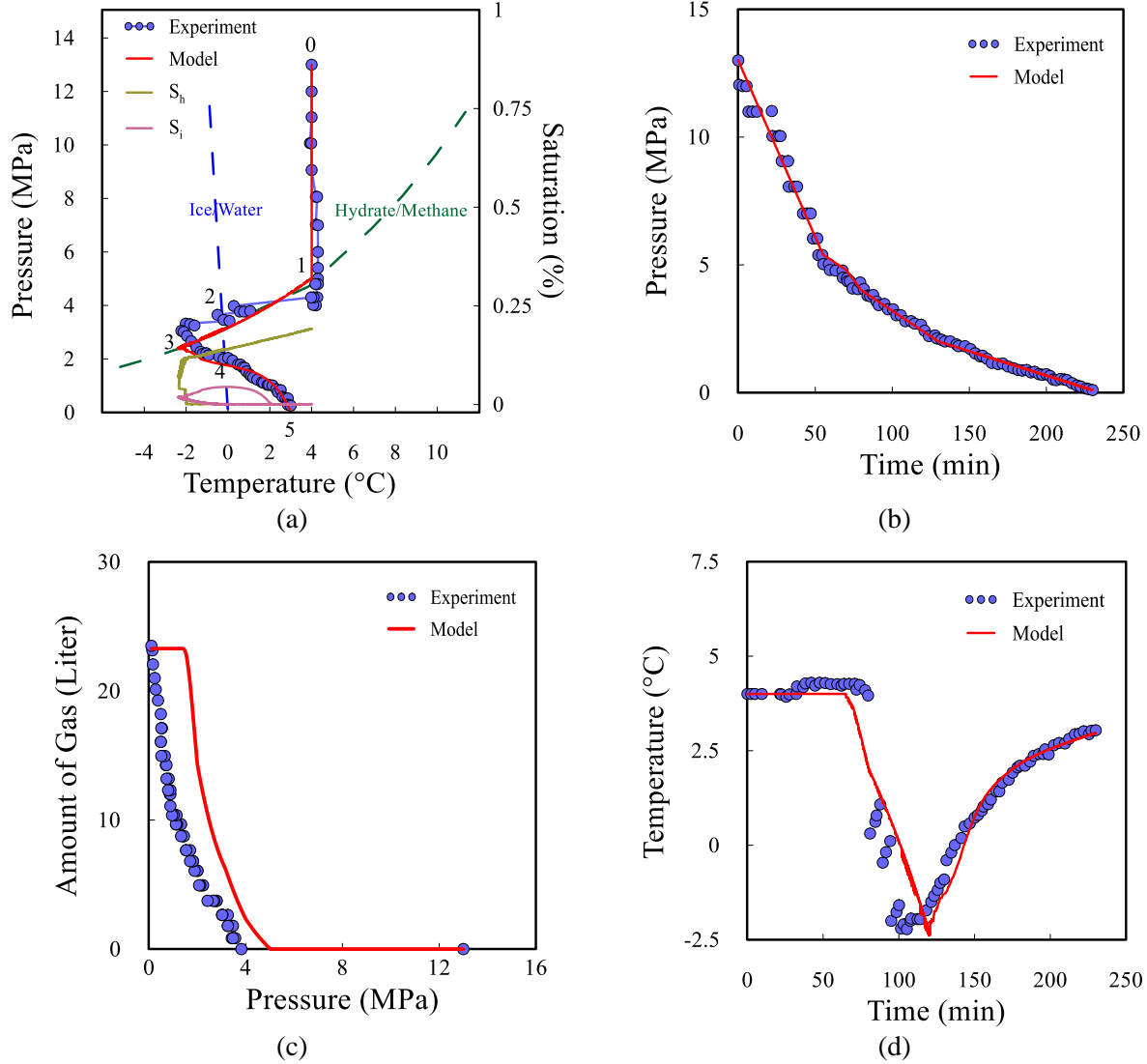
Figure 6.4 Experimental results versus numerical analysis based on the heterogonous hydrate distribution: a) the P-T paths and phase boundaries, b) time evolution of pressure, c) gas produced in terms of pressure evolution, and d) temperature evolution during the experiment.

The under-prediction of the minimum temperature obtained in the initial analysis was not related to a possible deficiency of the proposed formulation to properly capture the cooling during the endothermic hydrate dissociation, but to the impact of the no-uniform S_h distribution on this process.

The contours of S_h distribution is also plotted during depressurization (Figure.6.5). The two clear dissociation fronts observed in the homogenous analysis are also apparent in this case, but they are much less marked than before.
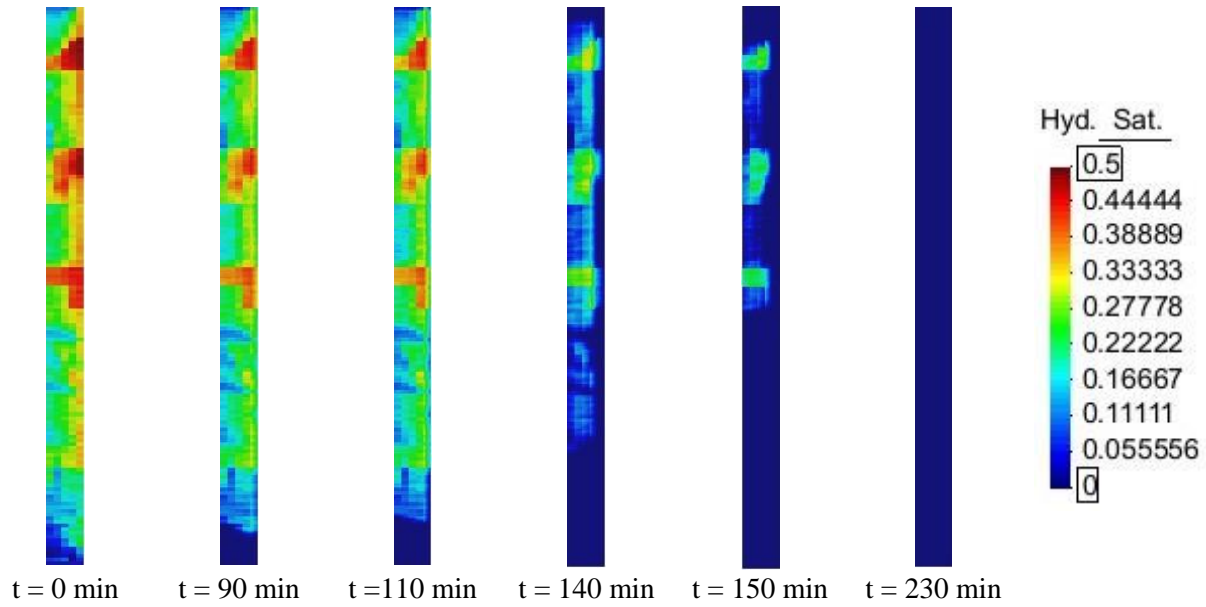
Figure 6.5 Evolution of contours of S_h with time, analysis assuming a heterogeneous hydrate distribution

In addition to above, a simple 1D plain strain model consists of 3 elements of 4 nodes is used to simulate methane hydrate dissociation under the same condition. Figure.6.6 reports the results of this analysis. As it is illustrated, the P-T path follows the ice/water boundary when all the hydrates dissociate. In other words, the numerical model captures the exothermic behavior of ice formation. Since the heat provided by surrounding is not defined as boundary conditions in this 1D model, the endothermic behavior of hydrate dissociation is just partially compensated by exothermic effect of ice formation. On the other hand, as both ice and liquid phases exist in the truly isolated model by the completion of hydrate dissociation, the P-T path follows the ice/water phase boundary in order to satisfy the equilibrium.

71
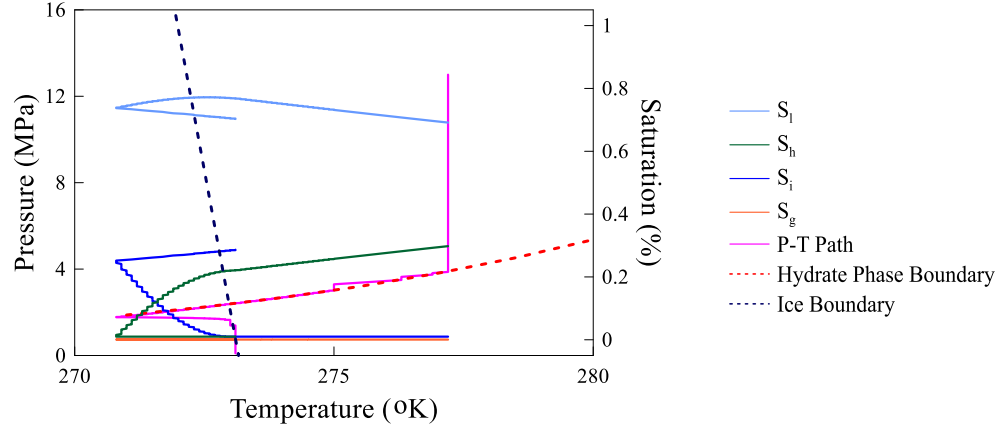
Figure 6.6 The P-T path in 1D numerical model with respect to the ice/water and the methane hydrate phase boundary.

6.1.2. The Pressure Core Testing at the Ulleung Basin, Sea of Japan

In order to assess the existence of the HBS, to recover deep offshore sediments containing methane hydrates, and to investigate physical properties of the HBS, the Korea UBGH01 was performed during the summer and fall of 2007.

By using the IPTC, which gathered good quality specimens and maintained them at $4\,^{\circ}$C and 15 MPa, Yun et al. (2011) characterized a natural HBS recovered from the Ulleung Basin during the first Korea UBGH expedition. A 10B-17P core of 822mm length and 50mm diameter was subsampled under pressure to simulate depressurization induced gas production. The index properties of this specimen are shown in Table.6.3 and fully reported in Yun et al. (2011).

Table 6-3 Index properties of the 10B-17P core specimen (from Yun et al. 2011).

Properties	Values	Device/Technique
Specific gravity, G_s	2.57	ASTM D854
Specific surface (S_a, m^2/g)	31	N_2 adsorption
Clay content (%)	12	Less than 2 µm
Liquid limit (w_L, %)	115	ASTM D4318
Plastic limit (w_P, %)	65	ASTM D4318
Plastic index (w_L-w_P)	50	
Soil classification	OH or MH	USCS system

Figure.6.7 illustrates the X-ray image of the sample prior to testing in which darker colors represent high density sediments while lighter colors indicate low density materials like gas

72

hydrates or cavities. The controlled depressurization of the pressure core established with a gradual reduction of the hydrostatic pressure at an average rate of 0.146 MPa/min for 50 min, until reaching the hydrate stability phase boundary. The depressurization rate was reduced afterwards, up to about 0.0115 MPa/min, for 130min until reaching 3.2MPa. Then, the valve was closed to keep the entire mass of chamber constant around 8 hours, from t=180min to t=650min. According to the experiment, the temperature remained constant at $1.2\,^{\circ}C$, while there was a slight rebound in pressure from 3.2MPa to 3.7MPa during this time. Again, the depressurization continued by opening the value from t=650min to t=830min to reaching the atmospheric pressure. The temperature was continuously measured during the controlled depressurization with a thermocouple located 422mm away from the valve (Figure.6.7).
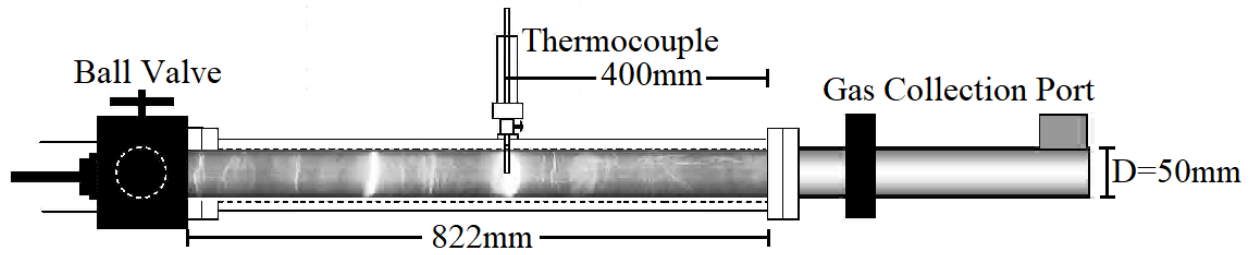
Figure 6.7 Schematic view of a HBS specimen (10B-17P), indicating the position of ball-valve, and the thermocouple (from Yun et al., 2011).

A 2-D axisymmetric model was adopted with a uniform mesh discretization consisting of 750 elements in order to represent the cylindrical sample. The model is based on assuming a homogeneous hydrate distribution of 0.195 (Yun et al., 2011). The initial conditions correspond to the experimental ones: P=12 MPa, T=3.5°C and φ=0.75. An impermeable flow boundary around the shell is considered except at the ball-valve position imposed the depressurization rate discussed above. A heat radiation condition at the valve for the thermal problem is implemented. Furthermore, the hydrate phase boundary described by Eq. (32) for a salt concentration of around 2.05% and the ice-liquid water phase boundary given by Eq. (33) are applied. The other parameters implemented in the numerical models are summarized in Table.6.4.

73

Table 6-4 Model parameters used in numerical simulation of the 10B-17P core specimen.

Parameter	Value
Average initial saturation	$S_h=0.195$, $S_l=0.805$, $S_g=0.00$
Intrinsic permeability in HBS	$k_{HBS}=1.9 \times 10^{-12}$ m^2 (Isotropic: $k_x = k_y = k_z$)
Porosity of HBS	$\varphi=0.75$
Capillary pressure model	Po=100 kPa; $\lambda=0.5$
Liquid relative permeability model	$a = 3$
Gas relative permeability model	$b = 3$

The evolution of the experimental and modeling P-T trajectory are shown in Figure.6.8a. The endothermic behavior of the hydrate dissociation is well captured by the model, predicting a sharp change of the P-T path direction (i.e. towards the left, in the P-T plane), upon touching the hydrate phase boundary. The heat consumed during hydrate dissociation induces a significant cooling of the sample reaching subzero temperatures. Once the hydrate dissociation is completed, the path leaves the phase boundary and the temperature increases because of both the ambient heat and the exothermic character of ice formation. The simulated P-T trajectory is satisfactorily compatible with the experiment one. Figure.6.8b presents the experimental and simulated pressure evolution versus time, where the aforementioned depressurization rates are clearly observed. Moreover, the slight pressure rebound happened during t=180min to t=650min in the experiment, because of the closed valve condition and keeping the entire mass of chamber constant, is also captured by the model. Figure.6.8c presents the comparison between experimental and simulated gas production. The model predicts well the maximum amount of produced gas. The trends observed in terms of temperature evolution are qualitatively well simulated (Figure.6.8d).

Although for analyzing the subsampled 21C-02E specimen from Krishna Godavari Basin, the heterogeneous model is required to capture the exact experimental results, but in the case of the 10B-17P core sample form the Ulleung Basin, outcomes of the homogeneous model are satisfactory compatible with that of the experiment as shown in Figure.6.8. The main difference between these two cases is the location of the thermocouple. However, in the first experiment, the thermocouple was located close to the valve and the heterogeneity of hydrate distribution is considerable at that location, for testing the 10B-17P specimen, the temperature was measured at the half length of the sample and the average of hydrate distribution beyond and back of this point is approximately the same.
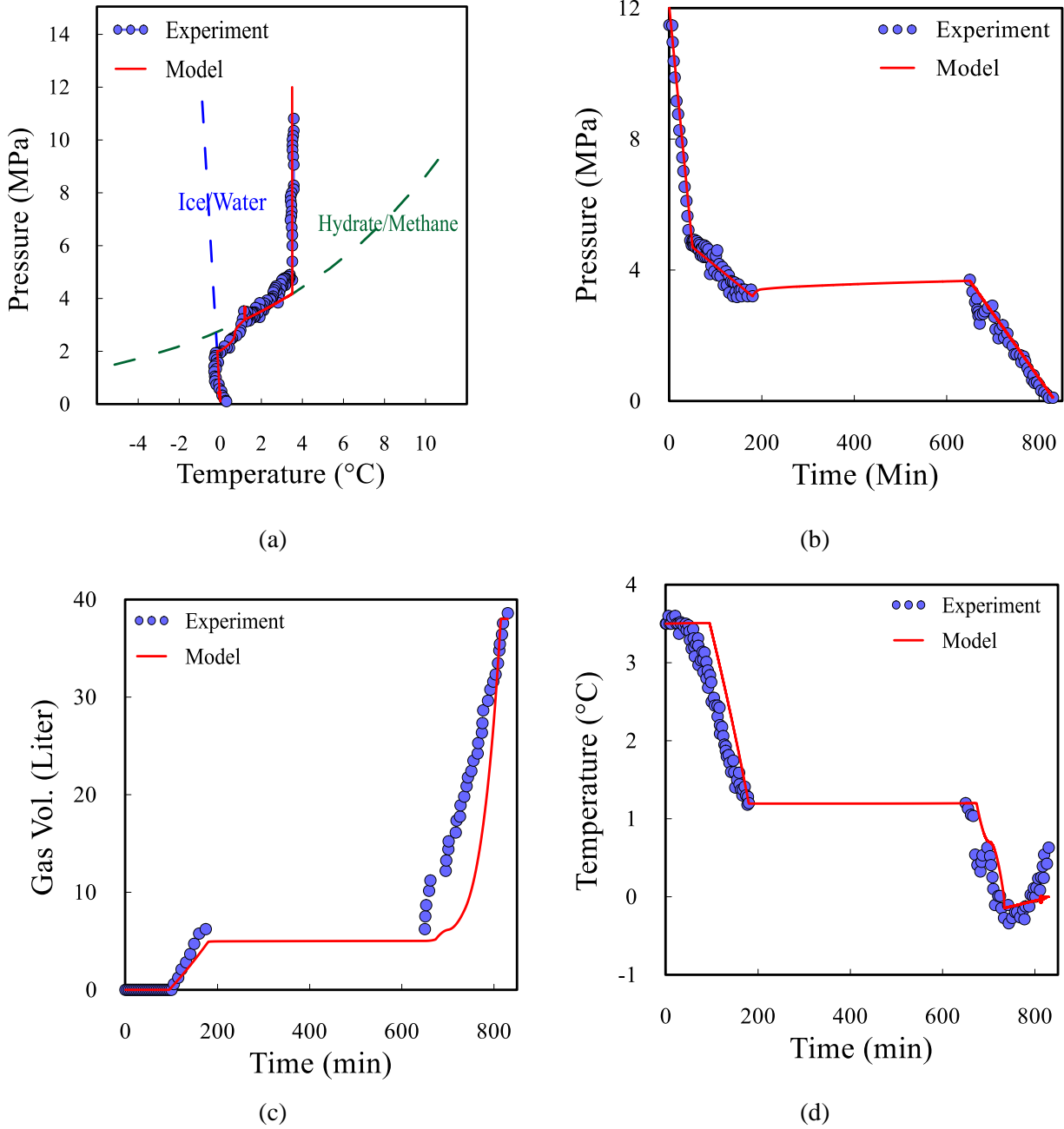
Figure 6.8 Experimental results versus numerical analysis of the specimen 10B-17P: a) the P-T paths and phase boundaries, b) time evolution of pressure, c) time evolution of produced gas, and d) temperature evolution during the experiment.

Figure.6.9 presents the contours of hydrate distribution during depressurization. Since the chamber was isolated from the environment and there was no heat radiation from the shell, oppose to the depressurization of core specimen from Krishna Godavari Basin, the dissociation front propagated only from the valve (where the depressurization was induced).
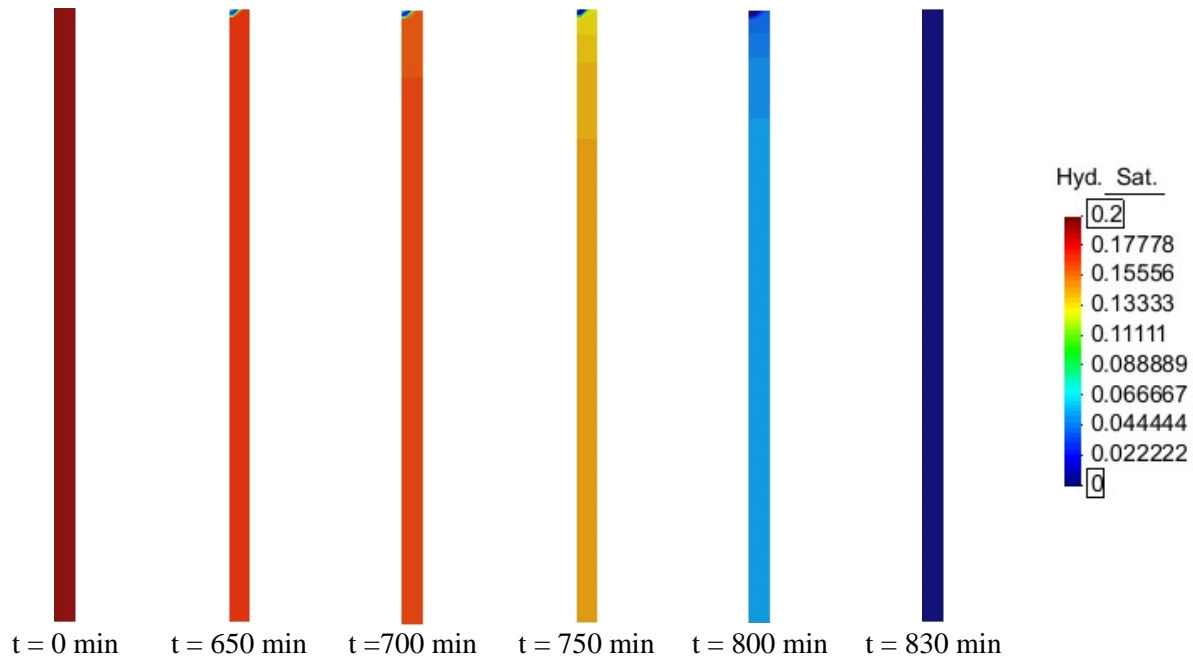
Figure 6.9 Evolution of contours of S_h with time, numerical analysis of the specimen 10B-17P.

6.2.Hydrate Formation in Permafrost Settings

The previous simulations focused on problems involving hydrate dissociation, hereafter the formation of methane hydrates under the specific hydrostatic conditions of high pressure and low temperature commonly found in permafrost layers is analyzed. According to information on permafrost and ground surface temperature (Wolfe, 1980,1994; Brigham & Miller, 1983; Wolfe & Upchurch, 1987; Parrish et al., 1987; Spicer & Chapman, 1990; Elias & Matthews, 2002; Matheus et al., 2003; Kaufman et al., 2004; Bujak Research International, 2008), stratigraphic and geologic information from Alaska North Slope (Reimnitz et al., 1972; Bird, 1981,1999; Collett et al., 1988; Valin & Collett, 1992; Frederiksen et al., 1998; Inks et al., 2008), and logging data gathered for the Mount Elbert, Dai et al. (2011) reconstructed the evolution of the ground surface elevation (GSE), the ground surface temperature (GST), the gas hydrate stability zone (GHSZ), and the base of ice bearing permafrost (BIPF) at Mount Elbert site, Alaska North Slope region (Figure.6.10). It was assumed that continuous permafrost was formed when the mean annual ground surface temperature was below -5 °C and the temperature at the BIPF was -1 °C. Furthermore, a linear geothermal gradient of -1.64 °C/100m and -3.56 °C/100m are considered

76

above the BIPF and below the permafrost, respectively (Lachenbruch et al., 1982; Collet et al., 1988, 2008; Collet, 1993). The fluid pressure is hydrostatic and water table was assumed at GSE. Two main formations with high S_h (i.e. between 60% and 75%) have been identified in this area: a shallower Unit D (depth: ~614m to ~628 m), and a deeper Unit C (depth: ~650 m to ~666 m).

As reported in Dai et al. (2011), different possible scenarios have been proposed to explain the presence of hydrates in these layers. For example: i) the preexistence of gas reservoirs that were transformed into hydrates sediments triggered by favorable P-T conditions was suggested, ii) the slow and progressive increase of hydrate saturation formed from biogenic or migrated thermogenic gas that arrives at the stability zone.
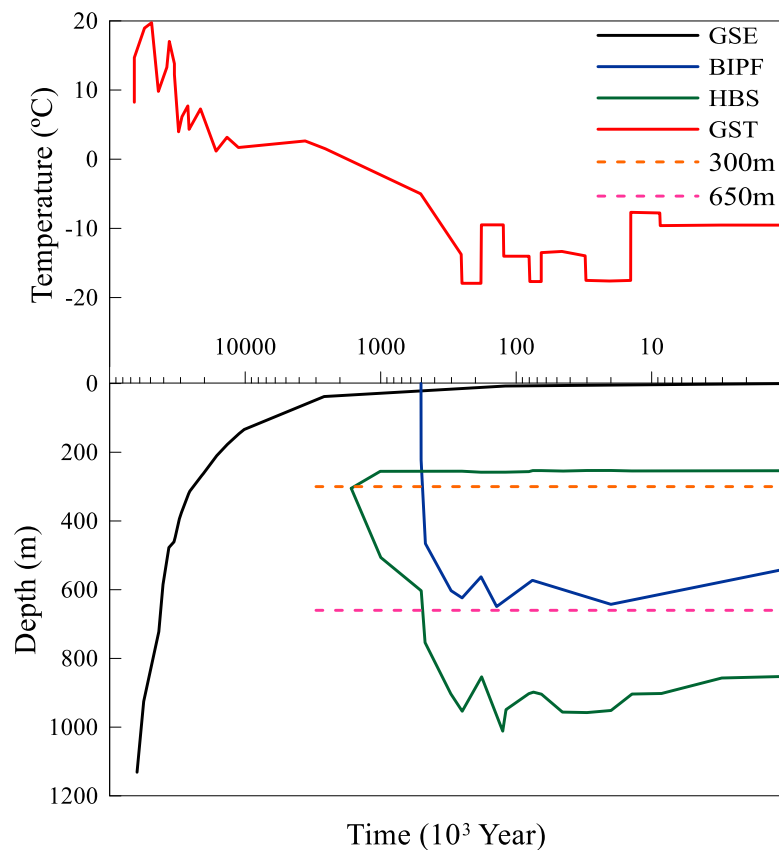
Figure 6.10 Evolution of the ground surface elevation (GSE), the ground surface temperature (GST), the base of ice bearing permafrost (BIPF), and the gas hydrate stability zone (GHSZ) at Mount Elbert site (from Dai et al. 2011). The depth is based on the current ground surface and time is shown in logarithmic scale in unit of thousand years reverse to the present time.

77

In order to replicate the both aforementioned scenarios, two models were prepared at two different levels, which are at 300m and 650m below the current GSE shown in the orange and the pink dash line in Figure.6.10 respectively.

A 1D plain strain numerical model consists of 3 elements and 4 nodes is studied based on the evolution of pressure and temperature at depth 300m (i.e. the orange dash line in Figure.6.10), which is derived from the aforementioned information.

At the initial condition, the value of both liquid and gas saturation is 0.5 and it is free of both hydrate and ice phase. The raise of the GSE and the reduction of the GST provide favorable condition of hydrate formation. With a rough calculation, according to the abovementioned initial liquid and gas phase saturation, the phase density at corresponding pressure and temperature upon touching the hydrate phase boundary, and the assumed hydration number of 5.75, which results in value 0.866 for the fractional mass of water in methane hydrate, the final hydrate phase saturation should be equal to 0.09 (Figure.6.12), which is satisfactory compatible with the results of numerical mode. Higher reductions of the GST in following time steps cause the formation of permafrost and extends the area with the favorable conditions for hydrate formation by cooling the deeper sediments (Figure.6.11)

Figure 6.11 Evolution of pressure, temperature at depth of 300m derived from Dai et al, (2011); evolution of phase saturations reported by the numerical analysis.

Figure 6.12 Evolution of phase saturations and the P-T path with respect to the ice/water and hydrate phase boundary for the model located at 300m below the current GSE reported by the numerical analysis.

To study the hydrate formation under the second scenario discussed above, a point level analysis to mimic the conditions prevailing at the Unit C (i.e. the pink dash line in Figure.6.10) was adopted. This model is based on the hypothesis that considers a sediment almost fully water saturated and in which hydrates form because of the continuous arriving of gas. Scenarios with a larger amount of initial free gas can also be simulated (Figure.6.13).
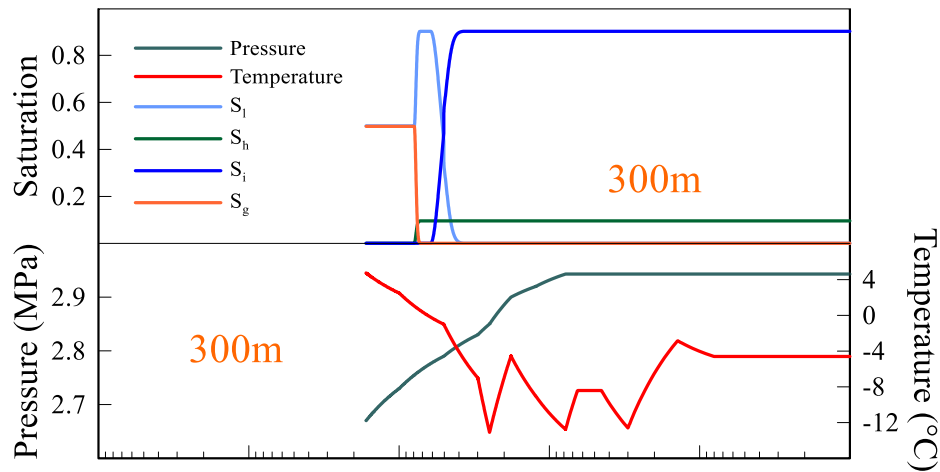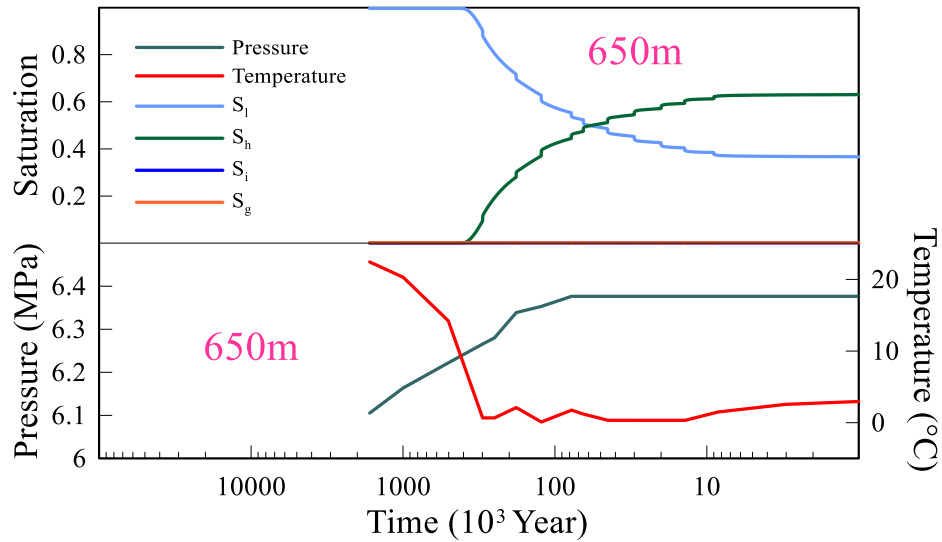

Figure 6.13 Evolution of pressure, temperature at depth of 650m, the Unit C, derived from Dai et al, (2011); evolution of phase saturations reported by the numerical analysis.
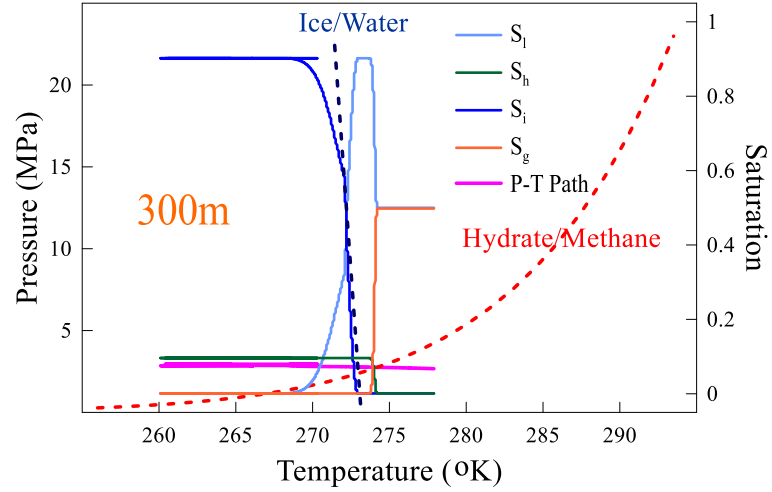
79
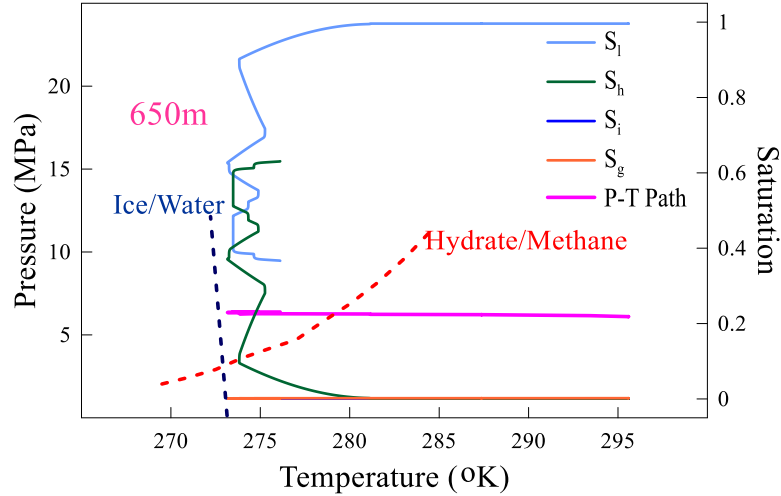
Figure 6.14 Evolution of phase saturations and the P-T path with respect to the ice/water and hydrate phase boundary for the model located at 650m below the current GSE, the Unit C, reported by the numerical analysis.

The temperature evolution at the Unit C was estimated based on the BIPF/GST and the corresponding geothermal gradients suggested by Dai et al. (2011). Also, according to Dai et al. (2011) assumption, P was calculated based on the GSE. The raise of GSE and the reduction of GST provide favorable conditions for hydrate formation. Hydrates start to form upon the P-T path touching the phase boundary (Figure.6.14) and continued increasing afterwards with the progressive reduction of S_l, (i.e. because the volume of voids is gradually occupied by hydrates). S_g remains very small during the whole analysis. Under the assumed conditions, the model predict a current S_h~0.63, which is compatible with the reported values (Lee & Collet, 2011).

6.3. Discussion

A variety of problems involving HBS have been analyzed with the proposed numerical code; from small scale laboratory tests to field scale simulations, and involving hydrate formation/dissociation, as well as, ice formation/melting.

The simulation of two gas production tests conducted in the lab are analyzed under controlled conditions on a natural HBS sample. This type of experiment are very useful for both, to advance the current knowledge about the complex behavior of sediments under this condition, and to validate numerical tools. The main tendencies observed in the experiments, in terms of pressure

80

evolution, gas produced and temperature are qualitatively well captured by the model. However in case of analyzing the specimen of the Krishna Godavari Basin, the adopted model under-predicts the recorded temperature during hydrate dissociation. To achieve a better description of the complex S_h distribution observed in the specimen under study, a model that contemplates a non-uniform hydrate distribution is developed, which is able to capture very satisfactorily the observed experimental behavior, confirming that the main physics that control this problem are properly implemented in the formal framework. Also, the experimental dissociation test on the specimen from Ulleung Basin is simulated and based on the location of thermocouple, the heterogeneity of hydrate distribution does not have considerable effects on the results. Both models also assisted to understand the propagation of the dissociation fronts inside the sample and the patterns of ice formation during the experiment. The two different set of assumptions behind of these two experiments address the characteristic behaviors of hydrate dissociation.

Further, two models are developed, which replicate the temperature and pressure evolutions during (around) $2,000 \times 10^3$ years that have led to the formation of gas hydrate at Mount Elbert site, Alaska. It was assumed that the hydrates were formed at depth 300m below the current ground surface elevation by consuming the preexisting gas upon providing the favorable P-T conditions by arising the elevation and cooling the temperature at the ground surface elevation. The concentration of formed hydrate is compatible with that of calculated theoretically. Based on the other scenario assuming hydrates were formed at depth 650m below the current ground surface by consuming migrated gas from lower elevation a $S_h \sim 0.63$ was computed, which concurs with the reported hydrate saturation in the unit under analysis.

7. CONCLUSIONS

Methane hydrate reservoirs have been known as a huge source of clean energy. The crystalline structure of hydrate is dissociated, which results in releasing significant volume of methane gas by the aid of depressurization, CH_4-CO_2 replacement, heat and/or chemical stimulation.

The experimental study of HBS has been hindered by the very low solubility of methane in water (preparing artificial samples in lab), and inherent sampling difficulties associated with depressurization and thermal changes during core extraction. This situation has prompted more decisive developments in numerical modeling in order to advance the current understanding of hydrate bearing sediments, and to investigate/optimize production strategies and implications.

Numerical simulation of methane hydrate gas production is also challenged by the complex behavior of HBS since hydrate dissociation comes along with interrelated THCM processes. Moreover, the potential ice formation during hydrate dissociation possess additional difficulties in numerical modeling. Complex stress paths in the P-T space with two phase boundaries (i.e. ice-liquid and gas-hydrate phase lines) are anticipated during gas production, including secondary ice and hydrate formation.

A critical component of this research is a coupled THCM formulation for HBS that allows integrating, in a unique and consistent framework, all the physics and interactions that control the behavior of this type of soil. It is a truly coupled mathematical framework that solves all the governing equations simultaneously in a monolithic manner. This robust numerical framework is able to capture the P-T paths and ensuing phase transmissions during methane hydrate gas production in both marine and permafrost settings based on the analysis of available data from laboratory tests and field experiments.

Therefore, by deep understanding the inherent natural behavior of HBS, a computer code has been developed to analyze problem associated with HBS. This finite element computer program takes into consideration thermal and hydraulic processes in deformable porous media, also accounts for the changes in sediment properties in the presence of hydrate dissociation/formation,

82

and it has been implemented in CODE_BRIGHT (Olivella et al., 1996), an existing coupled multiphysics program for geological media.

The proposed numerical code paves the path to advance the current knowledge of HBS; to simulate the hydrate dissociation/formation more efficiently and precisely; to investigate the crucial parameters, which affects the methane hydrate gas production; to optimize the future field production studies in marine and permafrost sediments; to minimize the hazardous side effects; to address the most pertinent questions that have emerged from both past lab tests and previous field scale experiences.

Implementing the novel pseudo kinetic model in this framework makes it possible to simulate the two-way phase transitions for both ice and hydrate and avoids complexities of the classical model.

Considering fully coupled THCM formulations instead of sequential methods makes the numerical analysis much more straightforward and accurate because of preventing linking two or more different numerical codes to study the problems involving HBS and avoiding one-way coupling, which cannot truly replicate the inherent behavior of HBS.

According to the presented framework, comprehensive 1D models were studied in *Chapter.3* to address the inherent behavior of HBS and the proposed numerical code successfully captures the complex phenomena associated with hydrate formation/dissociation.

When solving engineering problems both transient and steady state analyses are relevant. Transient solutions are typically used, amongst others, to learn about gas production rate, to investigate optimal production strategies, and to perform sensitivity studies aimed at understanding the impact of material parameters (and other factors) on gas production. Steady state analyses are equally relevant because they demonstrate about the limit (or the final condition) of the problem under study.

In this study, an analytical solution was also developed for the steady state condition involving fluid flow in an axisymmetric cylindrical geometry with various confining situations and accounting for the presence of two zones of different permeability coefficients for HBS and free hydrate sediments within the reservoir. This solution can be very useful in problems encompassing HBS as it provides the physical limit to the zone around a vertical well that can experience

dissociation triggered by depressurization. From this solution, it is possible to learn about the maximum amount of gas that can be produced from a given reservoir under these assumptions.

The suggested analytical solution predicts the ultimate radius of the depressurization induced dissociation front in HBS at the steady state equilibrium based on reservoir initial conditions, hydrate morphology and its pertinent effect on sediment properties, induced pressure at the vertical well, and the most important of all, the boundary conditions, geometries and properties of reservoir confining layers.

The numerical simulations have been combined together with analytical solutions and constitutive modeling, with the aim of achieving a better understanding of the behavior of HBS. To validate the FE program, the results of the analytical solution were compared against the outputs of a numerical model replicating the same conditions. Since the analytical solution depends on crucial factors which affect hydrate dissociation like the dependency of sediments properties on the hydrate morphology, the induced pressure at the wellbore, the initial pressure, and the temperature of HBS deposit, the effects of critical factors were also analyzed and discussed in *Chapter.4* and the results of both analytical solution and numerical models are compatible. For example, it is predicted that the dissociation front is the farthest (from the well) when the permeability contrast between already dissociated and hydrate sediments is the highest. This implies that the permeability enhancement during dissociation plays an essential role in the depressurization propagation in hydrate reservoirs. For a fixed k_{Sed}/k_{HBS}, the effect of the reservoir initial temperature was assessed (i.e. all the other factors are identical) showing that the larger amount of gas is released from warmer reservoirs. Moreover, under conditions in which all the factors are the same except the initial pressure, it was observed that the lower the initial reservoir pressure, the higher the amount of gas produced. Similar meaningful discussions can be conducted involving other variables and factors, showing the usefulness of this type of solution.

Furthermore, outputs of the developed numerical model were compared with those of the proposed analytical solution for the steady state conditions. The comparison between numerical model and analytical solution confirmed that the proposed numerical code is well suited to estimate the limits of gas production from HBS reservoirs.

According to the analytical solution, generally, the most efficient depressurization is related to a perfectly confined reservoir, but for the reservoir, which is confined by low permeable layers,

favorable condition is the existence of a vertical impermeable rock around the ultimate radius affected by depressurization derived as a function of the leakage factor. Also depressurization has the lowest efficiency in the reservoir confined by finite low permeable layers with the length shorter than affected radius of depressurization and connected to high permeable porous medium beyond that point.

In addition, defining realistic boundary conditions is one of the most essential requirements to get reasonable results from numerical modeling. By having proper simple data from reservoir horizontal and vertical confining layers, the suggested analytical solution can help to define realistic boundaries and also determine the influence zone of depressurization.

Sand production is a relatively well-known problem that has been extensively studied in the context of hydrocarbon production from conventional reservoirs. However, this problem associated with methane production from HBS possess new and significant challenges that require further research. A significant difference is that hydrate dissociation induces profound changes in the sediment structure, facilitating even more disaggregation of particles and their subsequent transport. A review of current methods to study sand production was provided in *Chapter.5* and comprehensive augmented formulations, based on the framework presented in *Chapter.3*, were developed to enhance the numerical code for the sake of simulating this side effect of methane hydrate production.

A variety of problems involving HBS have been analyzed with the proposed numerical code; from small scale laboratory tests to field scale simulations, and involving hydrate formation/dissociation, as well as, ice formation/melting.

The simulation of two gas production tests conducted in the lab are analyzed under controlled conditions on a natural HBS sample. This type of experiment are very useful for both, to advance the current knowledge about the complex behavior of sediments under this condition, and to validate numerical tools. The main tendencies observed in the experiments, in terms of pressure evolution, gas produced and temperature are qualitatively well captured by the model. However in case of analyzing the specimen of the Krishna Godavari Basin, the adopted model under-predicts the recorded temperature during hydrate dissociation. To achieve a better description of the complex S_h distribution observed in the specimen under study, a model that contemplates a non-uniform hydrate distribution is developed, which is able to capture very satisfactorily the observed

experimental behavior, confirming that the main physics that control this problem are properly implemented in the formal framework. Also, the experimental dissociation test on the specimen from Ulleung Basin is simulated and based on the location of thermocouple, the heterogeneity of hydrate distribution does not have considerable effects on the results. Both models also assisted to understand the propagation of the dissociation fronts inside the sample and the patterns of ice formation during the experiment. The two different set of assumptions behind of these two experiments address the characteristic behaviors of hydrate dissociation.

Further, two models are developed, which replicate the temperature and pressure evolutions during (around) $2,000 \times 10^3$ years that have led to the formation of gas hydrate at Mount Elbert site, Alaska. It was assumed that the hydrates were formed at depth 300m below the current ground surface elevation by consuming the preexisting gas upon providing the favorable P-T conditions by arising the elevation and cooling the temperature at the ground surface elevation. The concentration of formed hydrate is compatible with that of calculated theoretically. Based on the other scenario assuming hydrates were formed at depth 650m below the current ground surface by consuming migrated gas from lower elevation a $S_h \sim 0.63$ was computed, which concurs with the reported hydrate saturation in the unit under analysis.

Finally, the following activities are recommended for the future studies:

- Extending the analytical solution for the reservoir with more than one wellbore. By modifying the assumed boundary conditions, it is possible to calculate the profile of drawdown due to multiple sources of depressurization.

- Moreover, the suggested analytical solution can be adapted for the case of hydrate gas production induced by depressurization from a horizontal well. Besides considering the proper boundary conditions, the equation of flow at equilibrium should be adjusted.

- Furthermore, with the same approach but in different assumption, the analytical solution can be developed under the transient condition. In this case, the endothermic feature of hydrate dissociation and the ambient heat provided by surrounding should be considered. Obviously, all terms should be taken into consideration in terms of time evolution. The outputs provide valuable details about the production strategy optimization based on the effect of crucial parameters in terms of time and duration of depressurization.

REFERENCES

Ahmadi, G., Ji, C., & Smith, D. H. (2004). Numerical solution for natural gas production from methane hydrate dissociation. Journal of petroleum science and engineering, 41(4), 269-285.

Ajayi, T., Anderson, B.J., Seol, Y., Boswell, R., & Myshakin, E.M., (2018). Key aspects of numerical analysis of gas hydrate reservoir performance: Alaska North Slope Prudhoe Bay Unit "L-Pad" hydrate accumulation. *Journal of Natural Gas Science and Engineering,* 51, 37-43.

Bear, J., (1979). Hydraulics of groundwater. *McGraw-Hill Inc*. ISBN 0-07-004170-9.

Bird, K.J., (1981). Machine-generated displays of well logs and lithology from selected wells on the North Slope of Alaska; 7 wells from the east-central North Slope. *U.S. Geological Survey* Open-File Report 81-1036.

Bird, K.J., (1999). Geographic and geologic setting. Chapter GG, In: The Oil and Gas Resource Potential of the Arctic National Wildlife Refuge 1002 Area, Alaska, by ANWR Assessment Team: *U.S. Geological Survey* Open-File Report 98-34.

Briaud, J. L., & Chaouch, A., (1997). Hydrate melting in soil around hot conductor. *Journal of geotechnical and geoenvironmental engineering,* 123(7), 645-653.

Brigham, K.K., & Miller, G.H., (1983). Paleotemperature estimates of the Alaskan Arctic Coastal Plain during the last 125,000 years. *Proceedings of Fourth Internatinal Conference on Permafrost*, 17e22 July, Fairbanks, Alaska. Washington, D.C. National Academy Press, pp. 80e85.

Boswell, R., (2009). Is gas hydrate energy within reach? *Science* 325, 957–958.

Brooks, R.H., & Corey, A.T., (1966). Hydraulic properties of porous media affecting fluid flow. *Proc. ASCE J. Irrig. Drain. Div.*, 92, 61-68.

Bujak Research International, (2008). Palynological Biostratigraphy of the Interval 1990e2484ft Mount Elbert 01 Well Northern Alaska. Report, 23 pp.

Chatti I, Delahaye A, Fournaison L,& Petitet J-P (2005). Benefits and drawbacks of clathrate hydrates: a review of their areas of interest. *Energy conversion and management,* 46:1333–1343.

Collett, T.S., (1993). Natural gas hydrate of Prudhoe Bay and Kuparuk River area, North Slope, Alaska. *AAPG Bulletin* 77 (5), 793e812.

Collett, T.S., Bird, K.J., Kvenvolden, K.A., & Magoon, L.B., (1988). Geologic interrelations relative to gas hydrates within the North Slope of Alaska. *USGS* Open-File Report 88-389.

Collett, T.S., et al., (2008). Energy source potential of gas hydrates on the North Slope of Alaska-Project briefing. *BP-DOE Gas Hydrate Meeting presentation* on March 08, Personal communication.

Dai, S., Lee, Ch., & Santamarina, J.C., (2011). Formation history and physical properties of sediments from the Mount Elbert Gas Hydrate Stratigraphic Test Well, Alaska North Slope. *Marine and Petroleum Geology* 28 (2011) 427-438.

Davie, M. K., & Buffett, B. A., (2001). A numerical model for the formation of gas hydrate below the seafloor. *Journal of Geophysical Research,* 106(B1), 497-514.

De Glee, G., (1951). Berekeningsmethoden voor de winning van groundwater. *Drinkwatervoorzeiening, 3e Vacantiecursus*, 38-80.

Dickens, G. R., Paull, C. K., & Wallace, P. (1997). Direct measurement of in situ methane quantities in a large gas-hydrate reservoir. *Nature,* 385, 426-428.

Elias, S.A., & Matthews Jr., J.V., (2002). Arctic North American seasonal temperatures from latest Miocene to the Early Pleistocene, based on mutual climatic range analysis of fossil beetle assemblages. *Canadian Journal Earth Science* 39, 911e920.

Esmaeilzadeh, F., Zeighami, M.E., & Kaljahi, J.F., (2011). 1-D Mathematical Modeling of Hydrate decomposition in Porous Media by Depressurization and Thermal Stimulation. *Journal of Porous Media*, 14(1).

Fjaer E., Cerasi, P., Li, L., & Papamichos, P., (2004). Modeling the rate of sand production. *ARMA/NARMS* 04-588.

Frederiksen, N.O., Andrle, V.A., Sheehan, T.P., Ager, T.A., Collett, T.S., Fouch, T.D., Franczyk, K.J., & Johnsson M.J., (1998). Palynological dating of Upper Cretaceous to middle Eocene strata in the Sagavanirktok and Canning formations, North Slope of Alaska. *U.S. Geological Survey* Open-File Report 98-471.

Gens, A., & Olivella S., (2001). THM phenomena in saturated and unsaturated porous media. *Revue française de génie civil*, 5(6), 693-717.

Garg, S., Pritchett, J., Katoh, A., Baba, K., & Fujii, T., (2008). A mathematical model for the formation/dissociation of methane hydrates in the marine environment. *Journal of Geophysical Research,* 113:B01201.

Goel, N., Wiggins, M., & Shah, S., (2001). Analytical modeling of gas recovery from in situ hydrates dissociation. *Journal of Petroleum Science and Engineering*. 29(2), 115-127.

Gupta, S., Deusner, C., Haeckel, M., Helmig, R., & Wohlmuth, B., (2017). Testing a thermos-chemo-hydro-geomechanical model for gas hydrate-bearing sediments using triaxial compression laboratory experiments. *Geochem. Geophys.Geosyst.,* 18, 3419–3437.

Hong, H., & Pooladi-Darvish, M., (2005). Simulation of depressurization for gas production from gas hydrate reservoirs. *Journal of Canadian Petroleum Technology*, 44(11), 39-46.

Hong, H., Pooladi-Darvish, M., & Bishnoi, P., (2003). Analytical modeling of gas production from hydrates in porous media. *Journal of Canadian Petroleum Technology*, 42(11), 45-56.

Inks, T.L., Lee, M.W., Agena, W.F., Taylor, D.J., Collett, T.S., Zyrianova, M.V., & Hunter, R.B., (2008). Seismic prospecting for gas hydrate and associated free-gas prospects in the Milne Point area of northern Alaska. In: Collett, T., Johnson, A.

Isehunwa S.O., et al., (2010). A simple analytical model for predicting sand production in a Niger delta oil filed. *International Journal of Engineering Science and Technology.* Vol. 2(9), 2010, 4379-4387.

Jamaluddin, A., Kalogerakis, N., & Bishnoi, P., (1991). Hydrate plugging problems in undersea natural gas pipelines under shutdown conditions. *J. Petroleum Science and Engineering,* 5:323-335.

Ji, C., Ahmadi, G., & Smith, D.H., (2001). Natural gas production from hydrate decomposition by depressurization. *Chemical Engineering Science*, 56(20), 5801-5814.

Kamath, V., & Godbole, S., (1987). Evaluation of hot-brine stimulation technique for gas production from natural gas hydrates. *Journal of petroleum technology*, 39(11). 1379-1388.

Kaufman, D.S., et al., (2004). Holocene thermal maximum in the western Arctic (0e180 _C). *Quaternary Science Reviews* 23, 529e560.

Kayen, R. E., & Lee, H. J. (1991). Pleistocene slope instability of gas hydrate-laden sediment on the Beaufort Sea margin. *Marine Georesources & Geotechnology*, 10(1-2), 125-141.

Kim, J., Moridis, G.J., Yang, D., & Rutqvist, J. (2012). Numerical studies on two way coupled fluid flow and geomechanics in hydrate deposits. *SPE-141304.*

Kimoto, S., Oka, F., & Fushita, T., (2010). A chemo-thermo-mechanically coupled analysis of ground deformation induced by gas hydrate dissociation. *International Journal of Mechanical Sciences,* 52(2), 365-376.

Kimoto, S., Oka, F., Fushita, T., & Fujiwaki, M. (2007). A chemo-thermo-mechanically coupled numerical simulation of the subsurface ground deformations due to methane hydrate dissociation. *Computers and Geotechnics*, 34(4), 216-228.

Klar, A., Soga, K., & Ng, M. (2010). Coupled deformation—flow analysis for methane hydrate extraction. *Geotechnique,* 60(10), 765-776.

Klar, A., Uchida, S., Soga, K., & Yamamoto, K., (2013). Explicitly coupled thermal flow mechanical formulation for gas-hydrate sediments. *SPE Journal*, 18(02), 196-206.

Klauda, J.B., & Sandler, S.I., (2005). Global Distribution of Methane Hydrate in Ocean Sediment. *Energy & Fuels*, 19, 459-470.

Konno, Y., Masuda, Y., Hariguchi, Y., Kuriharra, M., & Ouchi, H., (2010). Key factors for depressurization induced gas production from oceanic methane hydrates. *Energy&Fuels*, 24(3), 1736-1744.

Kvenvolden, K.A., (1998). A primer on the geological occurrence of gas hydrate. In: Henriet, J.P. & Mienert, J. (eds). Gas hydrates: Relevance to world margin stability and climate change. *Geological Society London Special Publication* 137. pp 9–30.

Kwon, T.H., Cho, G.C., & Santamarina, J.C., (2008). Gas hydrate dissociation in sediments: Pressure- temperature evolution. *Geochemistry, Geophysics, Geosystems*, 9(3).

Lachenbruch, A.H., Sass, J.H., Marshall, B.V., & Moses Jr., T.H., (1982). Permafrost, heat flow, and the geothermal regime at Prudhoe Bay, Alaska. *Journal of Geophysical Research* 87 (B11), 9301e9316.

Lee, M.W., & Collett, T.S., (2011). In-situ gas hydrate hydrate saturation estimated from various well logs at the Mount Elbert Gas Hydrate Stratigraphic Test Well, Alaska North Slope. *Journal of Marine and Petroleum Geology* 28 (2), 439e449.

Lee, S.Y., & Holder, G.D., (2001). Methane hydrates potential as a future energy source. *Fuel Processing Technology*, 71, 181–186.

Matheus, P., Beget, J., Mason, O., & Gelvin-Reymiller, C., (2003). Late Pliocene to late Pleistocene environments preserved at the Palisades Site, central Yukon River, Alaska. *Quaternary Research* 60, 33e43.

Milkov, A.V., (2004). Global estimates of hydrate-bound gas in marine sediments: how much is really out there? *Earth-Science Reviews*, 66, 183 – 197.

Moridis, G.J., (2014). TOUGH+HYDRATE v1.2 User's Manual: A Code for the Simulation of System Behavior in Hydrate Bearing geologic Media. *R. LBNL-3158, ed*., Lawrence Berkeley National Laboratory, Berkeley, CA.

Moridis, G.J., Collett, T., Boswell, R., Kurihara, M., Regan, M.T., Koh, C., & Sloan Jr, E.D., (2008). Toward production from gas hydrates: current status, assessment of resources, and simulation-based evaluation of technology and potential. *SPE* 114163, Keystone, Colo.

Moridis, G.J., Silpngarmlert, S., Reagan, M.T., Collett, T., & Zhang, K., (2011). Gas production from a cold, stratigraphically-bounded gas hydrate deposit at the Mount Elbert gas hydrate stratigraphic test well, Alaska North Slope: implications of uncertainties. *Marine and Petroleum Geology*, 28, 517-534.

Nazridoust, K., & Ahmadi, G., (2007). Computational modeling of methane hydrate dissociation in a sandstone core. *Chemical engineering science,* 62(22), 6155-6177.

Olivella S., (1995). Non-isothermal multiphase flow of brine and gas through saline media. *Phd Thesis*, Geotechnical Engineering Department, Technical University of Catalunya, Spain.

Olivella, S., Gens, A., Carrera, J., & Alonso, E.E., (1996). Numerical formulation for a simulator (CODE-BRIGHT) for the coupled analysis of saline media. *Engineering Computations*, 13/7:87-112.

Olivella, S., Carrera J., Gens, A., & Alonso, E.E., (1994). Non-isothermal multiphase flow of brine and gas through saline media. *Transport in porous media*, 15, pp. 271-293.

Papamichos, E., (2004). Failure in rocks. *RFGC*, 8:5-6, 709-734.

Papamichos, E., & Vardoulakis, I., (2005). Sand erosion with a porosity diffusion law. *Computers and Geotechnics,* 32 47-58.

Parrish, J.M., Parrish, J.T., Hutchison, J.H., & Spicer, R.A., (1987). Late Cretaceous vertebrate fossils from the North Slope of Alaska and implications for dinosaur ecology. *PALAIOS* 2 (4), 377e389.

Pooladi-Darvish, M., (2004). Gas production from hydrate reservoirs and its modeling. *Journal of Petroleum Technology*, 56(6), 65-71.

Rahmati, H., Jafarpour, M., Azadbakht, S., Nouri, A., Vaziri, H., Chan, D., & Xiao, Y., (2013). Review of sand production prediction models. *Journal of Petroleum Engineering*, 864981.

Reimnitz, E., Wolf, S.C., & Rodeick, C.A., (1972). Preliminary interpretation of seismic profiles in the Prudhoe Bay area, Beaufort Sea, Alaska. *U.S. Geological Survey* Open-File Report 72-312.

Rempel, A., & Buffett, B., (1997). Formation and accumulation of gas hydrate in porous media. Journal of Feophysical *GEOPHYSICAL RESEARCH-ALL SERIES-,* 102, 10-10.

Rutqvist, J., & Moridis, G., (2007). Numerical studies of geomechanical stability of hydrate-bearing sediments. *Offshore Technological Conference*, Houston, U.S.A.; 30/04–3/05. OTC 18860.

Rutqvist, J., (2011). Status of the TOUGH-FLAC simulator and recent applications related to coupled fluid flow and crustal deformations. *Computers & Geosciences,* 37(6), 739-750.

Sanchez, M., & Santamarina, J.C., (2015). THCM Coupled Model for Hydrate-Bearing Sediments: Data Analysis and Design of New Field Experiments (Marine and Permafrost Settings). *DOE Quarterly Research Performance Progress Report* (Period ending 12/31/2014).

Sloan, E.D., (1998). Gas Hydrates: Review of Physical/Chemical Properties. *Energy & Fuels*, 12, 191-196.

Sloan, E.D., & Koh, C.A., (2008). Clathrate hydrates of natural gases, 3rd ed. *CRC Press*, ISBN: 0-8493-9078-8.

Soga, K., Lee, S.L., Ng, M.Y.A., & Klar, A., (2006). Characterisation and engineering properties of methane hydrate soils. *Characterisation and engineering properties of natural soils*, 2591-2642.

Spicer, R.A., & Chapman, J.L., (1990). Climate change and the evolution of high-latitude terrestrial vegetation and floras. *TREE* 5 (9), 279e284.

Sultan, N., Foucher, J. P., Cochonat, P., Tonnerre, T., Bourillet, J. F., Ondreas, H., Cauquil, E., & Grauls, D., (2004). Dynamics of gas hydrate: case of the Congo continental slope. *Marine Geology,* 206(1-4), 1-18.

Tsypkin, G.G., (2000). Mathematical models of gas hydrates dissociation in porous media. *Annals of the New York Academy of Sciences*, 912(1), 428-436.

Uchida, S., Klar, A., & Yamamoto, K., (2016). Sand production model in gas hydrate-bearing sediments. *International Journal of Rock Mechanics & Mining Sciences*, 86, 303-316.

Ullerich, J., Selim, M., & Sloan, E., (1987). Theory and measurement of hydrate dissociation. *AIChE Journal*, 33(5), 747-752.

Valin, Z.C., & Collett, T.S., (1992). Molecular and isotopic analyses of the hydrocarbon gases within gas hydrate-bearing rock units of the Prudhoe Bay-Kuparuk River area in Northern Alaska. *U.S. Geology Survey*, Open-File Report 92-299.

Van Genuchten, M.T., (1980). A closed-form equation for predicting the hydraulic conductivity of unsaturated soils. *Soil Sci. Soc. Am. J.*¸44, 892-898.

Van Genuchten, R., (1978). Calculating the unsaturated hydraulic permeability conductivity with a new closed-form analytical model. *Water Resource Researc*, 37(11), pp. 21-28.

Walsh, M.R., Hancock, S.H., Wilson, S.J., Patil, S.L., Moridis, G.J., Boswell, R., Collet, T.S., Koh, C.A., & Sloan, E.D., (2009). Preliminary report on the commercial viability of gas production from natural gas hydrate. *Energy Economics*, 31(5), 815-823.

Wagner, W., & Kretzschmar, H.J., (2008). International Steam Tables, 2nd edition. *Springer Verlag*, Berlin, Heidelberg, 2008.

Wang, J., Yale, D., Dasari, G., & ExxonMobil Upstream Research Company, (2011). Numerical modeling of sand production. *SPE* 147110.

Webb, S.W., (2000). A simple extension of two-phase characteristic curves to include the dry region. *Water Resour. Res.,* 36, 1425-1430.

Wolfe, J.A., (1980). Tertiary climates and floristic relationships at high latitudes in the northern hemisphere. *Palaeogeography, Palaeoclimatology, Palaeoecology* 30, 313e323.

Wolfe, J.A., (1994). Tertiary climatic change at middle latitudes of western North America. *Palaeogeography, Palaeoclimatology, Palaeoecology* 108, 195e205.

Wolfe, J.A., & Upchurch Jr., G.R., (1987). North American nonmarine climates and vegetation during the late Cretaceous. *Palaeogeography, Palaeoclimatology, Palaeoecology* 61, 33e77.

Xu, W., & Germanovich, L.N., (2010). Excess pore pressure resulting from methane hydrate dissociation in marine sediments: A theoretical approach. *Journal of Geophysical Research*, Vol. 111, B01104.

Xu, W., & Ruppel, C., (1999). Predicting the occurrence, distribution, and evolution of methane gas hydrate in porous marine sediments. *Journal of Geophysical Research,* 104(B3), 5081-5095.

Yamamoto, K., Terao, Y., Fujii, T., Ikawa, T., Seki, M., Matsuzawa, M., & Kanno, T., (2014). Operational overview of the first offshore production test of methane hydrates in the Eastern Nankai Trough. *OTC-25243-MS*.

Younglove, B., & Ely, J., (1987). Thermophysical Properties of Fluids II Methane, Ethane, Propane, Isobutane, and Normal Butane. *Journal of Physical and Chemical Reference* Data 16 (4):5

Yun, T.S., Fratta, D., & Santamarina, J.C., (2010). Hydrate bearing sediments from the Krishna Godavari Basin: physical characterization, pressure core testing, and scaled production monitoring. *Energy Fuels*, 24, 5972-5983.

Yun, T.S., Lee, C., Lee, J.S., Bahk, J.J., & Santamarina, J.C., (2011). A pressure core based characterization of hydrate bearing sediments in the Ulleung Basin, Sea of Japan (East Sea). *Journal of Geophysical Research*, 116, B02204.

Zhang, Z.F., Oostrom, M., & White, M.D., (2016). Relative permeability for multiphase flow for oven-dry to full saturation conditions. *International Journal of Greenhouse Gas Control*, 49, 259-266.

White, M.D., (2008). Numerical simulation of methane hydrate production from geologic formation via carbon dioxide injection. *OTC 19458.*

White, M.D., & McGrail, B.P., (2006). STOMP-HYD: A New Numerical Simulator for Analysis of Methane Hydrate Production from Geologic Formations. *In Proceedings of the 2nd International Symposium on Gas Hydrate Technology at the 43rd Coordinating Committee for Geoscience Programmes* in East and Southeast Asia (CCOP) Annual Session, October 29 - November 3, 2006, Daejeon, Republic of Korea, ed. A Reedman, YS Park, JJ Bahk and N Chaimanee, pp. 77-86. The Coordinating Committee for Geoscience Programmes in East and Southeast Asia (CCOP), Bangkok, Thailand.